Title
PROTON-PROTON ELASTIC SCATTERING AT INCIDENCE MOMENTA 3,5, AND 7 BEV/c

Author
Clyde, Allan Roy.

Publication Date
1966-05-01

Thesis/dissertation

UCRL-16275
c.2

DISCLAIMER

UCRL-16275

UNIVERSITY OF CALIFORNIA

Lawrence Radiation Laboratory

Berkeley, California

AEC Contract No. W-7409-eng-48

PROTON-PROTON ELASTIC SCATTERING AT INCIDENCE MOMENTA 3, 5, AND 7 BEV/C

Allan Roy Clyde

(Ph.D. Thesis)

May 1966

PROTON-PROTON ELASTIC SCATTERING AT 3, 5, AND 7 BEV/C

CONTENTS

PROTON—PROTON ELASTIC SCATTERING AT 3, 5, AND 7 BEV/C

Allan Roy Clyde

Lawrence Radiation Laboratory
University of California
Berkeley, California

May 1966

ABSTRACT

Differential cross sections for p—p elastic scattering have been measured for incident momenta, 3, 5, and 7 BeV/c. The backward scattered protons were momentum analyzed with magnetic spectrometers and detected with scintillation counters for the missing mass spectrum of $p + p \rightarrow p + x$ for x = a proton. A hydrogen gas target was used for recoil momenta from 75 to 600 MeV/c and polyethylene with matched carbon for subtraction was used from 500 to 4000 MeV/c. Statistical errors were approximately 2% at low momentum transfer, and increased to about 5% for 90° scattering in the center—of—mass. The data indicates shrinkage of the diffraction peak with incident energy, a strong energy dependence of $d\sigma/d|t|$ at 90° and is consistent with a logarithmic decrease in the total elastic cross section with the center—of—mass energy. The behavior of the forward scattering indicates the presence of a real scattering amplitude. The values obtained for the ratio of the real to the imaginary scattering amplitudes are 43, 39, and 34% respectively. An assumption of similar angular dependence of the real and imaginary parts of the nucleon scattering amplitude is indicated by these data.

I. INTRODUCTION

It has been pointed out by G. F. Chew, S. C. Frautschi, and others that a Regge model with the Pomeranchuk or vacuum pole, though only approximate, leads to definite predictions for the behavior of elastic cross sections.[1,2] Previous experiments on elastic p-p scattering have established the exponential dependence of the forward scattering on t, the indicated shrinkage of the diffraction peak, and a logarithmic decrease in the total elastic cross section with s, where s is total center-of-mass energy and t is the four-momentum transfer.[2,3,4,27]

More recently, however, there has been considerable interest in various models in an attempt to understand more fully the appearance of a significant amount of real part in the forward elastic scattering amplitude.[5-9] Using a dispersion relation approach, P. Söding predicts 20 to 34% for the real part of the scattering amplitude in the 5 to 30 BeV/c range.[10] Although it does little to explain the mechanism, the agreement with present data is rather good. W. Rarita and R.J.N. Phillips have obtained reasonable agreement with experiment using a Regge Model containing the P, P', ω, and ρ poles.[11] However, it is confined to energies above 10 BeV. Also, there is continued interest in optical models using short range phase shifts and tapered potentials.

In the high momentum transfer (large angle) region of the elastic differential cross section the statistical model has been applied with some success by L. W. Jones at $\theta_{cm} > 70^{\circ}$ for high energy data between 10–20 BeV/c.[12] More dramatically, J. Orear has shown very good agreement with experiment through 12 orders of magnitude in the differential cross section using a decreasing exponential dependence on transverse three-momentum.[13,14] His fit to the recent Brookhaven data goes from 3 to 25 $(\mathrm{BeV}/c)^2$ in four-momentum transfer for incident momenta between 10-30 GeV/c and extends into the region of

$$\frac{(d\sigma/d|t|)}{(\sigma_T^2/16\pi)} \simeq 10^{-4} .$$

It seems clear that an eventual understanding of the p-p interaction is going to require a more detailed knowledge of the entire angular dependence of the elastic scattering. This experiment has been an attempt to improve p-p elastic scattering statistics and display the differential cross section over a wide range ($5^\circ \leq \theta_{cm} \leq 90^\circ$) for incident momenta 3, 5, and 7 BeV/c.

II. EXPERIMENTAL ARRANGEMENT

Incident Beam Characteristics

The Bevatron EPB (External Proton Beam) at Berkeley was used for this experiment with a momentum spread of ± .3%. The intensity was approximately 10^{11} protons per pulse with a spill length of about 300 milliseconds. Data was taken at incident beam momenta 3, 5, and 7 BeV/c.

General Layout

The apparatus consisted of three momentum spectrometers. These were located in a fixed array about the target area as shown in Fig. 1a. This was enclosed by a large vacuum tank which served to support the target mechanism and transport the secondary beam to the appropriate focusing elements. One momentum spectrometer was set at 69.5° to the EPB. Another was set at 33.5°. The third was set opposite the first two on the Bevatron side of the EPB and consisted of one horizontal bending element. The first or Low Momentum Channel (LMC) utilized a fixed H_2 gas target. This channel detected recoil particles from roughly 87° down to 66° in the lab system, corresponding to scattered momenta of 87 to 600 MeV/c. The second or High Momentum Channel (HMC) was used to take data from matched polyethlyene and carbon targets. Beginning at about 75°, this channel was operated in two distinct modes enabling it to take data at angles down to about 26° in the laboratory (just about 90° in the center-of-mass system for the 7.0 BeV/c incident momenta) for the observation of scattered momenta of 450 to 4,000 MeV/c. The general focusing properties of these two modes are shown in Figs. 1b and 1c. The third channel was used to detect the recoil protons for elastic scattering near the 90° center-of-mass point or between 25° and 35° in the laboratory. In this region of very small cross sections, it was desirable to use coincidence to detect both protons in their

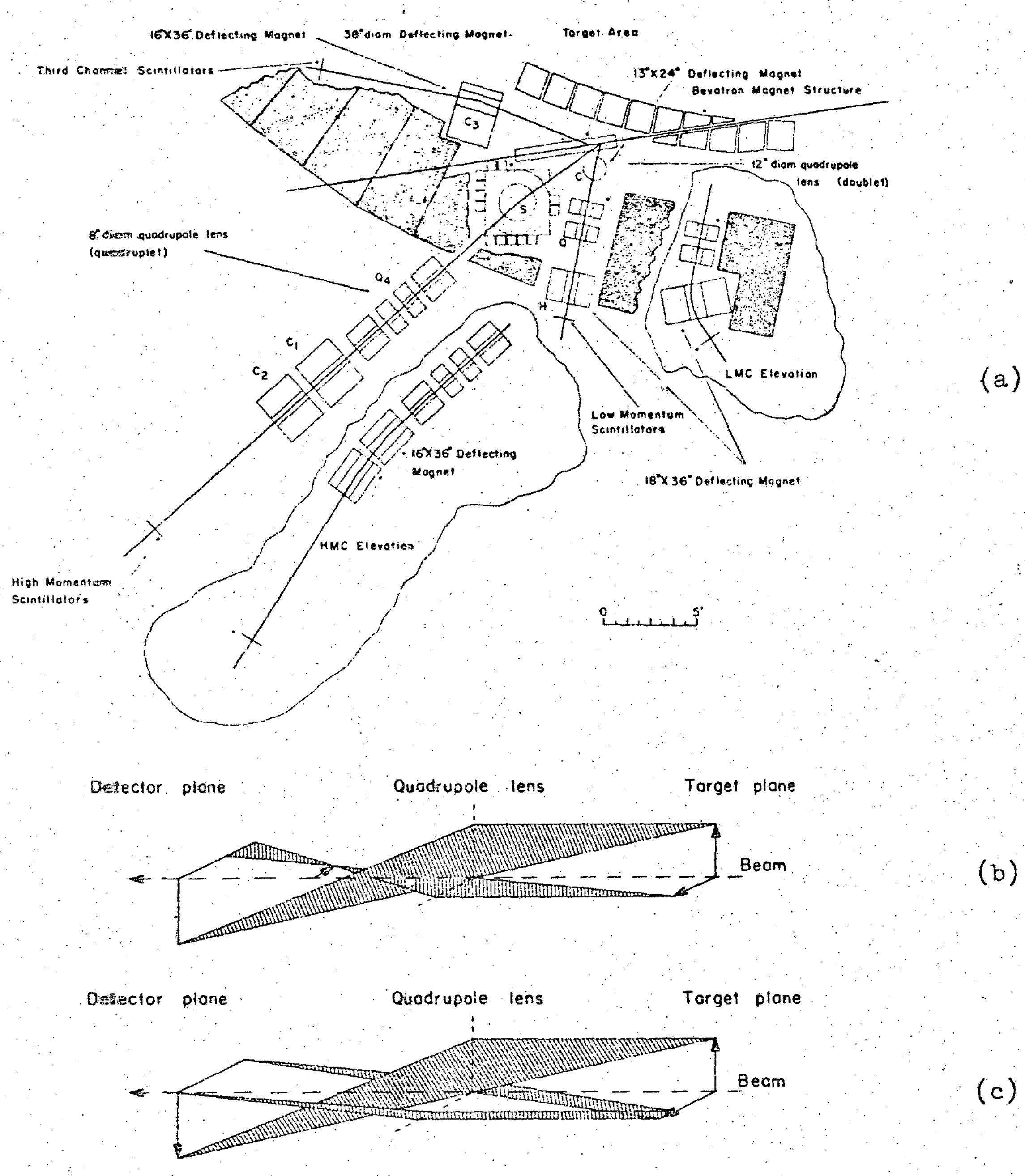

MUB-8870

Fig. 1. The experimental layout, (a) shows the three momentum spectrometers, the target area, and the shielding. Diagram (b) illustrates the basic nature of the secondary beam focusing for the "Cross-over" mode of the HMC. The "Parallel" mode is shown in (c).

appropriate kinematic relationship in order to resolve the elastic p-p scattering above background.

In both the High Momentum Channel and Low Momentum Channel the scattered protons were focused by a set of magnetic quadrupole elements (Fig. 1) and momentum analyzed by magnetic spectrometers. The tuning of these quadrupole elements entered only to second order in the calculation of the cross section. Terphenyl loaded polystyrene scintillation counters were used for the particle detection. In addition, an array of H_2O Cerenkov counters was used in the third channel.

Low Momentum Spectrometer

The LMC consisted of three magnetic elements. The first was a horizontal bending magnet. This was used to direct the scattered beam down the channel for the various angles selected. It was possible to eliminate any significant focusing or distortion in the vertical plane for this element, by utilizing pole faces of an effectively circular geometry. With the LMC orientation of 69.5° to the EPB, 16° was the maximum deflection required to bend the scattered beam down the channel. Following the horizontal bend there was a quadrupole doublet which was tuned for "point-to-point" focusing in both planes, where this requires that beam particles from a given point at the source are focused to a unique point at the image plane independent of their slope with respect to the optic axis for a monochromatic beam. The upstream element was operated as a converging lens in the horizontal plane. The beam was then deflected vertically downward through 45.2° with an H-type bending magnet into the detector system.

There were 4 scintillation counters in the LMC detector telescope. Looking downstream, they were labeled L_1, L_2, L_3, and L_4. The L_3 counter was used for vertical positioning, and the L_2 and L_4 counters were sectioned for left, right balance of the scattered beam during tuning. An illustration

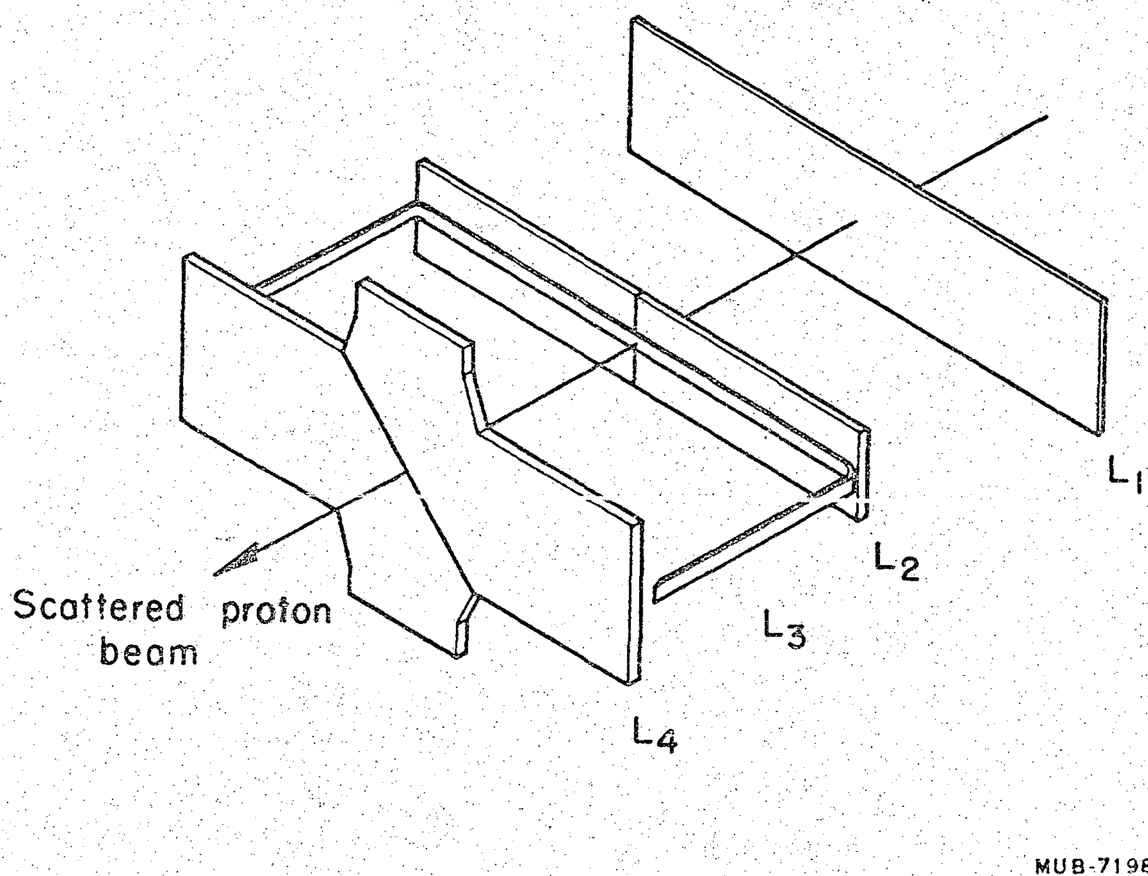

Fig. 2. The Low Momentum Channel detector arrangement showing the polystyrene scintillation counters. The 6810A photo tubes were connected to the left and right sides of L_1, L_2, and the tuning counter L_3. Connection was made at top and bottom for L_4.

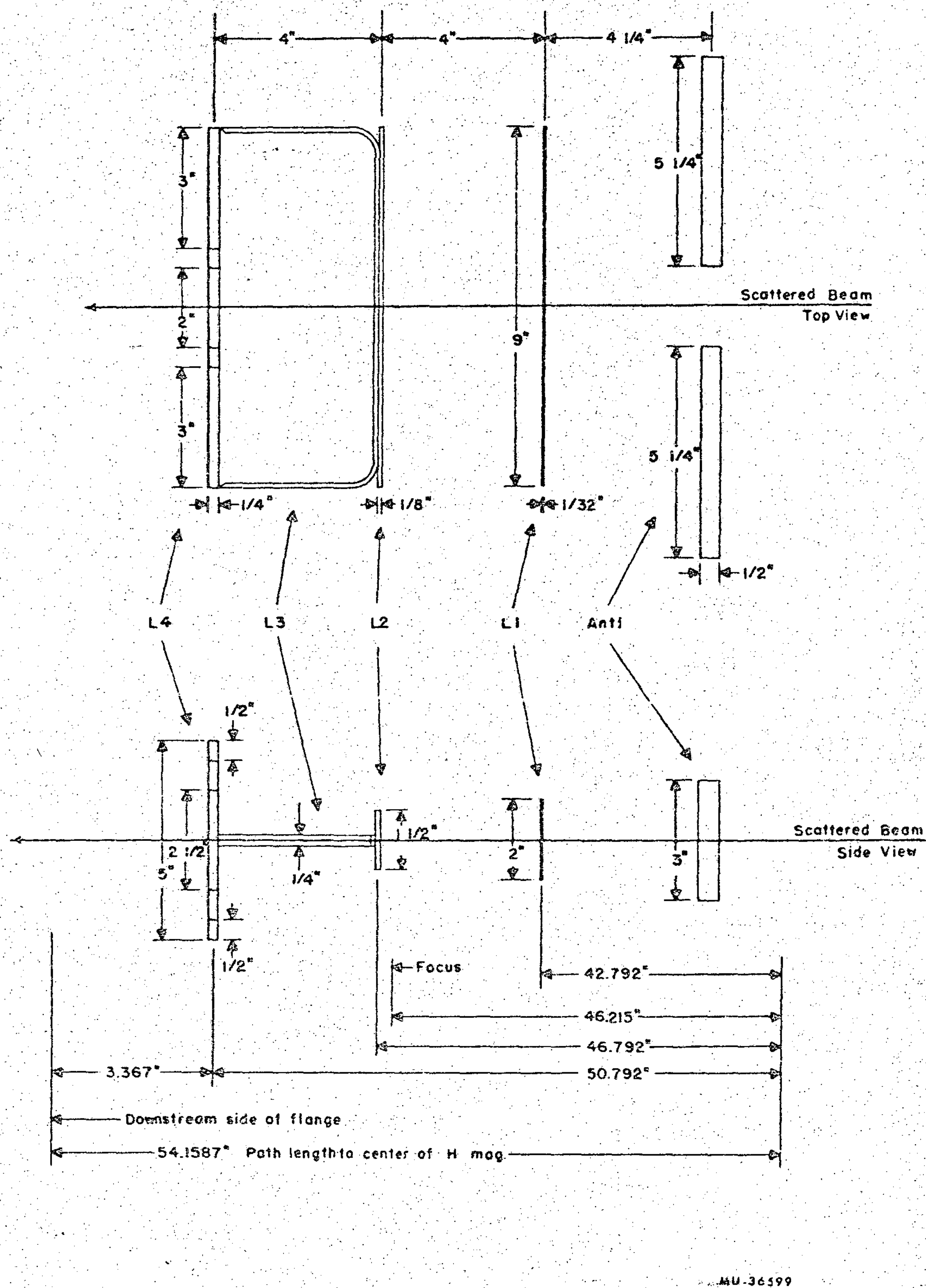

Fig. 3. The Low Momentum Channel detector arrangement showing the dimensions of the various scintillation counters.

of the detection system is shown in Fig. 2. The counter dimensions of the telescope are given in Fig. 3.

The LMC counter telescope was operated in three basic configurations. In each case, the one used depended on the energy loss in the polystyrene. For momenta from 75 to 125 MeV/c the L_1 counter (1/32" thick) was sufficient to stop the scattered beam and was therefore used alone to count the secondary beam particles. In the range of 150 to 250 MeV/c, L_1 was operated in coincidence with the L_2 counter (1/8" thick). The third configuration was an L_2 coincidence with the L_4 counter (1/4" thick) for the 300 to 600 MeV/c range.

By pulse height analysis on the L_1, L_2, or L_4 counter it was possible to select protons by proper plateauing of the discriminators in the LMC coincidence circuit. The block diagram of this circuit is shown in Fig. 4. For the higher momenta of 500 to 600 MeV/c, range in copper was used to calibrate the momentum as a check during the tuning of the system.

Hydrogen gas at one atmosphere pressure and room temperature was used as a target. The entire Low Momentum Channel was enclosed in a vacuum. The target container window for the scattered beam was .001" mylar.

In the vertical plane, the quadrupole was focused for a source along the EPB line to an image plane just beyond the L_2 counter. The height of the source was less than 1/2", defined by the vertical height of the EPB. However, in the horizontal plane the source was taken to be the effective target defined by a movable brass collimator located between the pole faces of the first bending magnet. This arrangement is illustrated in Fig. 5. The effective source was located from 11 to 13 inches from the EPB, depending on the scattering angle selected.

Using the angular dependence of the scattered momentum, and the vertical dispersion in the system, the angular acceptance in the horizontal plane was calculated from the vertical dimensions of the L_1 and L_2 scintillation counters. Over the entire momentum range

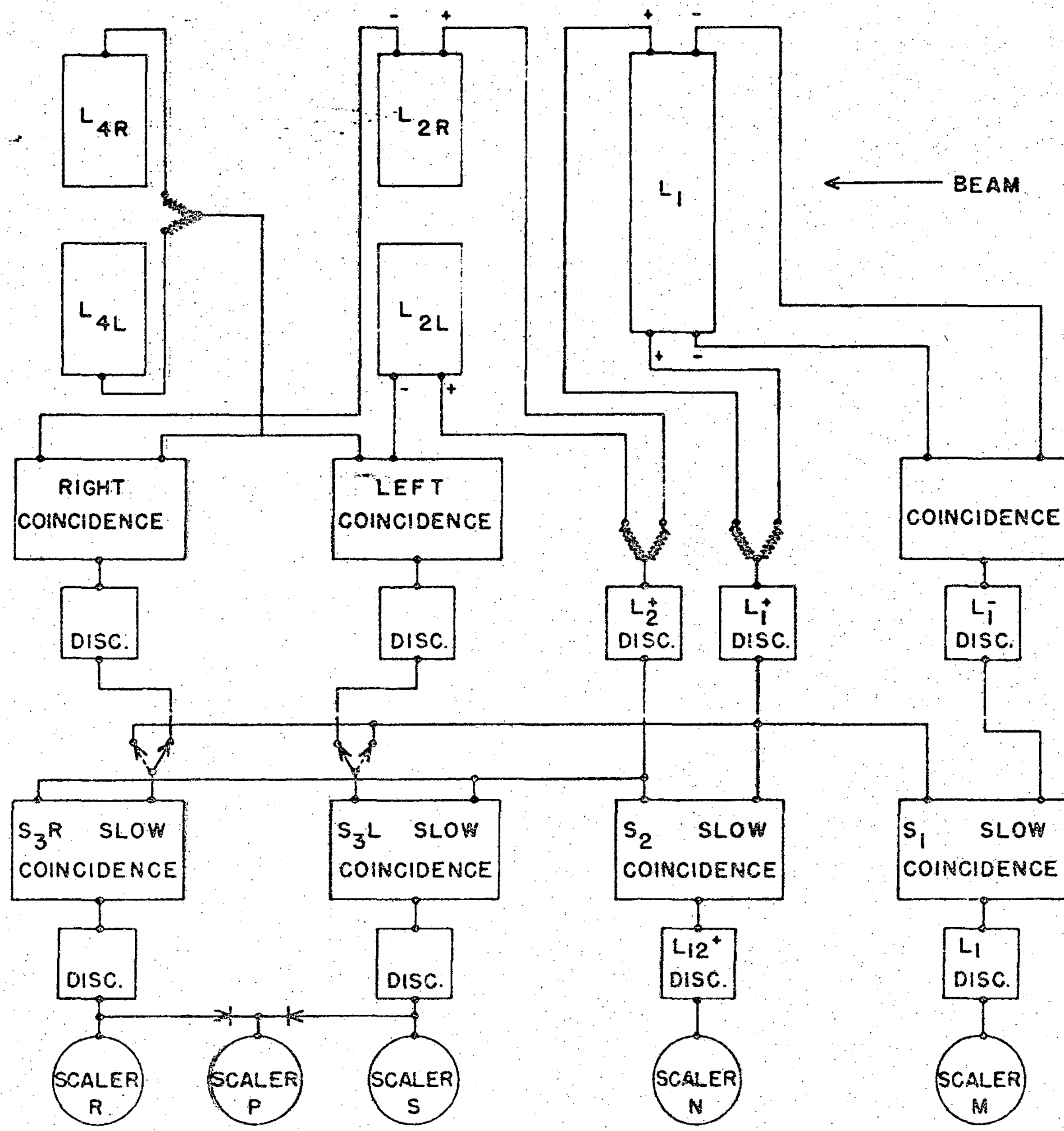

MUB-7530

Fig. 4. Block diagram of the Low Momentum Channel circuit logic.

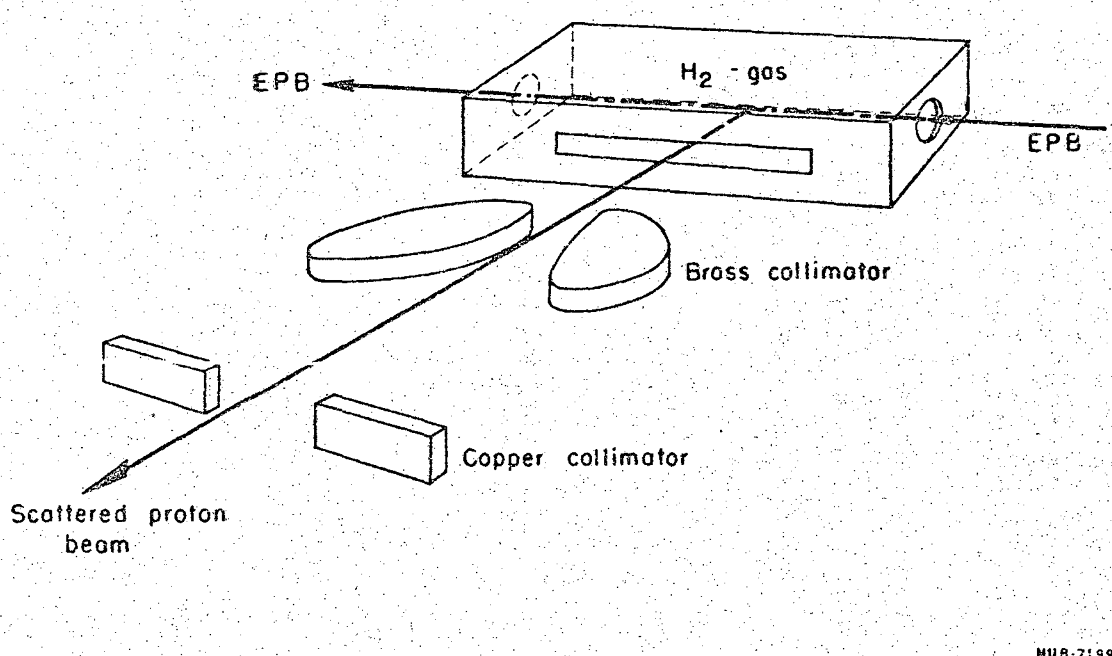

Fig. 5. The Low Momentum Channel target and collimator arrangement showing the H_2 gas container, the movable brass collimator, and the copper collimator used as the aperture stop.

observed with this channel, the angular acceptance did not exceed $\Delta\theta_1 = 1.1°$. Therefore, with $\Delta\theta_1$ small, there is no significant difference between the length determined by the brass gap/sin θ_1 and the average length of the actual source distribution subtended by the gap.

A rectangular copper collimator 2" in thickness was located between the horizontal bending magnet and the quadrupole. The downstream edge was 6.875" upstream from the effective entrance face of the quadrupole. It was adjusted in the horizontal dimension for a 9" gap so that the scattered beam would not be significantly limited by this aperture in the horizontal plane. However, the vertical dimension was fixed at 2.5", and was used to define the azimuthal angle $\Delta\phi$ of the scattered beam.

A computer program named LOTCH, for "Low Transfer channel", was used to calculate tuning currents in the magnet elements and the running systematics. These parameters were found to be accurate to 1% and they greatly simplified the final empirical tuning that was carried out for each point before data were taken.

The resolution is most conveniently given in terms of mass for $p + p \to p + X$, where X is the missing mass. For the Low Momentum Channel $\Delta m/m < 8\%$, where in Appendix A it is shown that in the region of X = 938 MeV/c^2

$$\Delta m/m = \left|(\gamma_o + 1)\beta_{cm} \cos\theta_1 \frac{\Delta P_1}{m} [(1-\beta_{cm}^2 \cos^2\theta_1)/(1+\beta_{cm}^2 \cos^2\theta_1)]\right| . \quad \text{(A-7)}$$

High Momentum Spectrometer

Similar to the LMC, the High Momentum Channel also contained 3 basic magnetic elements, consisting of a horizontal bending element followed by a

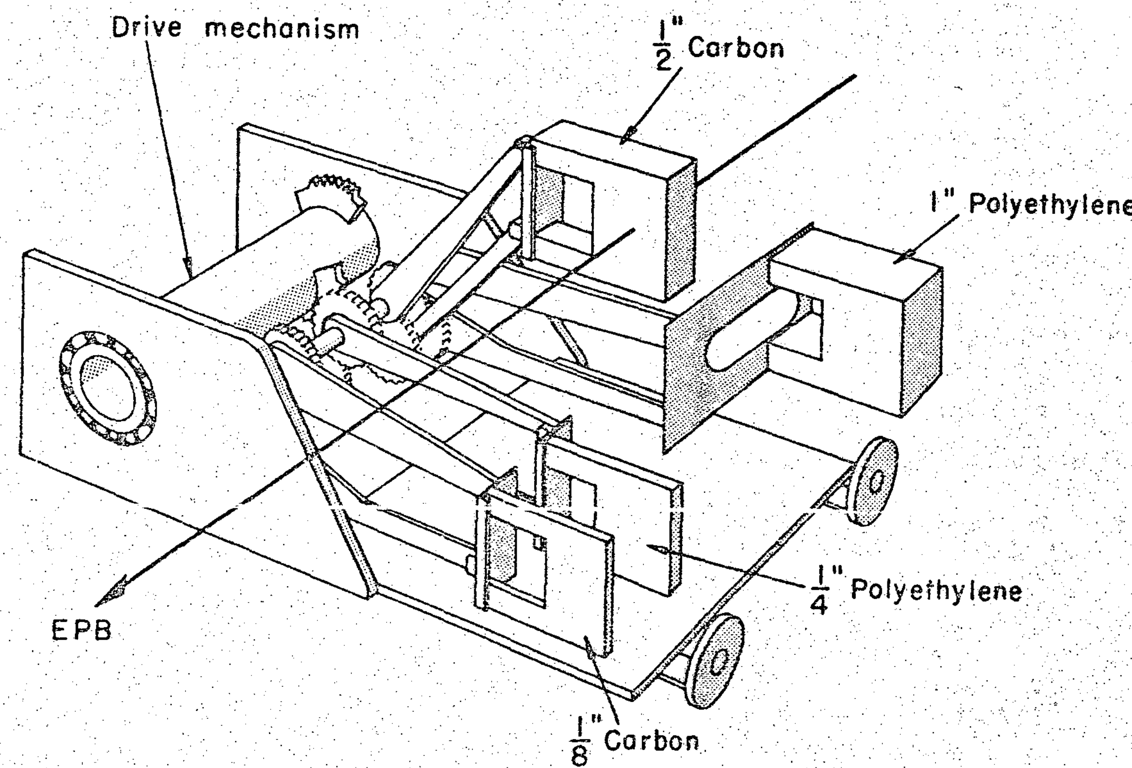

Fig. 6. The movable pantograph arrangement for the High Momentum Channel targets showing the 1/2" carbon target in position in the EPB.

focusing magnet and then a vertical deflection element used as a momentum spectrometer. This channel was set at 33.5° to the EPB. The horizontal bending element (Sagane magnet) was used to deflect the scattered beam into the channel for any of the possible target positions corresponding to scattering angles between 25° and 75° in the lab. The design of the Sagane magnet provided a large horizontal aperture. The pole faces were circular with a 40" diameter and were separated by 10". Figure 1 shows its position in the scattered beam.

Polyethylene targets of 1" and 1/4" thickness were used to take data for subtraction with their respective carbon targets of 1/2" and 1/8" thickness. These were attached to a pantograph arrangement mounted on a movable cart. This allowed any of the four targets to be raised individually into the EPB and also to be moved along the EPB. An illustration of this arrangement is shown in Figure 6. Target selection and positioning was done remotely.

Typically, several cross sections were taken alternately with the polyethylene and carbon targets after the system had been tuned for the scattering angle selected. The actual procedure varied somewhat depending on the mode of operation and focusing. The 1/4" polyethylene target was used to overlap the gas target data and the 1" polyethylene target was used to obtain data in the 90° center of mass region.

The HMC was operated in two distinct modes. The "Crossover Mode" utilized "point-to-point" focusing in both planes where the vertical focus occurred at the detectors with the horizontal focus 13' upstream. This focusing condition avoided certain physical aperture limitations of the secondary beam transport system.

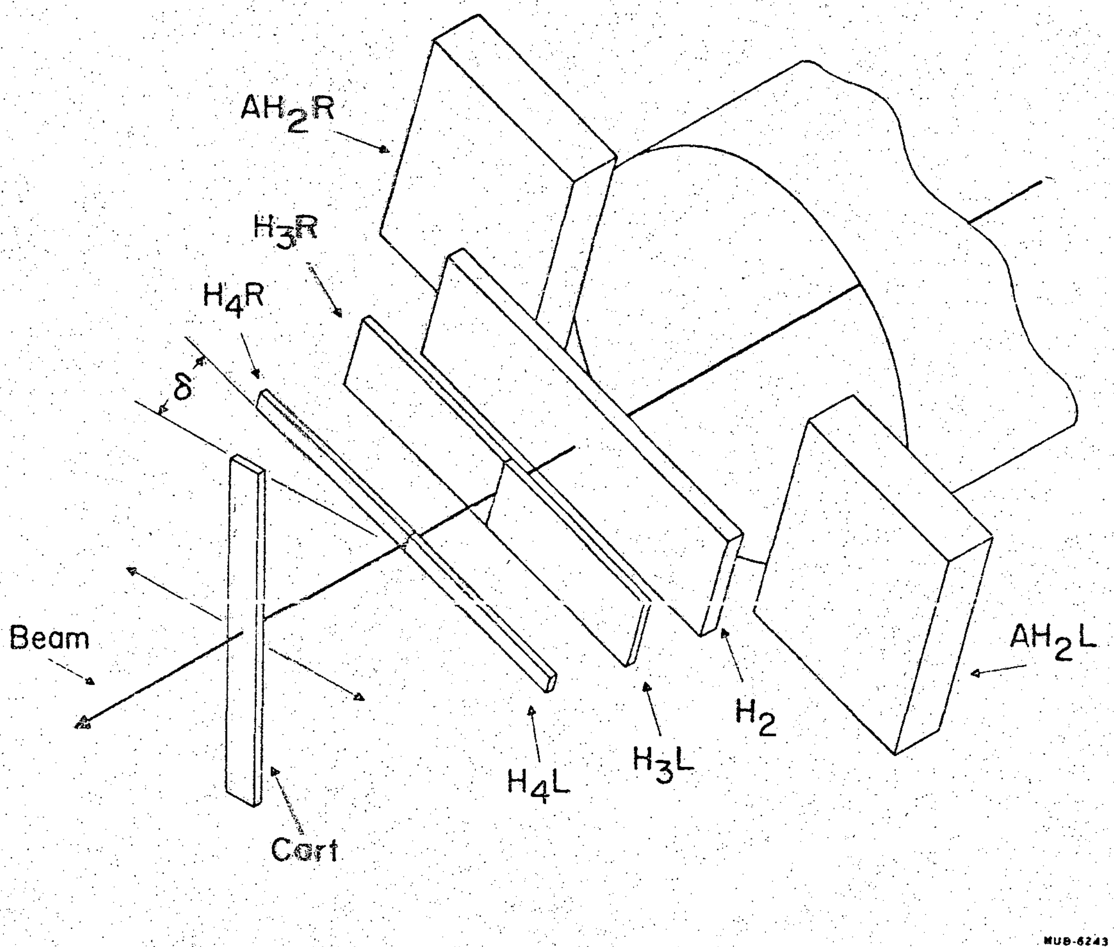

Fig. 7. The High Momentum Channel counter arrangement shown at an angle delta to the horizontal axis in a plane perpendicular to the optic axis. Also shown are the cart counter and a section of the beam transport vacuum pipe.

The data from this mode overlapped the gas target data of the low momentum channel for scattered beam momenta in the range of 450 to 2000 MeV/c. In this mode the upstream element of the four element quadrupole was operated as a converging lens in the horizontal plane with the outside elements and the inside elements being run in tandem (CDDC). This, in addition to a 6.0" horizontal and 3.038" vertical Pb aperture located 15.28" upstream from the effective entrance face of the quadrupole (see Fig. 1) helped prevent some loss of the scattered beam. The angular distribution of this beam was spread significantly at the lower momenta (450 to 800 MeV/c) by coulomb scattering. In this mode, the counters shown in Fig. 7 were used in their horizontal position. This figure also shows the 1" wide, 1/4" thick, vertical counter that was mounted on a cart for motion transverse to the scattered beam. The solid angle in this mode was determined vertically ($\Delta\phi$) by the aperture and horizontally ($\Delta\theta$) by the vertical width of the H_3 counter.

Two separate detector configurations were used in this mode. The first utilized the vertically mounted cart counter, allowing transverse motion to the scattered beam in the horizontal plane (see Fig's. 7 and 10). This scintillator was run in coincidence with the H_3 and H_2 counters, the H_1 and AH_2 counters being in anti-coincidence (see Scaler L of the block circuit diagram in Fig. 8). Data was taken by focusing the image on H_3 and then scanning it with the cart. The second configuration was used to integrate this curve directly using the H_3 and H_2 in coincidence with the H_1 and AH_2 counters in anti-coincidence. Here, as before, the H_3 counter was used for

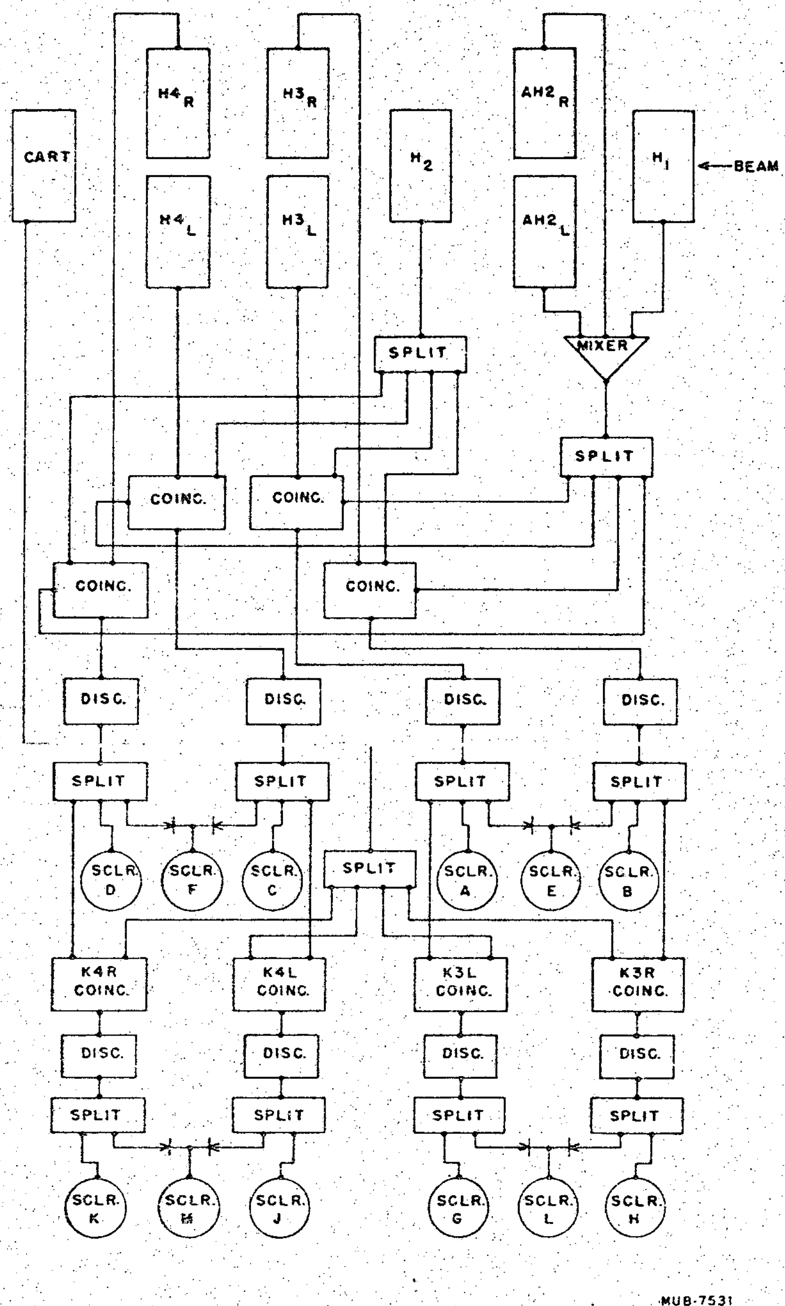

Fig. 8. Block diagram of the High Momentum Channel circuit logic for the Crossover Mode.

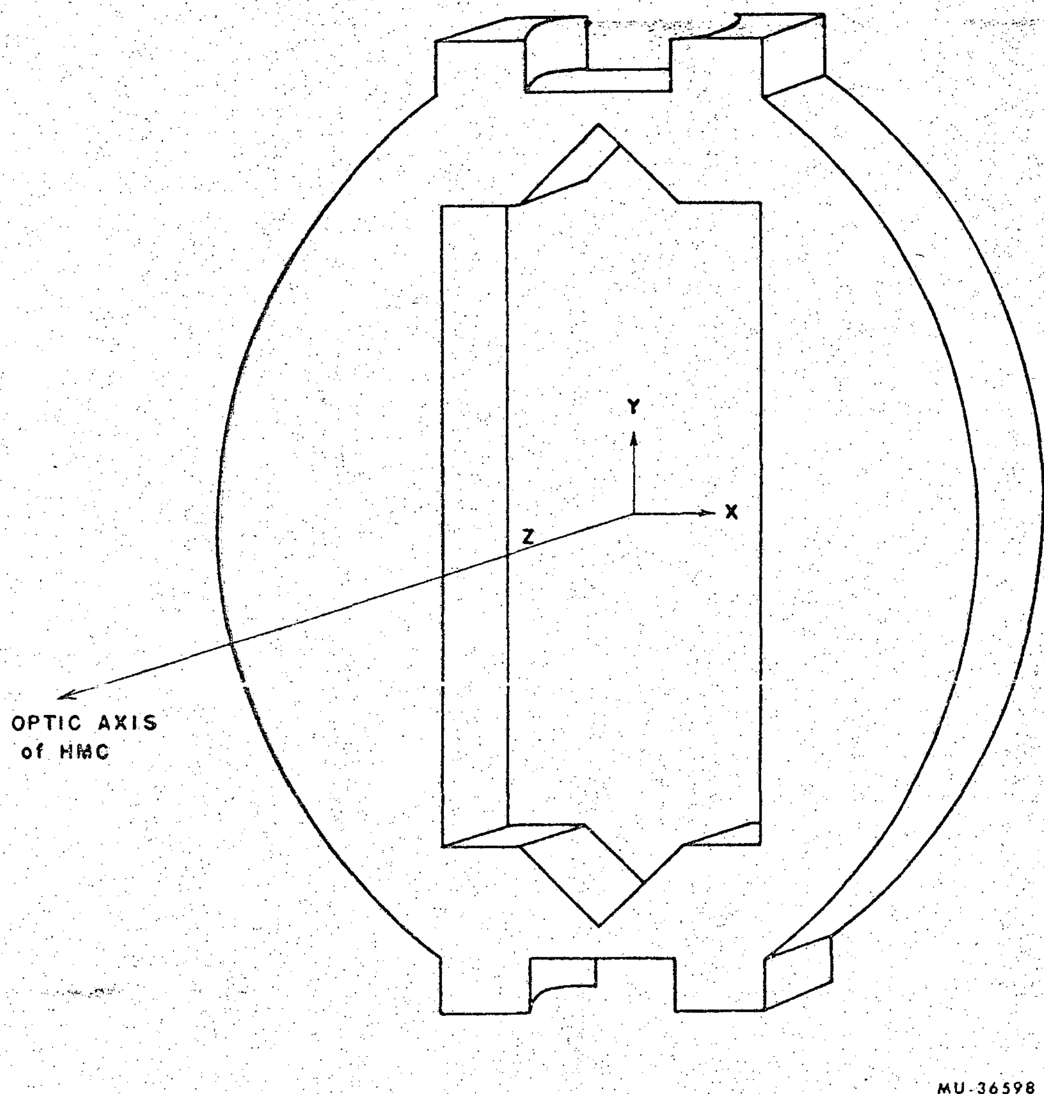

Fig. 9. Polystyrene scintillator used in anti-coincidence as the aperture stop for the Parallel Mode, light pipes and phototubes were mounted at top and bottom.

beam definition in the vertical direction transverse to the optic axis.

The "Parallel Mode" utilized point-to-point focusing in the vertical plane and parallel to point focusing in the horizontal. This means that all orbits of unique slope to the optic axis in the horizontal plane were focused to a unique point in the detection plane. This led to a unique spatial relationship between missing mass and secondary momentum at the image plane. The scattered beam rate was small for those laboratory angles observed in this mode, making desirable the use of the 1" polyethylene target. The solid angle was determined by an aperture located 15.28" upstream from the effective entrance face of the quadrupole magnet. This aperture was a polystyrene scintillator operated in anti-coincidence with the detector telescope. This counter and the geometry of the hole are shown in Fig. 9. The basic horizontal dimension was 3.0" and the vertical was 6.0" with two small triangular sections top and bottom to provide more efficient light collection.

These were isosceles right triangles with 1" legs. The light pipes and 6810A phototubes were then mounted above and below. To a good approximation the aperture had an effective shape of a rectangle 3.0" wide and 6.375" high. To be compatible with the orientation of the aperture the outside elements of the quadrupole were run diverging and the inside elements were run converging in the horizontal (DCCD).

In the image plane the counter arrangement was placed at an angle to the horizontal. This angle δ was required by the horizontal and vertical dispersion in the system, and was uniquely determined by the optics and the kinematics of elastically scattered protons. Therefore, ideally, a given incident momentum

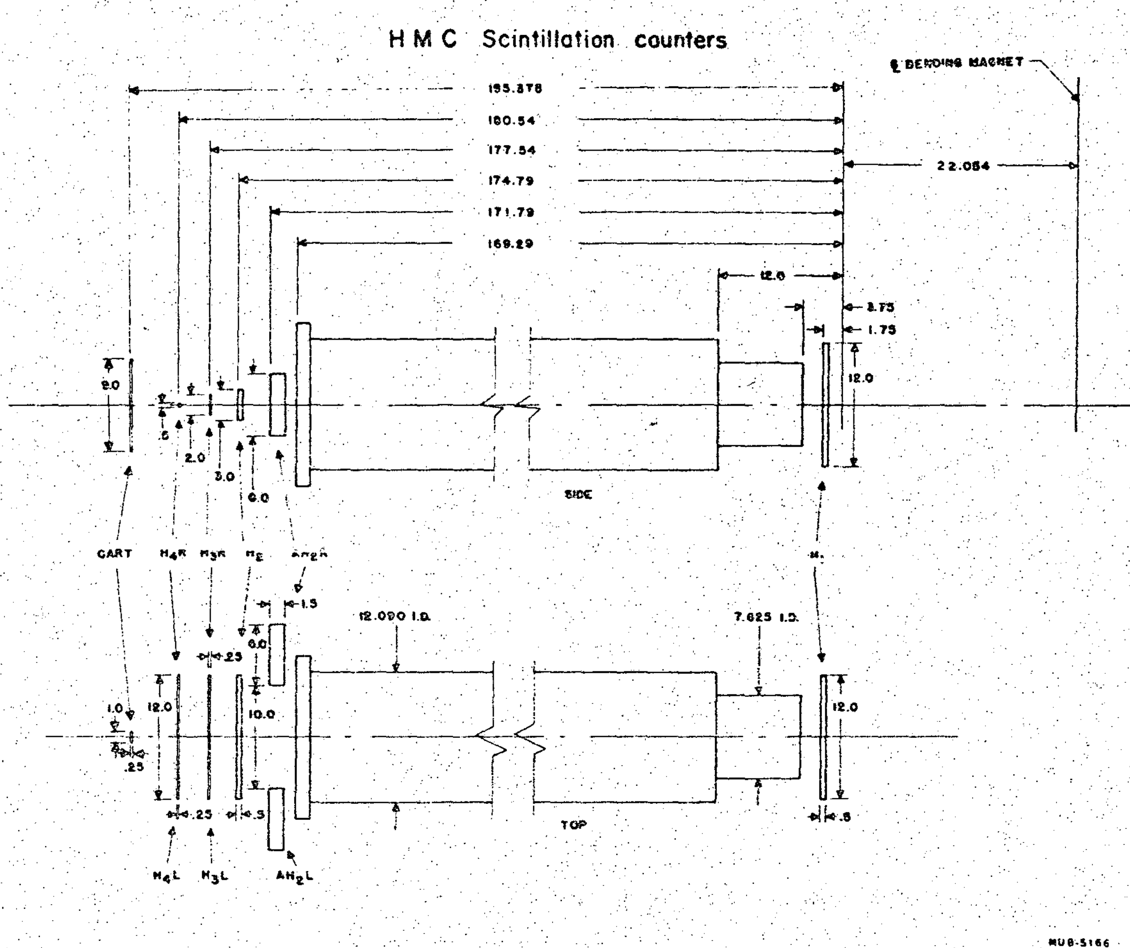

Fig. 10. The High Momentum Channel detector dimensions showing the position of the H_1 counter for the Parallel Mode data. In the Crossover Mode the H_1 scintillator was used in anti-coincidence, being replaced by a counter with a hole and located midway in the beam transport pipe. The narrow portion of this pipe (7.625 ID) to the right is the neck of the transport pipe.

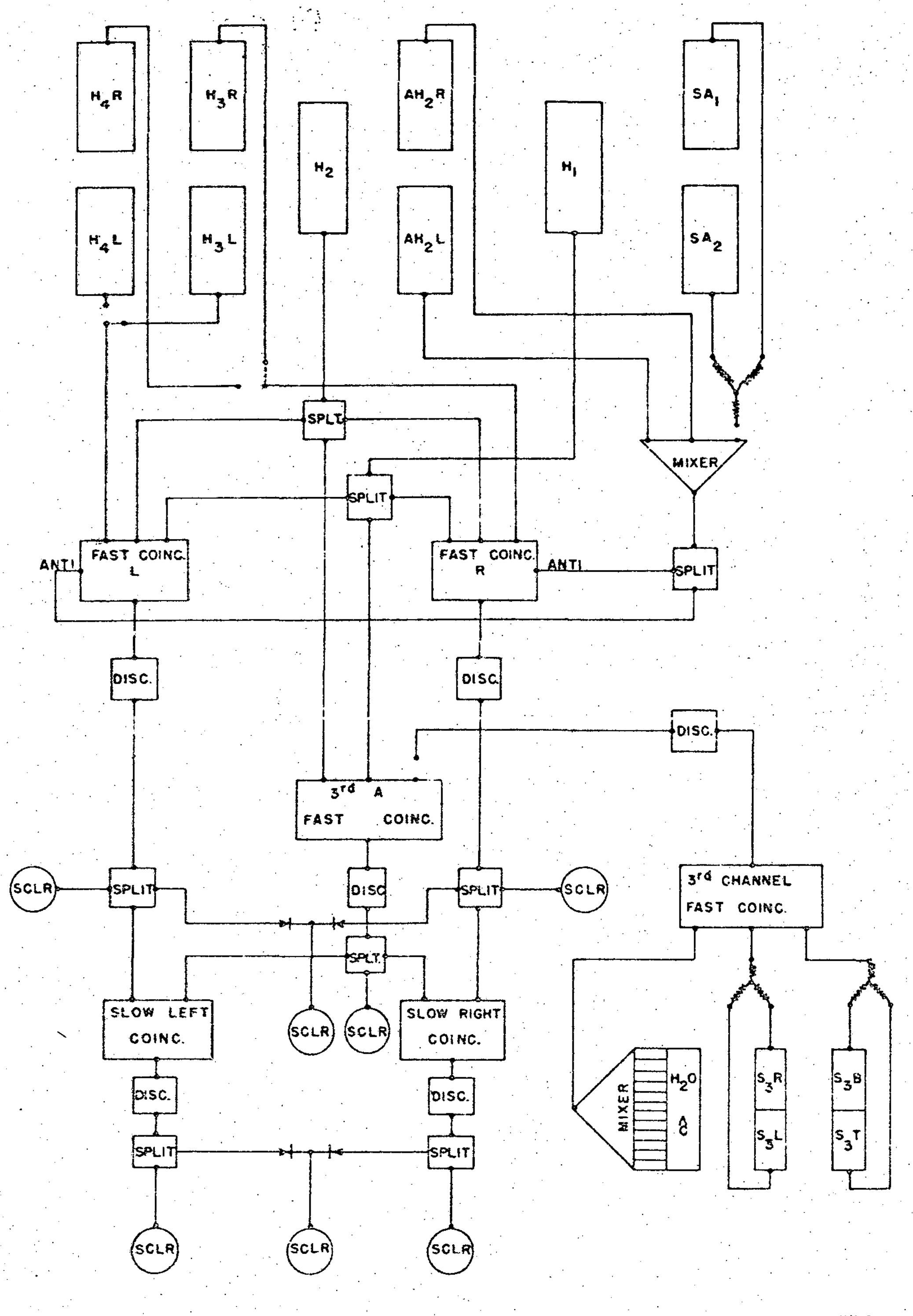

Fig. 11. Block diagram of the High Momentum Channel circuit logic for the Parallel Mode. The 3rd Channel circuit was connected for data taken at 90° in the center of mass. The SA_1 and SA_2 counters were connected for aperture calibration at low beam intensities. For some data the H_4 counters replaced the H_3 counters in the coincidence circuit.

and missing mass was represented by a line in the image plane of unique angle to the horizontal, the length of the line being determined by the secondary momentum width accepted by the aperture. Actually, of course, the line was a distribution whose width was determined by the finite source size, vertical magnification, and optical effects. This was typically about 1/2", the H_4 counter being 1/2" and the H_3 being 2" wide (see Fig. 10).

The block diagram in Fig. 11 shows the circuit logic for the coincidence telescope. The H_2 counter was used to integrate the elastic peak. This was operated in coincidence with the H_1 counter shown in Fig. 10. The AH_2 left and right counters along with the aperture were used in anti-coincidence.

The AH_2 counters shown in Fig. 10 were separated by 12" and served only to eliminate a small amount of random background. The scattered beam distribution was broad and flat, being almost trapezoidal with a width of around 8".

Data was taken by scanning the image past the H_2 counter through variation of the vertical bending magnet current about the central tuning value. The operation of this mode overlapped the Crossover Mode with the scattered beam momenta ranging from 1160 to 4000 MeV/c, providing data through the 90° center of mass region or down to lab angles of 25°.

A computer program named HITCH, for "high momentum transfer channel," was used to determine the tuning parameters for the HMC to about 1%. Fine tuning for each data point was facilitated by left-right balance of the H_3 and H_4 counters. The resolution of the system depends, as does the LMC, on scattering angle, but is less than 20% for $\Delta m/m$ given by Eq. (A-7) of Appendix A.

III. BEAM CALIBRATION

The external proton beam was monitored by an ionization chamber located on the downstream side of the vacuum tank that enclosed the target area. Absolute normalization of the elastic scattering cross section required a careful calibration of this detector. For this purpose, two small scintillation counters were located at the entrance and exit windows of the vacuum tank, and mounted on actuators that allowed them to be remotely moved into the EPB during the calibration runs. These counters were 1-3/4" square and 1/8" thick. In addition, two large 12 x 18 x 2-in. scintillators were placed in the beam at some 33 feet downstream from the vacuum tank exit window. These were centered in the beam and separated by about 4' along the beam line. The two small counters were labeled B_1 and B_2 whereas the two larger ones were B_5 and B_7, the subscripts increasing in the direction of the beam. The layout of the calibration telescope is shown in Fig. 12.

The outputs from the scintillators were split, providing scaler readout for the individual counting rates in addition to a $B_5\ B_7$ coincidence, and also a $B_1\ B_5$ and $B_2\ B_5$ coincidence. The electronics for the $B_5\ B_7$ coincidence circuit began to jam at rates just beyond 10^4 protons per pulse for a spill time of ~ 300 ms. The counting ratios $B_1/B_5\ B_7$, $B_5/B_5\ B_7$, $B_7/B_5\ B_7$, and $B_1\ B_5/B_5\ B_7$ were constant below this intensity, but increased about 5% between 1.5×10^4 and 1.5×10^5, except $B_1\ B_5/B_5\ B_7$ which showed a decrease < 1%. Therefore, it was desirable to use a 2' x 2' x 6' block of heavy concrete to attenuate the EPB for beam intensities above 10^4 protons per pulse. This block was located 8' upstream from the B_5 counter, and

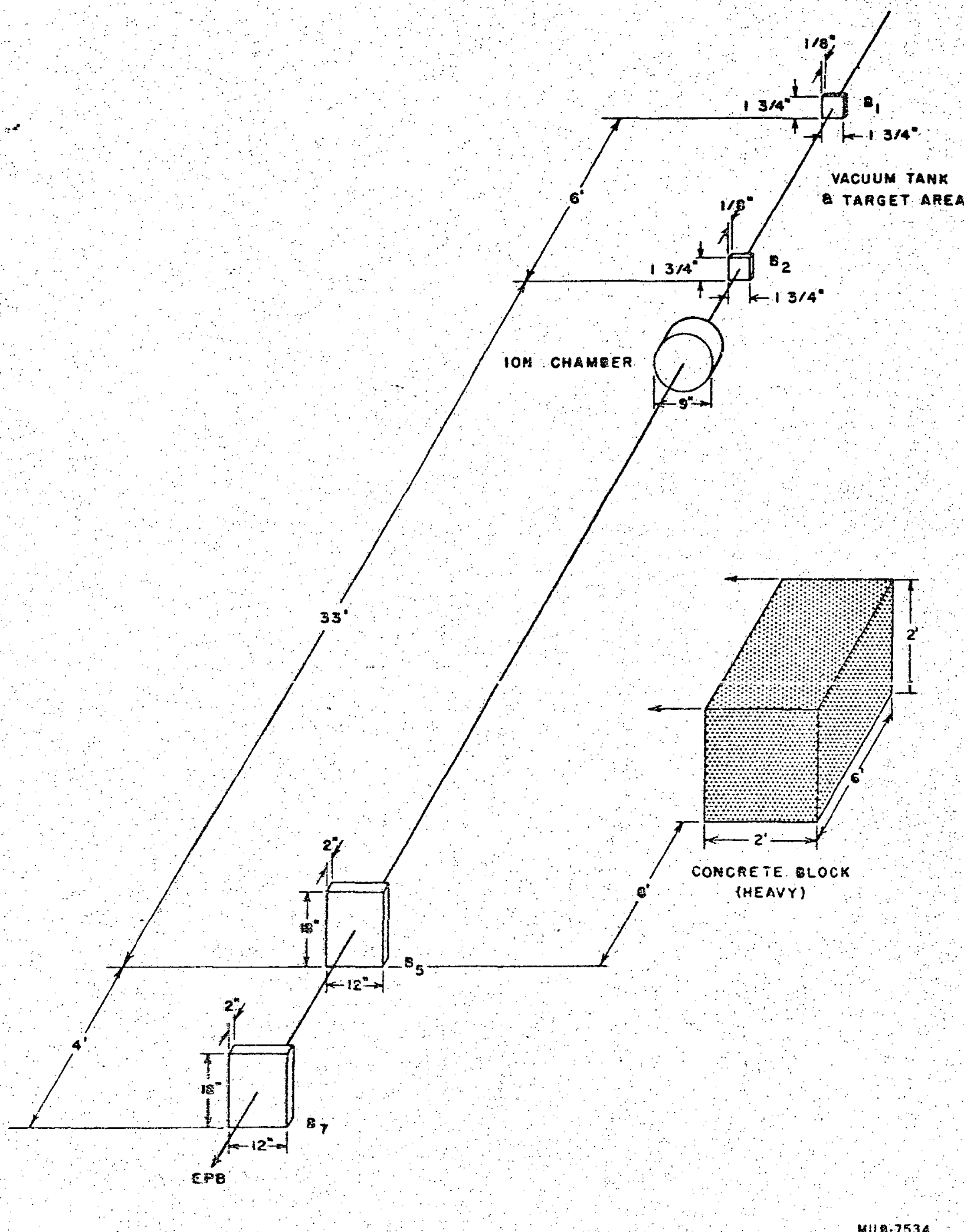

Fig. 12. The scintillation counter arrangement for the calibration of the ionization chamber, showing the concrete block used for attenuation.

could be easily moved into the beam. The 6' thickness of the block and the .01 steradian solid angle subtended at it by B_7 gave an attenuation factor of $\sim 10^{-2}$. This was sufficient to provide the necessary overlap with the ion chamber at 10^6 protons per pulse.

Data were taken with the EPB focused at B_1 and then again at B_2. For the focus at B_1 the two fold coincidence of B_5, B_7 was used to normalize counts from B_1 and also counts from the B_1,B_5 coincidence. These data were obtained at incident beam intensities of 10^2 to 10^4 protons per pulse with the concrete out. With the block in the beam data was again taken at these beam intensities to calculate the attenuation in the block. The intensity was then increased to 10^6 where the ion chamber was read in micro-Coulombs and normalized by the B_5,B_7 coincidence.

The calibration constant is then

$$N/Q = [(B_1B_5/B_5B_7)/(B_1/B_5B_7)]_{\text{block out}} \times [(B_1/B_5B_7)/(Q/B_5B_7)]_{\text{block in}}$$

in protons/micro-Coulomb where the ratios were averaged over all intensities within the ranges allowed by the counter efficiencies. Similarly, data were taken for a focus at B_2, where the appropriate expression for calculating the calibration constant is exactly as above with the replacement of B_1 with B_2.

The calibration constants calculated in this fashion for the incident momenta 3, 5 and 7 BeV/c are summarized in Table 1. The errors shown depend principally on the uncertainty in the focusing of the EPB and the statistical error in the measurements. However, the reproducibility of the measurements due to the focusing uncertainty at the target and scintillators was the dominant source of error. The design characteristics and operating parameters of the ionization chamber are given in Appendix B.

TABLE 1.

P_o in BeV/c	Counter	N/Q in protons/micro-Coulomb	
3.0	B_1	1.45×10^{10}	± 3.5%
3.0	B_2	1.30×10^{10}	+15% - 0.0%
5.0	B_1	1.48×10^{10}	± 2.0%
7.0	B_1	1.42×10^{10}	± 2.1%
7.0	B_2	1.42×10^{10}	± 2.1%

IV. ANALYSIS

The systematics of the Low Momentum Channel and the two modes of the High Momentum Channel were sufficiently distinct as to require an almost unique analysis of the respective data. This was particularly true of the various corrections, their calculation, and their relative importance. However, it is shown in Appendix F that the differential cross-section is represented by

$$d\sigma/d|t| = C(N_S/N_I)/(n_t\ \beta_1\ \Delta\Phi\ \Delta P_1) \qquad (1)$$

in mb/(BeV/c)^2. Even so, the determination of the various parameters depends on the systematics of the particular mode used. In this expression,

N_S = No. of scattered protons at the detector,

N_I = No. of incident protons seen by the ion chamber (beam monitor,

n_t = Target thickness expressed in number of protons/mb,

β_1 = Lab velocity/c for the scattered protons.

$\Delta\Phi$ = Azimuthal angle allowed by the vertical aperture limits of the system,

ΔP_1 = The momentum bite determined by the system, and

$C = \pi/m_oc = 3.3485$ for m_oc in BeV/c.

The number of incident beam particles N_I was read from a continuous pen recorder that indicated the output of an integrating electrometer connected to the ionization chamber. This gives

N_I = (integrator reading in volts)

x (capacitance in μf)

x (calibration constant in counts/μ Coul.)

= Number of particles counted.

In general, the calibration constant is a function of position along the EPB because of the focusing characteristics of the beam. Therefore, the calibration constant used was an interpolation of the B_1 and B_2 values in Table 1.

Low Momentum Channel

These data were taken with the hydrogen gas target. It is convenient therefore to express the parameter n_t of the general relation as $n_t = \ell_g \rho$, where ℓ_g is the effective target length in centimeters and ρ is the density of the gas expressed in protons/(mb–cm). The effective length is related to the brass collimator gap and the scattering angle by $\ell_g = \text{gap}/\sin\theta_1$, where the gap was set at 5.152 cm. The density of the gas was determined by

$$\rho = \rho_o\,(T_o/P_o)(P/T) \qquad (2)$$

where

P = pressure of the gas in inches of H_g,

P_o = 29.92 inches of H_g,

T = absolute temperature,

T_o = 273.16 degrees Kelvin,

ρ_o = density at S.T.P. = .53713 x 10^{-7} protons/(mb–cm).

The target pressure was obtained in inches of Hg with a mercury Manometer. The temperature was measured by a thermistor bridge calibrated by a mercury thermometer. The calibration of the brass collimator, copper collimator, and thermistor bridge is given in Appendix B.

The parameter β_2 is the lab velocity at the detector and is related to the observed particle momentum P_2 by $\beta_2 = (P_2/M)/\sqrt{(P_2/M)^2 + 1}$. The momentum was defined by the vertical spectrometer through careful pre-tuning and current calibration of the magnetic elements of the system and the proper positioning of the brass collimator. Unlike the systematics of the HMC, position of the target did not define the production kinematics, rather it was calculated from p-p kinematics for elastically scattered protons of a given initial momentum P_1, where the energy loss in the target and window relates P_1 to P_2 by the range relation derived in Appendix C giving

$$P_1 = \exp\left\{\ell n\ b + n\ \ell n\ [\Delta R + \exp(\ell n\ P_2/b)/n]\right\} \qquad (3)$$

with ΔR given by

$$\Delta R = \Delta r + \ell_S \rho. \qquad (4)$$

The effective length in H_2 gas for the .001" mylar window was found to be $\Delta r = 1.33\ mg/cm^2$. The distance traversed in H_2 gas by the scattered beam in exiting from the target is given by

$$\ell_S = 16.5\ cm/\sin\theta_1, \qquad (5)$$

and ρ is defined by Eq. (2) where $\rho_o = .08988\ mg/cm^3$, giving $\ell_S\rho < 1.77\ mg/cm^3$ or $\Delta R < 3\ mg/cm^2$. The constants n and b are determined from published range-momentum curves.[17]

The azimuthal angle $\Delta\Phi$ determined by the copper collimator is calculated from the matrix for the horizontal bending region given in Appendix D. This gives the phase space at the aperture as a function of the source vectors. Therefore, using the appropriate matrix element

$$\Delta\Phi \approx \tan \Delta\Phi = y_c'/\sin \theta_1 = y/(S_{44} \sin \theta_1), \tag{6}$$

where y = vertical aperture = 2.5",

$$S_{44} = \ell_a + \ell_t - 2 R_e + R_e \Phi_h \cot(\Phi_h/2). \tag{D-25h}$$

In this expression

ℓ_t = 24"/sin θ_1 for the distance from the center of the bending magnet to the target,

ℓ_a = 21.57" for the distance from the center of the bending magnet to the aperture,

R_e = 14.55" for the effective radius of the magnet, and

$\Phi_h = (69.5^\circ - \theta_1)$ for the horizontal angle of deflection.

It is important to note that ℓ_t was measured along θ_1 to the EPB or actual target.

The momentum bite of the observed momentum P_2 was determined by the vertical dimension of the L_1 or L_2 counters depending on the detector that was used.

An expression for this is derived in Appendix E, where it is shown that

$$\Delta P_2 = P_2 \cdot w/L \tag{E-7}$$

where w is defined as the vertical dimension of the defining scintillator. It has the values

w_1 = 1.985" for the L_1 counter and

w_2 = 1.506" for the L_2 counter.

The parameter L is given by

$$L = \ell_{eff} \sin(\Phi_v/2) + 2d \sin(\Phi_v/2) \cos(\epsilon - \Phi_v/2)/\cos\epsilon, \tag{E-8}$$

where d is defined as the field free distance along the optic axis from the effective exit face of the H_1 bending magnet to the defining scintillator. It has the values

d_1 = 18.905" for the L_1 counter and

d_2 = 22.905" for the L_2 counter.

Also,

ℓ_{eff} = 46" for the effective pole tip length of the M_1 magnet, and

Φ_v = 45.2° for the vertical deflection of the M_1 magnet.

The parameter ϵ was obtained empirically from the optics and geometry of the H_1 magnets and is referred to as the wedge angle. The pole faces of the vertical bending magnet were rectangular, in which case the wedge angles ϵ_1 and ϵ_2 at the entrance and exit are equal to $\Phi_v/2$ for a symmetrical orientation of the magnet about the turning point of the scattered beam. However, because of the large deflection of 45.2°, the entrance and exit of the scattered beam was somewhat below the centerline of the magnet. Therefore, the effective shape of the pole tip did not appear rectangular because of the fringing field. This led to wedge angles $\epsilon = \epsilon_1 = \epsilon_2 > \Phi/2$ (see a more detailed description of the bending magnet parameters and matrix in reference 18 and in Appendix D). Using the bending element matrix and the measured focal length of f = 400" for the H_1 magnet, it is shown in Appendix E that

$$\tan \epsilon = \left\{ 1 + \cot^2 \Phi_v - \rho/(f \sin \Phi_v) \right\}^{1/2} - \cot \Phi_v \qquad \text{(E-11)}$$

In order to correct for accidentals in the detector system, the data were taken alternately with H_2 gas in and then with the target container evacuated. Therefore,

$$\frac{d\sigma}{d|t|} \propto \frac{N_s}{N_I} = \left(\frac{N_s}{N_I}\right)_{H_2} - \left(\frac{N_s}{N_I}\right)_{vac} \qquad (7)$$

The attenuation of the scattered beam by the gas target and window, which together were less than 3 mg/cm^2 in equivalent H_2, can be shown to be very small compared with the statistics and was therefore neglected.

The geometry of the LMC was such that it allowed a small part of the rate at the lower momenta to be contributed by degraded higher energy particles that penetrated the thin parts of the brass collimator around the gap. This and some scattering from the edges of the brass gap required a -.3% correction to the cross section at 83 MeV/c increasing to −3% at 600 MeV/c. This correction was made by graphical methods using average lengths for scattering and energy loss in the brass.

The correction for the energy loss of the scattered beam in the target and window is most conveniently described by (see Appendix C).

$$\frac{\beta_2\,\Delta P_2}{\beta_1\,\Delta P_1} = \exp\left[\frac{1}{2}\log\frac{(P_1{}^2 + m^2)}{(P_2{}^2 + m^2)} + \frac{(1-2n)}{n}\log\frac{P_1}{P_2}\right], \qquad \text{(C-9)}$$

where the subscript 2 labels the observed parameters and the subscript 1 labels the actual values. The constant n is determined by published range-momentum curves.[17] This correction is + 15% at 83 MeV/c, dropping rapidly to less than 1% at about 300 MeV/c.

Chromatic aberrations and focusing in the quadrupole lead to second-order effects in the phase space at the image plane that have a significant effect on ΔP_1. It is convenient to express this effect in the form $\frac{\Delta P_1}{\Delta P_1'}$ which was found to be $.964 \leq \frac{\Delta P_1}{\Delta P_1'}, \leq .980$ for $83 \leq P_1 \leq 600$ MeV/c, respectively, or a correction of −2.0 to −3.6% in the cross-section. This effect is contained in the product matrix $Q_t = \prod_i Q_i$, where the Q_i are the matrices of the various elements of the LMC system (see Appendix D). The calculation of $\Delta P_1'$ was done by the 7094 program LOTCH. This routine generated a plot at the detection plane for y (vertical to the optic axis) against momentum for orbits passing through the top, bottom, and center of the vertical aperture. In principle this is computed by $X = Q_T X_0$, where

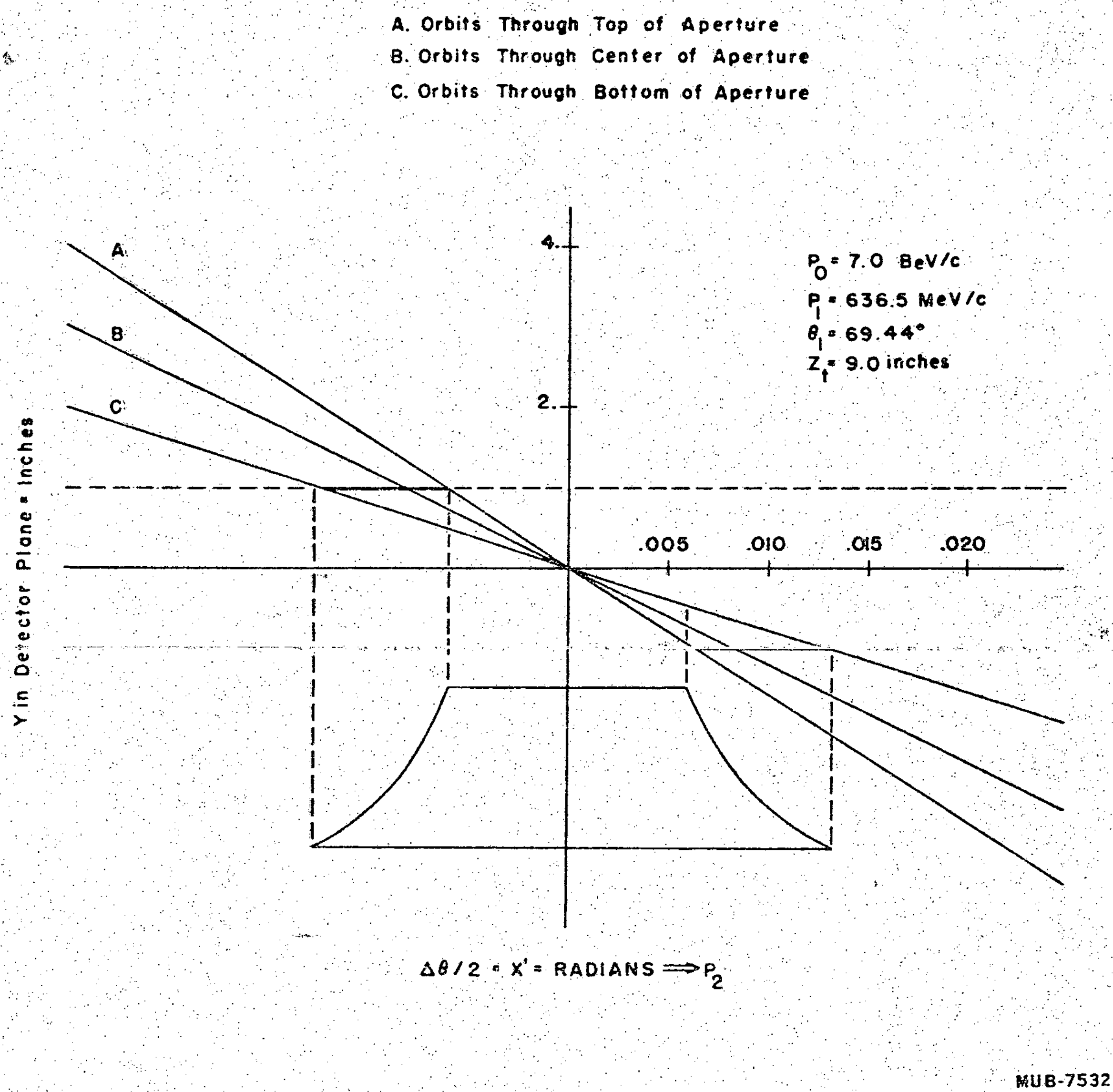

Fig. 13. Plot of y measured vertically in a plane perpendicular to the optic axis at the detector against P_2 calibrated in units of x_0' in radians at the source. Also shown is the superposition of the 2" H_3 counter and the projected momentum distribution with arbitrary normalization for the ordinate.

$$X_o \begin{pmatrix} x_o \\ x_o' \\ y_o \\ y_o' \\ \Delta P/P \end{pmatrix} \quad \text{and} \quad X = \begin{pmatrix} x \\ x' \\ y \\ y' \\ \Delta P/P \end{pmatrix}$$

are the initial and final vectors respectively. Superimposing the counter width on this plot, it is then possible to calculate an arbitrarily normalized intensity distribution for P_1 from which an average width $\Delta P_1'$ can be obtained (see Fig. 13). No correction was required for the Coulomb scattering of the secondary beam in the target and window because of the very large 9" horizontal aperture which was sufficient to accept a broad spatial distribution of the scattered beam at the aperture.

High Momentum Channel

In this channel the initial momentum P_1 of the scattered protons was defined by the location of the target along the EPB. The target position Z_t was taken as the distance from the intersection of the perpendicular from the center of the Sagane magnet to the EPB, to the center of the target looking upstream along the incident beam. Therefore, in Eq. (1) for the cross section, β is uniquely related to Z_t by (see Appendix F)

$$\beta_1 = {}^{P}1/m \Big/ \sqrt{(P_{1/m})^2 + 1} \quad , \tag{8}$$

where

$$P_1 = 2m\,\beta_{cm} \cos\,\theta_1/(1 - \beta_{cm}^2 \cos^2\,\theta_1)$$

for

$$\beta_{cm} = \sqrt{\frac{\gamma_o - 1}{\gamma_o + 1}} \ , \quad \gamma_o = \sqrt{\left(\frac{P_o}{m}\right)^2 + 1} \ ,$$

and

$$\theta_1 = \tan^{-1} \frac{48}{Z_t} \quad (Z_t \text{ in inches and } P_o = \text{incident beam momentum}).$$

The five targets that were used to take data in the HMC are summarized in Table 2. The target thickness parameter n_t of Eq. (1) was given by

$$n_t = (2\ \ell\rho/14.0173) \quad 6.0248 \times 10^{-4} =$$

Hydrogen Atoms/mb for the polyethylene target.

N_I is given by the ion chamber reading in μ Coul multiplied by the calibration constant given in Table 1.

TABLE 2

Target	$\ell\rho$ = gram/cm^2	Thickness
P_2 (CH_2)	2.3735	1"
P_1 (CH_2)	2.3737	1"
P_4 (CH_2)	.5701	1/4"
C_2 (carbon)	2.6806	1/2"
C_{10} (carbon)	.6884	1/8"

Crossover Mode

In this mode of the HMC the momentum bite ΔP_2 of the observed scattered beam was defined by the vertical dimensions of the H_3 counter which was horizontally oriented for these data (see Fig. 7). Using a matrix representation of the magneto-optical system (Appendix D) the 7094 program HITCH was used to calculate ΔP_2 from the optics of the Crossover Mode and the detector width. Therefore using the scheme described for the LMC, ΔP_2 was obtained as the width of the distribution of P_2 against y measured vertically at the detector. Figure 13 is an example of one of these graphs.

The proton–proton elastic scattering cross section is obtained by subtraction of the polyethylene and carbon target data. This is expressed by

$$\frac{d\sigma}{d|t|} = \left\{ E_p \left[\left(\frac{N_s}{N_I}\right)_p - \left(\frac{N_s}{N_I}\right)_b \right] - E_c C_m \left[\left(\frac{N_s}{N_I}\right)_c - \left(\frac{N_s}{N_I}\right)_b \right] \right\} \left(\frac{\pi}{m_o c}\right) \Big/ \left(n_t \cdot \beta_1 \cdot \Delta\varphi \cdot \Delta P_2\right) \qquad (9)$$

where

E_p = the combined correction to the polyethylene data

E_c = the combined correction to the carbon data.

The constant C_m is the carbon target matching ratio for the number of equivalent carbon atoms/cm^2 in the polyethylene target. This is given by

$$C_m = \left(\frac{6}{7}\right) (\ell_p \rho_p) \,/\, (\ell_c\, \rho_c)\ . \qquad (10)$$

The subscripts throughout are p for polyethylene, c for carbon, and b for background. The "target out" data $\left(\frac{N_s}{N_I}\right)_b$ was constant with little scatter over the entire Crossover Mode range at each incident momentum. However, the background subtraction becomes very important at the larger momentum transfer where small differences become involved. The combined correction E represents the product of the energy loss correction, the attenuation correction, and the correction for truncation of the angular distribution of the scattered beam from horizontal aperture stopping in the quadrupole and in the vacuum transport pipe downstream from the bending magnets.

The azimuthal angle $\Delta\Phi$ was determined by the vertical dimension of the collimator. The dependence of $\Delta\Phi$ on θ_1 is given by Eq. (6) where

$$\ell_t = 48'' / \sin\theta_1$$

$$\ell_a = 86.625''$$

$$R_e = 22.6''$$

$$\Phi_h = 33.5^\circ - \theta_1$$

$$y = 3.038''.$$

The energy loss in the target is conveniently expressed by

$$\frac{\Delta P_2}{\Delta P_1} = \exp\left[\left(\frac{1-n}{n}\right) \ln \left(\frac{P_1}{P_2}\right) \right], \tag{11}$$

where the observed momentum is given by (see Appendix C)

$$P_2 = \exp\left\{ \ln b + n \ln \left[-\Delta R + \exp\left(\frac{1}{n} \ln \frac{P_1}{b}\right) \right] \right\}. \tag{12}$$

In this expression b and n are functions of the scattered momentum P_1. As in Eq. (3) these parameters are determined by the range curves. The average path transversed by the scattered beam in leaving the target is given in g/cm^2 by

$$\Delta R = \frac{w}{\cos\theta_1}, \text{ for } 0 \leq \tan\theta_1 \leq \frac{a}{2w}, \tag{13}$$

$$\Delta R = \frac{w}{\cos\theta_1} \left\{ 1 + \frac{a}{2h} - \frac{a^2}{4hw} \cot\theta_1 + \frac{a^3 \cot^2\theta_1}{24hw^2} - \frac{w}{3h} \tan\theta_1 \right\} \text{ for} \tag{14}$$

$$\frac{a}{2w} < \tan\theta_1 \leq \frac{(a + 2h)}{2w},$$

$$\Delta R = \frac{(a + h)}{\sin\theta_1} \left\{ 1 - \frac{(a^2 + 2ah + \frac{4}{3} h^2)}{4w\,(a + h)} \cot\theta_1 \right\} \text{ for } \frac{a + 2h}{2w} \leq \tan\theta . \tag{15}$$

In these relations

$w = \ell\rho/2$ for the target in g/cm^2,

$h = 1/2$ the width of the incident beam in effective g/cm^2 of target,

$a = 1/2$ the width of the target minus h in g/cm^2.

The correction for attenuation of the scattered beam in the target is partially offset by the correction for attenuation of the incident beam. Even so their combined effect is significant in the lower momentum region of 500 to 800 MeV/c. This is expressed by

$$\frac{(\text{observed incident beam})}{(\text{initial incident beam})} \times \frac{(\text{initial scattered beam})}{(\text{observed scattered beam}} = \exp\left[\sigma_n \ (\Delta R - w)\right] . \qquad (16)$$

The total nucleon cross section σ_n for the carbon and polyethylene was taken from F. F. Chen, et al.[19,20]

As shown in Fig. 7, the H_3 and H_4 counters were split into left and right sections. These were wrapped independently to provide left, right balancing capability for tuning the channel in both modes. This choice led to a small dead space between the left and right counters of about 1/32". In this mode the dead space requires a correction to the cross section of ~ +1.3%.

The correction for horizontal aperture stopping is obtained by evaluating the angular acceptance of the beam transport system in terms of X_o', and then comparing this acceptance to the angular distribution of the scattered beam intensity projected on the source. The cross section is corrected for that part of the distribution which is outside of the angular region accepted by the system. Figure 14 shows the dependence of this distribution on the scattered momentum P_1 and the thickness of the carbon and polyethylene targets. At a given P_1 and for a given target, the angular distribution of the scattered beam is a fold of three independent

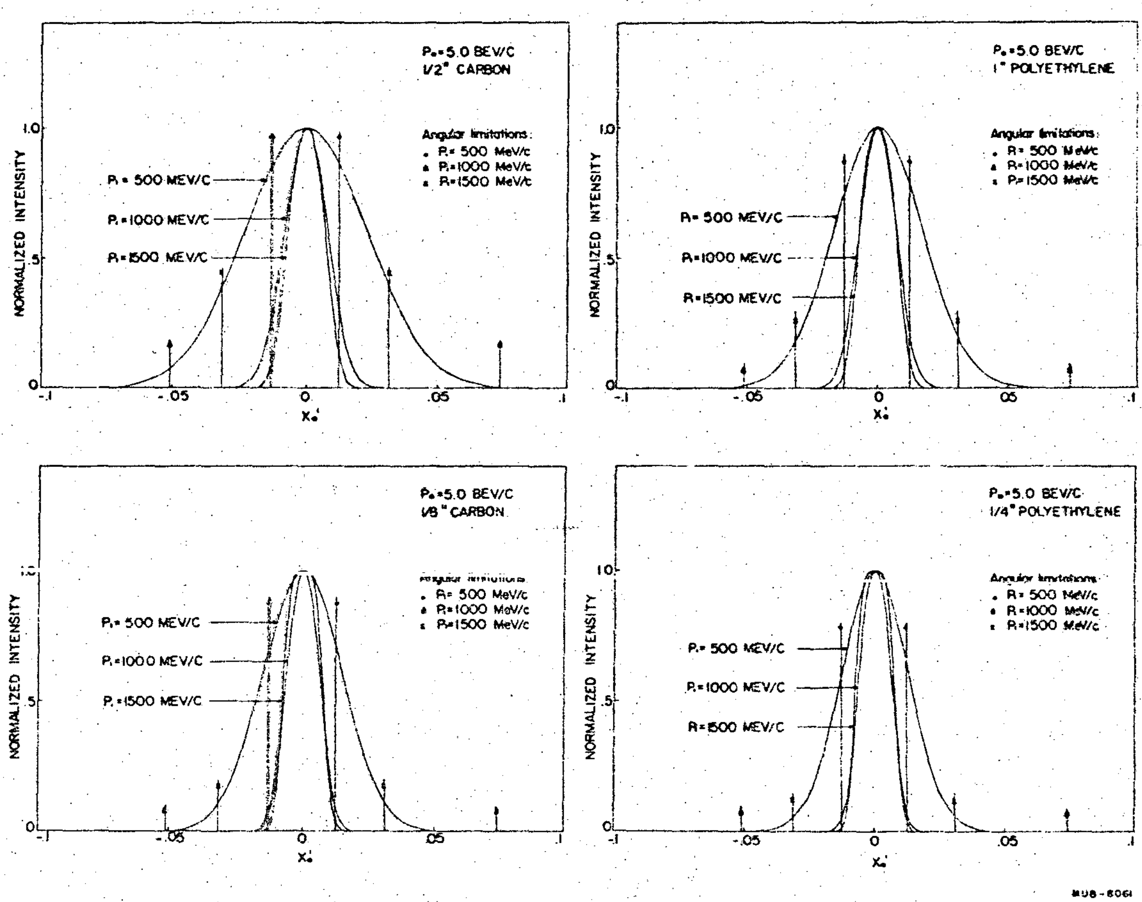

Figure 14. The angular distributions of the scattered beam intensity projected on the source plane for the Crossover Mode. The cut off areas represent the part of the distribution which would also have been seen by the detection but is lost due to the limited angular acceptance of the beam transport system. These curves illustrate the stopping of the system for a point source.

effects: the effective source distribution arising from the finite target size; the angular spread of the secondary beam due to coulomb scattering in the target; and a momentum distribution about P_1 determined to first order by the detector width and by significant second order optical effects. This fold is a triple integral which depends, among other things, on the geometry of the system and the beam optics. The calculation was performed on the 7094 using the program ERRTOT which incorporated HITCH as a subroutine for the computation of those parameters depending on the optics of the system. The triple integrals may be written

$$A_o = \int_{\eta_1}^{\eta_2} \int_{-\infty}^{\infty} \int_{-\infty}^{\infty} y_1(x_1)\, y_2\,(x_2')y_3\,(x_3'-x_2')\, dx_3'\, dx_2'\, dx_1 \tag{17a}$$

$$A_t = \int_{\eta_1}^{\eta_2} \int_{s_1(x_1)}^{s_2(x_1)} \int_{-\infty}^{\infty} y_1(x_1)\, y_2\,(x_2')y_3\,(x_3'-x_2')\, dx_3'\, dx_2'\, dx_1\ , \tag{17b}$$

where the y's are the probability distribution given by

$y_1(x_1) = \mathbb{P}_1\,(\delta\eta)$	for the effective spatial distribution of the target,
$y_2(x_2') = \mathbb{P}_2\,(\delta\theta_c)$	for the angular distribution of the coulomb scattering,
$y_3\,(x_3') = \mathbb{P}_3\,(\delta p)$	for the unobstructed momentum distribution which (without stopping in the system) would be seen by the detector.

The η_1 and η_2 are the spatial limits of the source and $s_1(x_1)$ and $s_2(x_1)$ are the acceptance limits of the system.

The dummy variables are taken along the horizontal axis at the source and

$$\delta\eta = x_1 = \text{inches}$$

$$\delta\theta_c = -x_2' = \text{radians}$$

$$\delta p = \frac{\delta P_1}{P_1} = x_3' \left[\frac{-1}{P_1}\ \frac{dP_1}{d\theta_1}\right] ,$$

where Eq. (F–30) gives

$$-\frac{1}{P_1}\ \frac{dP_1}{d\theta_1} = -\tan\theta_1 \left[(1+\beta_{cm}^2 \cos^2\theta_1)/(1-\beta_{cm}^2 \cos^2\theta_1)\right] . \tag{18}$$

The distribution $\mathbb{P}_1\ (\delta\eta)$ for the effective target is given by an isosceles trapezoid resulting from the rectangular shape of the actual target. The top of this distribution is then given by

$$b_1 = \left| w \sin\theta_1 - h \cos\theta_1 \right| , \tag{19}$$

and the base by

$$b_2 = w \sin\theta_1 + h \cos\theta_1 . \tag{20}$$

Therefore the limits of integration η_1 and η_2 of Eq. (17) are given by

$$\eta_1 = -b_2/2 , \tag{21a}$$

$$\eta_2 = +b_2/2 . \tag{21b}$$

The coulomb scattering distribution $\mathbb{P}_2\ (\delta\theta_c)$ is well approximated by a gaussian for the relatively short exit paths traversed in the targets. Therefore

$$\mathbb{P}_2\ (\delta\theta_c) \propto \exp\left(-\ \delta\theta_c^2/2\Delta\theta_c^2\right) \tag{22}$$

where

$$\Delta\theta_c = \frac{21}{P_1\ \beta_1}\sqrt{\frac{\Delta R}{L_{rad}}}$$

with

ΔR = average length traversed in exit,

L_{rad} = radiation length of the material,

β_1 = lab velocity of the scattered protons, and

P_1 = momentum of the recoil proton in MeV/c

The distribution P_3 (δp) for the momentum spread was computed from beam optics by the 7094 program HITCH in connection with the computation of its width. That is, in the calculation of ΔP_2 illustrated in Fig. 13.

The angular acceptance limits $s_1(x_1)$ and $s_2(x_1)$ were computed by a modified version of HITCH called VIGNET. This is a CDC 6600 system which uses the matrix representation of the optics to determine the maximum possible angular excursions for protons as a function of position (x_o) on the target for each geometry.

The form (A_o/A_t) of the acceptance correction makes the normalization of the three distributions entirely arbitrary. The combined correction due to the energy loss, attenuation, and the horizontal acceptance was then applied in the form

$$E = (\text{Energy loss}) \times (\text{Attenuation}) \times (\text{Acceptance}).$$

This is a function of the target geometry and material. Therefore, as shown in Eq. (9) it is necessary to apply this to the carbon and polyethylene cross sections before subtraction. These corrections are summarized in Table 3. Additional corrections must be applied to these cross section data for inelastic background and counting inefficiency. In the region of the Crossover Mode data this background is closely parameterized by

$$C_B = 1 - t^2/72. \tag{23a}$$

For counting inefficiency due to high particle rates at the H_2 counter

$$C_c = 1.013, \tag{23b}$$

where both C_B and C_c are then applied directly to the numbers obtained from Eq. 9 for the final cross sections.

Parallel Mode

In this mode ΔP_1 is determined by the horizontal dimension ΔX of the aperture. From the matrix for the Sagane magnet given in Appendix D

$$\Delta X = \Delta\theta_1 \cdot S_{12} + \frac{\Delta P_1}{P_1} \cdot S_{15} \tag{24}$$

for

$$S_{12} = \ell_t + \ell_a - 2\,\ell_t\,\ell_a \sin^2(\Phi_h/2)/Re \tag{D-25b}$$

$$S_{15} = -\ell_a \sin\Phi_h\ . \tag{D-25c}$$

From P–P elastic kinematics(16)

$$f(\theta_1, \beta_{cm}) = \frac{-\Delta P_1}{P_1\Delta\theta_1} = \tan\theta_1 \left[(1 + \beta_{cm}^2 \cos^2\theta_1)\Big/(1 - \beta_{cm}^2\cos^2\theta_1)\right]. \tag{25}$$

By substitution

$$\Delta P_1 = -\Delta X \cdot P_1\Big/\left\{\left[S_{12}/f\,(\theta_1,\beta_{cm})\right] - S_{15}\right\}, \tag{26}$$

for

$$\Delta X = 3.0''\ .$$

For the calculation of the cross section it is convenient to use the form given in Eq. 1 with

$$N_S/N_I = (\cos\delta/w_c)\int (n_s/n_i)\,(dy/dP_1)\,(dP_1/dI)\,dI \tag{27a}$$

where

$$n_s/n_i = (n_s/n_i)_{OH_2} - C_m\,(n_s/n_i)_{carbon} \tag{27b}$$

for the polyethylene–carbon subtraction. The factor

$\cos\delta/w_c$

TABLE 3.

E_0, BeV/c	Target	P_s, BeV/c	Attenuation	Energy Loss	Aperture	Combined
3.0	1/4"-CH_2	.500	1.009	1.047	[illegible]	1.262
		1.000	1.003	1.004	1.000	1.007
		1.500	1.002	1.002	1.000	1.004
		2.000	1.001	1.001	1.000	1.002
	1/8"-Carbon	.500	[illegible]	1.060	[illegible]	1.350
		1.000	1.004	1.005	1.000	1.009
		1.500	1.002	1.002	1.000	1.004
		2.000	1.001	1.001	1.001	1.004
	1"-CH_2	1.000	1.005	1.014	1.000	1.019
		1.500	1.004	1.007	1.000	1.012
		2.000	1.003	1.004	1.033	1.040
	1/2"-Carbon	1.000	1.012	1.020	1.000	1.031
		1.500	1.006	1.009	1.001	1.017
		2.000	1.005	1.005	1.037	1.046
5.0	1/4"-CH_2	.450	1.011	1.081	1.977	2.161
		.500	1.010	1.052	1.490	1.583
		.600	1.008	1.025	1.062	1.096
		.800	1.005	1.009	1.000	1.014
		1.000	1.004	1.005	1.000	1.009
		1.500	1.003	1.002	1.000	1.005
		2.000	1.002	1.001	1.000	1.003
	1/8"-Carbon	.450	1.015	1.109	[illegible]	2.552
		.500	1.014	1.068	[illegible]	1.300
		.600	1.011	1.032	1.105	1.153
		.800	1.007	1.011	1.000	1.017
		1.000	1.005	1.006	1.000	1.011
		1.500	1.003	1.003	1.000	1.006
		2.000	1.002	1.001	1.000	1.004
	1"-CH_2	.800	1.005	1.042	1.000	1.047
		1.000	1.005	1.014	1.000	1.019
		1.500	1.006	1.007	1.000	1.013
		2.000	[illegible]	1.004	1.000	1.009
	1/2"-Carbon	.800	1.017	1.033	1.001	1.051
		1.000	1.014	1.021	1.000	1.035
		1.500	1.011	1.010	1.000	1.020
		2.000	1.008	1.005	1.000	1.014
7.0	1/4"-CH_2	.450	1.012	1.084	[illegible]	[illegible]
		.500	1.011	1.054	1.653	1.792
		.600	1.008	1.026	1.116	1.157
		.800	1.006	1.009	1.000	1.015
		1.000	1.004	1.005	1.000	1.010
		1.400	1.004	1.002	1.000	1.006
		2.000	1.002	1.001	1.000	1.004
	1/8"-Carbon	.450	1.017	1.115	[illegible]	[illegible]
		.500	1.015	1.072	[illegible]	2.063
		.600	1.011	1.034	1.154	1.238
		.800	1.007	1.001	1.000	1.009
		1.000	1.005	1.007	1.000	1.012
		1.400	1.004	1.003	1.000	1.007
		2.000	1.003	1.001	1.000	1.004
	1"-Carbon	.800	1.005	1.042	1.002	1.049
		1.000	1.005	1.014	1.000	1.020
		1.400	1.004	1.008	1.000	1.014
		2.000	1.005	1.004	1.000	1.010
		.800	1.017	1.034	1.007	1.060
		1.000	[illegible]	1.020	1.000	1.037
		1.400	1.013	1.011	1.000	1.024
		2.000	1.010	1.005	1.000	1.015

is the vertical dimension of the H_2 scintillator seen by the scattered beam when the counter is oriented at the appropriate angle δ to the horizontal in a plane perpendicular to the optic axis. The arrangement of the detector system and the definition of δ is illustrated in Fig. 7. The counter width is given by

$w_c = 3.0''$.

The variable of integration I is the current in equivalent milli-Volts for a known shunt resistance of the C_1 and C_2 vertical bending magnets. Throughout both modes of the High Momentum Channel these magnets were operated in tandem as one momentum spectrometer. The angle of deflection in each was 8.0°, giving an overall deflection of 16.0° for ϕ_v. The quantity

$$dP_1/dI = (\mathrm{MeV}/c)/\text{milli-Volt}$$

is taken from the empirical magnetization curves for the C_1 and C_2 bending magnets. The quantity

$$dy/dP_i = \mathrm{inches}/(\mathrm{MeV}/c)$$

is the dispersion of the momentum spectrometer; it depends to first order on the angle of deflection Φ_v, the central scattered momentum P_1, and the distance S_t from the turning point to the plane of the H_2 counter. Therefore

$$dy/dP_1 \approx P_1/(S_t \cdot \Phi_h) .$$

However, there are significant second order effects that depend on the optical aberrations and focusing of the system, and on the variation of the C_1, C_2 current for the data scan. By using the phase space at the H_2 counter calculated from the Matrix representation of the system, it was found that dy/dP_1 can be represented by

$$dy/dP_1 = (.06245/P_1) \quad (I_o/ I) \tag{28}$$

where I_o is the central value of the C_1, C_2 current.

The abscissas of polyethylene and the carbon data in general do not coincide. Therefore it was desirable to generate a curve for the carbon with which one could perform the subtraction indicated by Eq. 27. Figure 15a is a typical set of data from a spectrometer scan. The ordinate being given in counts at H_2 per number of incident beam protons, and the abscissa in milli-Volts. It is convenient to rewrite Eq. 27 as

$$y_{H_i} = y_{P_i} - y_j \tag{29}$$

for

$$y_{H_i} = n_s/n_i \tag{30a}$$

$$y_{P_i} = (n_s/n_i)_{CH_2} \cdot \tag{30b}$$

The y_j depends on the carbon data points $\left\{y_{c_k}, I_k\right\}$, where

$$y_{c_k} = C_m \, (n_s/n_i)_{carbon} \cdot \tag{30c}$$

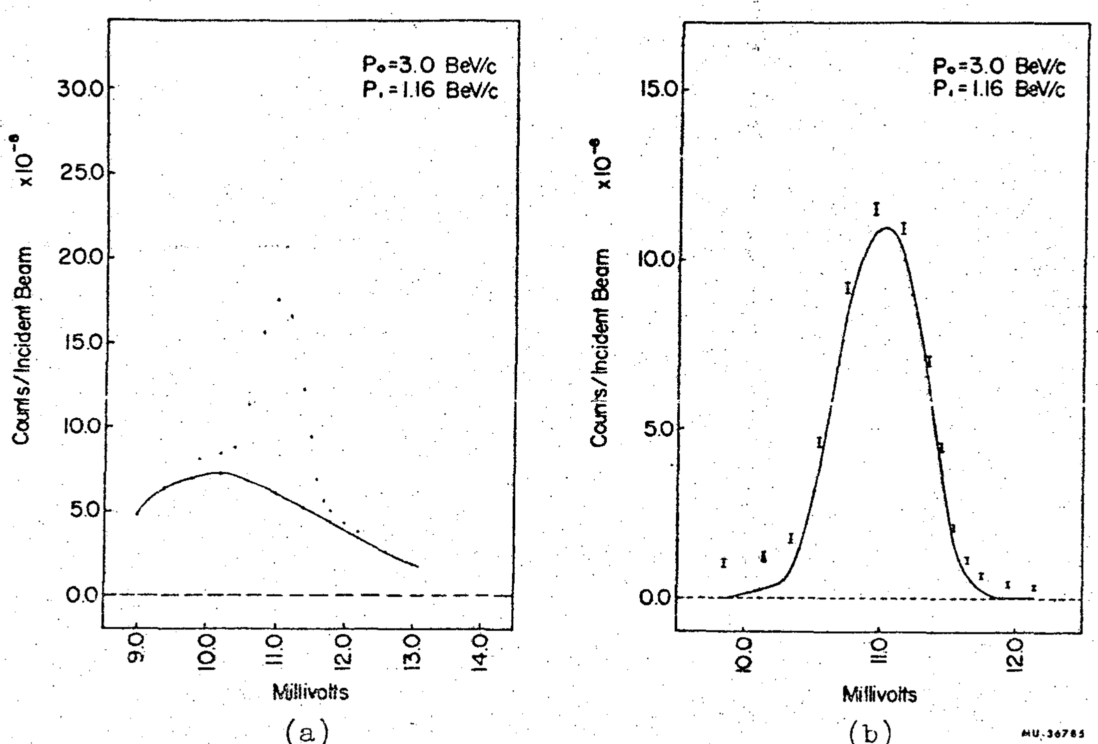

Fig. 15. Raw data from a typical Parallel Mode scan is shown in (a). The upper and lower sets of points were taken by varying the current in the C_1, C_2 bending magnets for the polyethylene and carbon targets respectively. The ordinate is given in raw counts at the H_2 counter per incident beam proton. In addition, the carbon points are normalized by a target matching constant. The carbon background has been subtracted from the points plotted in (b), where the remaining background is due to inelastic p–p scattering. The curve shown is a fit to the final data after subtracting the inelastic background.

Now this curve for the carbon (shown passing through a typical set of data points $\left\{y_{c_k}, I_{c_k}\right\}$ in Fig.15a) is generated from a set of points $\left\{y_j, I_j\right\}$ on a collection of second order polynomials. These quadratics are constrained to pass through the data points, and to be continuous in the value of the functions and their first derivatives. Each point (y_j, I_j) of this curve therefore lies on one of two polynomials each of which is forced to pass through a closest pair of data points $\left(y_{c_k}, I_{c_k}\right)$, one polynomial for the closest pair on the right, and the other for the closest pair on the left of the region of (y_j, I_j). These functions are then matched midway between the 2 innermost of the 4 data point sequence. Therefore y_j is given by a quadratic of the form

$$y_j = a_1 I_j^2 + a_2 I_j + a_3 , \tag{31}$$

where the constants are obtained by inverting the matrix equation

$$Y = MX, \tag{32}$$

for

$$Y = \begin{pmatrix} y_{c_1} \\ y_{c_2} \\ 0 \\ 0 \\ y_{c_3} \\ y_{c_4} \end{pmatrix} \qquad X = \begin{pmatrix} a_1 \\ a_2 \\ a_3 \\ a_4 \\ a_5 \\ a_6 \end{pmatrix} \tag{33}$$

and

$$M = \begin{pmatrix} I_{c_1}^2 & I_{c_1} & 1 & 0 & 0 & 0 \\ I_{c_2}^2 & I_{c_2} & 1 & 0 & 0 & 0 \\ I_m^2 & I_m & 1 & -I_m^2 & -I_m & -1 \\ 2I_m & 1 & 0 & -2I_m & -1 & 0 \\ 0 & 0 & 0 & I_{c_3}^2 & I_{c_3} & 1 \\ 0 & 0 & 0 & I_{c_4}^2 & I_{c_4} & 1 \end{pmatrix} \tag{34}$$

In these expressions the set,

(y_{c_1}, I_{c_1}) ,

(y_{c_2}, I_{c_2}) ,

(y_{c_3}, I_{c_3}) ,

(y_{c_4}, I_{c_4}) ,

are the coordinates of the 4 points selected as described for the region about the point (y_j, I_j) specified by the value of I_1. This parameter is computed from

$$I_j = j \cdot \Delta I ,$$

for

$$\Delta I = (\text{upper bound—lower bound})/100 .$$

The parameter I_m of M is the abscissa for which the quadratics are matched. This is just

$$I_m = (I_{c_2} + I_{c_3})/2 . \tag{35}$$

The statistical error in y_H is given by

$$(\Delta y_{H_i}) = \sqrt{(\Delta y_{F_i})^2 + (\Delta y_j)^2} , \tag{36}$$

where

$$(\Delta y_j)^2 = \sum_{\ell=1}^{4} q_\ell^2 \, (\Delta y_{c_\ell})^2 \Big/ |M|^2 , \tag{37}$$

and the q_ℓ are a linear combination of the elements of the matrix M^{-1} and therefore depend only on the constants I_{c_1}, I_{c_2}, I_{c_3}, I_{c_4}, and I_m.

Figure 15b shows the subtracted data points $\left\{y_{H_i}, I_{H_i}\right\}$ for the original set of Fig. 15a. The curve shown is again generated by a set of points $\left\{y_n, I_n\right\}$. This is now for a collection of second order polynomials constrained to pass through the points $\left\{y_{H_i}, I_{H_i}\right\}$ for the purpose of performing the integration indicated in Eq. 26. This integral is expressed as a finite sum of the form

$$\sum_{n=1}^{200} y_n \, (dy/dP_1)_n \, (dP_1/dI)_n \, \Delta I \tag{38}$$

for convenience in computation, where

$$y_n = a_1 \, I_n^2 + a_2 \, I_n + a_3 - y_{bn} \quad , \tag{39}$$

and the vector Y of the matrix Eq. 32 is now given by

$$Y = \begin{pmatrix} y_{H_1} \\ y_{H_2} \\ 0 \\ 0 \\ y_{H_3} \\ y_{H_4} \end{pmatrix} \quad , \tag{40}$$

and M by

$$M = \begin{pmatrix} I_{H_1}^2 & I_{H_1} & 1 & 0 & 0 & 0 \\ I_{H_2}^2 & I_{H_2} & 1 & 0 & 0 & 0 \\ I_m^2 & I_m & 1 & -I_m^2 & -I_m & -1 \\ 2I_m & 1 & 0 & -2I_m & 1 & 0 \\ 0 & 0 & 0 & I_{H_3}^2 & I_{H_3} & 1 \\ 0 & 0 & 0 & I_{H_4}^2 & I_{H_4} & 1 \end{pmatrix} . \tag{41}$$

The values of y_{bn} are the estimated inelastic background.

The statistical error for the integral is given by

$$\left\{ \sum_{n=1}^{100} \Delta y_n^2 \, (dy/dP_1)_n^2 \; (dP_1/dI)_n^2 \, \Delta I^2 \right\}^{1/2}$$

where

$$\Delta y_n^2 = \sum_{\ell=1}^{4} (q_\ell \cdot \Delta v_{H_\ell})^2 / |M|^2 ,$$

and the q_ℓ are again linear combinations of the constants which are now I_{H_1}, I_{H_2}, I_{H_3}, I_{H_4}, and I_m.

The proton-proton elastic peak overlaps the broad inelastic distribution. This background is shown in figure 16, for each of the H_2, H_3, and H_4 scintillation counters. This effect is given in percent of the elastic cross-section measured under the peak. The absolute normalization of the inelastic background does not, of course, depend on the detector. However, for the purpose of correcting the data, it is desirable to plot it in this form. These curves then represent a best estimate of the inelastic background as averaged over a collection of all the Parallel Mode data. This and data from a more recent experiment by C. M. Ankenbrandt, A. R. Clark, B. Cork, T. Elioff, L. T. Kerth, and W. A. Wenzel [23] are consistent with a smooth, well-defined background under the sharply resolved p-p elastic peaks. The error in the elastic cross-section from the uncertainty in subtracting this contribution to the peak is:

1.76 % for the H_2 counter coincidence,

4.18 % for the H_3 counter coincidence,

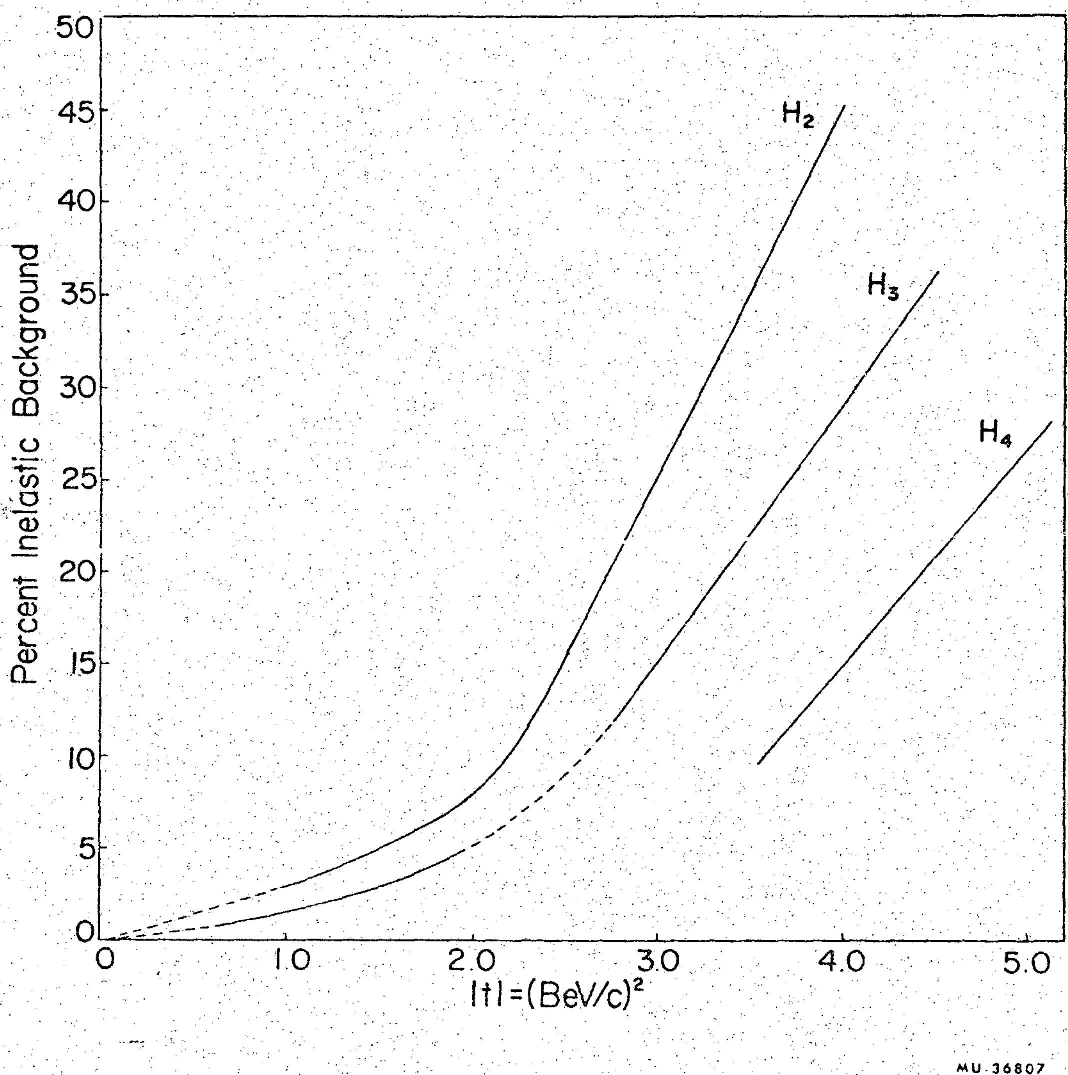

Fig. 16. The inelastic background from raw counts at the detectors for the Parallel Mode in percent of the elastic cross section measured under the peak. The four momentum transfer is given in $(BeV/c)^2$.

4.00% for the H_4 counter coincidence, and

.5% for 3rd Channel coincidence at 90° cm.

For a large part of the 7 BeV/c data of the Parallel Mode, good resolution and low inelastic background were found to be more important than statistics. Therefore it was desirable to use an H_3 or H_4 counter coincidence to obtain the best data for the cross-sections. This choice gave a maximum (raw count) inelastic background of less than 45% of the elastic peak (see Figure 16).

The anti-coincidence counter used as an aperture in this mode (see Fig. 9) was found to jam at normal beam intensities, thus requiring a ~+4.0% correction to the cross section. Therefore it was desirable to operate the system with this counter off. The data was then corrected to aperture (anti-coincidence-counter) turned on geometry by taking calibration data at low beam intensity with this aperture counter both turned on and off. This correction is written for convenience in the form:

$$\frac{(\text{anti-in counter at the detector})}{(\text{anti-out counter at the detector})} \left.\frac{d\sigma}{d|t|}\right|_{out} . \qquad (44)$$

Over the range of 1 to 3.5 BeV/c for the scattered momentum P_1, this correction is .88 to .84 respectively with an uncertainty of 1.5%.

The aperture in this mode must also be corrected for limitations occurring in the quadrupole and in the vacuum beam-transport pipe located downstream from the C_2 bending magnet. For a given value of P_o, P_1 and a given point (x_o, y_o) at the source, the effects of this aperture stopping in the system are calculated from the matrix representation using the VIGNET code on the 7094. For the accuracy desired, a sufficient number of apertures through the quadrupole elements are projected on the source along with the limiting "neck" of the transport pipe. This neck was a narrow-section of the HMC beam transport pipe located 12" downstream from the vertical bending magnets (see Fig. 10). These projections are plotted in

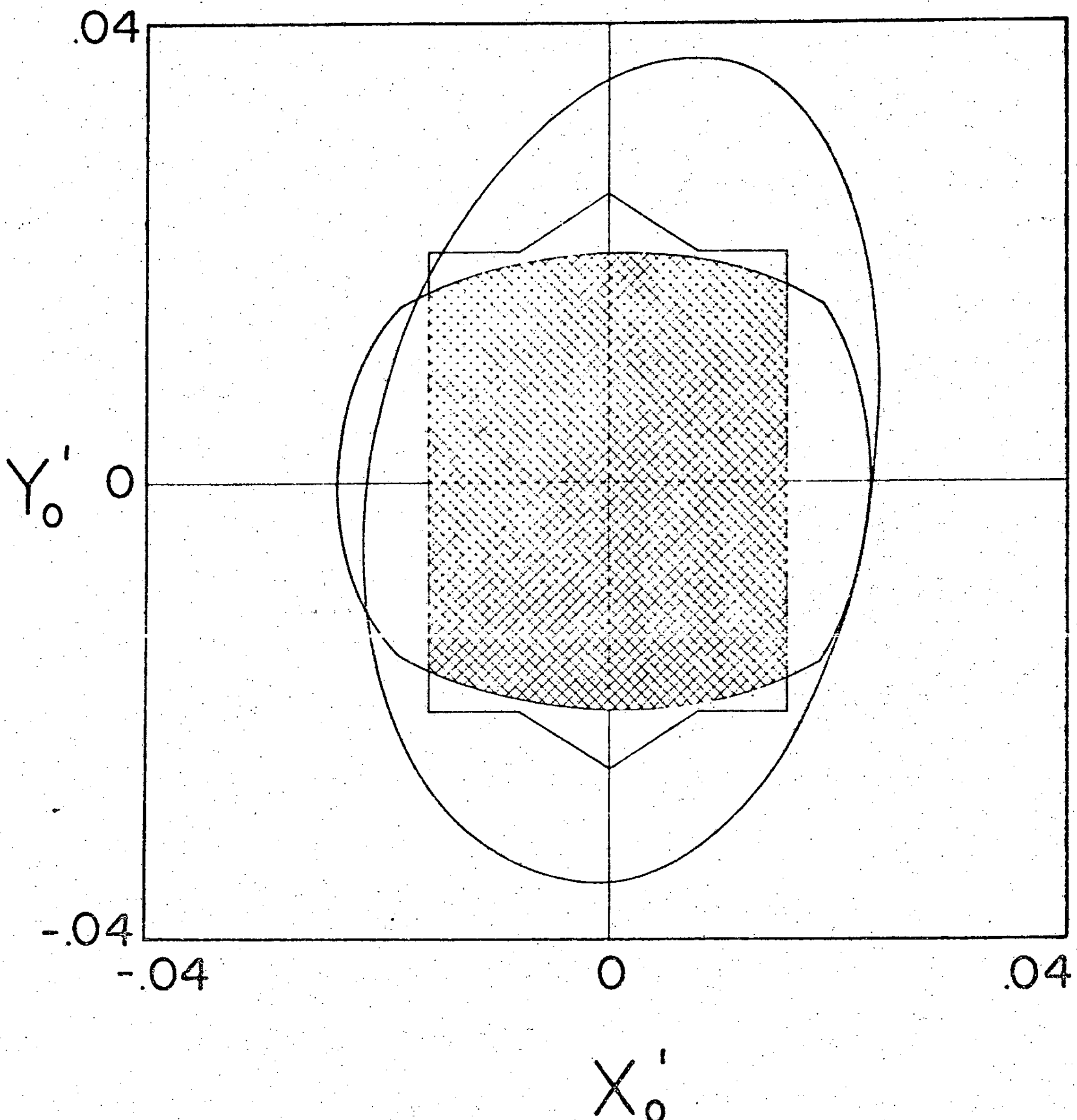

MU-36791

Fig. 17. The superposition of the effective apertures due to the pipe neck, quadrupole, and anti—counter aperture for their projections on the x_o', y_o' plane at the source, the curve of largest area resulting from a projection of the transport pipe neck. The common area determines the available aperture of the Parallel Mode for a given P_o, P_1, and (x_o, y_o). This figure is for P_o = 3.0 BeV/c, P_1 = 1.16 BeV/c, and $x_o = y_o = 0$.

the x_o', y_o' plane where

$$x_o' = dx_o/dz$$

$$y_o' = dy_o/dz \ ,$$

and where z is the optic axis. The common area obtained from a superposition of these curves and a similar projection of the anti-counter aperture determines the solid angle available to a point (x_o, y_o) at the source. Figure 17 illustrates a superposition of the pipe neck, the effective quadrupole aperture, and the anti-counter aperture projected on the source in the x_o', y_o' plane. Using the transformations

$$x_{oi}' = \rho_i \sin \phi_i$$

$$y_{oi}' = \rho_i \cos \phi_i \ ,$$

The solid angle for a given (x_o, y_o), ρ_o, P_1 is computed from

$$\begin{aligned} \Omega = \int d\Omega &= \iint \rho \left(1 - \frac{9}{8}\rho\right) d\rho \, d\phi \\ &\approx \sum_{i=1}^{N} (\rho_i^2/2)(1 - 3\rho_i/4)\, \Delta\phi_i \end{aligned} \tag{45}$$

where the common area of the superposition is computed in the form of an array $\left\{x_{oi}', y_{oi}'\right\}$ for this final calculation. By varying (x_o, y_o) over the extent of the target, this computer program provides an average solid angle $< \Omega >$ available for each ρ_1, ρ_o. If Ω_A is the solid angle subtended at the source by the anti-counter aperture, then the appropriate correction to the elastic cross-section is

$$[\Omega_A / < \Omega >] \frac{d\sigma}{d\, t} \ . \tag{46}$$

The uncertainty in this correction is ~ .5%.

V. RESULTS

The measured differential cross sections at low-momentum transfer are given in Table 4 in the Lorentz invariant form $d\sigma/d|t|[mb/(BeV/c)^2]$. This table is a collection of all the data taken by LMC with the hydrogen gas target. The error shown represents the combined counting statistics and experimental uncertainties for each point. The significant contributions to the experimental error arise from the combined uncertainties of target density, the determination of θ_1, magnet tuning and stability, and from the uncertainties in the calculation of the experimental corrections to the data (see the analysis section "Low Momentum Channel" for a discussion of these corrections).

The target density, calculated from the measured pressure and temperature of the H_2 gas, had an uncertainty of ± .7%. The azimuthal positioning of the brass collimator for the measurement of θ_1 lead to an uncertainty of ±.2% in these data. Magnet tuning and stability errors were ±.9% for the P_o = 3 BeV/c data and ± 1.6% for the P_o = 5 and 7 BeV/c data. The uncertainty in calculating the experimental corrections to these data lead to an error of ±.9%. These errors added in quadrature give

± 1.5% for P_o = 3 BeV/c data,

± 2.0% for P_o = 5 BeV/c data,

± 2.0% for P_o = 7 BeV/c data,

for the experimental errors.

Of particular interest is the ratio between the real and imaginary parts of the forward scattering amplitude. This may be determined from the coulomb interference with the nuclear scattering amplitude. It is expressed by

TABLE 4

P_o, (BeV/c)	$d\sigma/d\|t\|$ mb/(BeV/c)^2	$\|t\|$ (BeV/c)^2	Error ±%
3.0	121.2	.01083	1.80
	112.3	.01617	1.77
	105.9	.02282	1.80
	97.01	.03072	1.76
	91.33	.03965	1.68
	78.41	.06163	1.72
	66.10	.08796	1.66
	53.16	.1186	1.72
	42.74	.1534	1.70
	32.14	.1921	1.73
	24.84	.2345	1.75
	19.06	.2803	1.74
	13.69	.3293	1.76
5.0	106.5	.01081	2.34
	96.85	.01615	2.28
	85.89	.02281	2.37
	74.95	.03984	2.23
	8.660	.3293	3.09
7.0	98.89	.01081	2.22
	91.17	.01615	2.14
	82.27	.02281	2.22
	74.96	.03072	2.15
	70.54	.03984	2.15
	63.96	.05015	2.14
	56.89	.06163	2.11
	45.89	.08796	2.13
	37.48	.1186	2.12
	27.75	.1534	2.07
	15.59	.2345	2.24
	10.62	.2803	2.10
	7.732	.3293	2.23

TABLE 5

	$P_o = 3.0$	$P_o = 5.0$	$P_o = 7.0$
σ_T = mb	43.60 ± 2.0%	41.10 ± 1.4%	40.30 ± 1.4%
$\frac{d\sigma}{d\|t\|}\Big\|_{O.P}$ = mb/ (BeV/c)^2	96.49	85.74	82.44
A= (BeV/c)$^{-2}$	6.50 ± .5%	7.44 ± .6%	7.69 ± .4%
ρ = real/imaginary	-.426 ± 11 %	-.389 ± 8 %	-.339 ± 11 %
χ^2 percentage points	.77	.14	.06
Number of data points	13	5	13
E^2_{cm} = (BeV)^2	7.66	11.31	15.01

$$d\sigma/d|t| = |f_n + f_c|^2. \tag{47}$$

The coulomb scattering amplitude adapted from H. A. Bethe is[24]

$$f_c = \frac{c_o}{\beta_1 |t|} \; (1 + i\,\epsilon), \tag{48}$$

with

$c_o = -.01617$

β_1 = laboratory velocity of scattered proton/c

$\epsilon = .0073 \; \ell n \; (.0437/|t|)$.

From recent work it has been shown that a purely imaginary spin dependent form for the forward scattering amplitude is entirely inadequate to describe the behavior of the angular distributions at small momentum transfer.[5-9, 25, 26] Accordingly fits were made to these data (Table 4) for a model with the complex spin independent scattering amplitude

$$f_n = f_o \; [\rho(t) e^{-Ar|t|/2} + ie^{-Ai|t|/2}], \tag{49}$$

where

$f_o = .2253 \; \sigma_T$

from the optical theorem. To obtain a simple two parameter form it is assumed that $A_r = A_i = A$ and that the parameter ρ, which represents the ratio of the real to the imaginary scattering amplitude, is independent of the four momentum transfer t. The value of ρ is particularly sensitive to the total cross section and the absolute normalization of the differential cross section.

From the fits to these data $[.0108 \leq |t| \leq .32 \; (\mathrm{BeV/c})^2]$ it can be shown that the average contribution of f_c is small, as expressed by

$$< | f_n + f_c | \; / \; |f_n| > \cong 1.02. \tag{50}$$

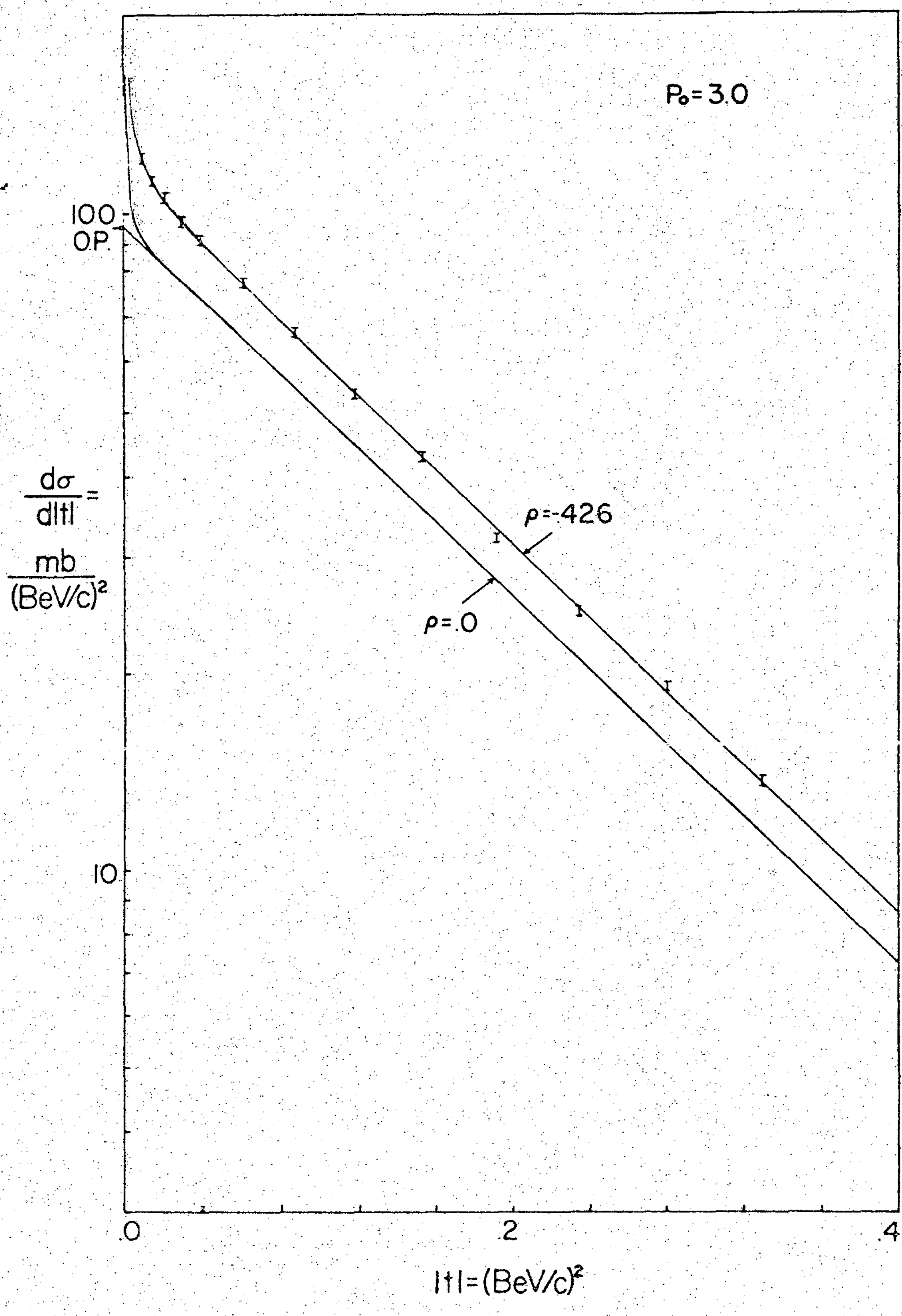

MU-36808

Fig. 18a. The forward scattering data taken with the hydrogen gas target at incident momentum $P_0 = 3.0$ BeV/c. The upper curve is the theoretical fit to the data points for $\rho = -.426$. The lower curve is shown for comparison with $\rho = 0$.

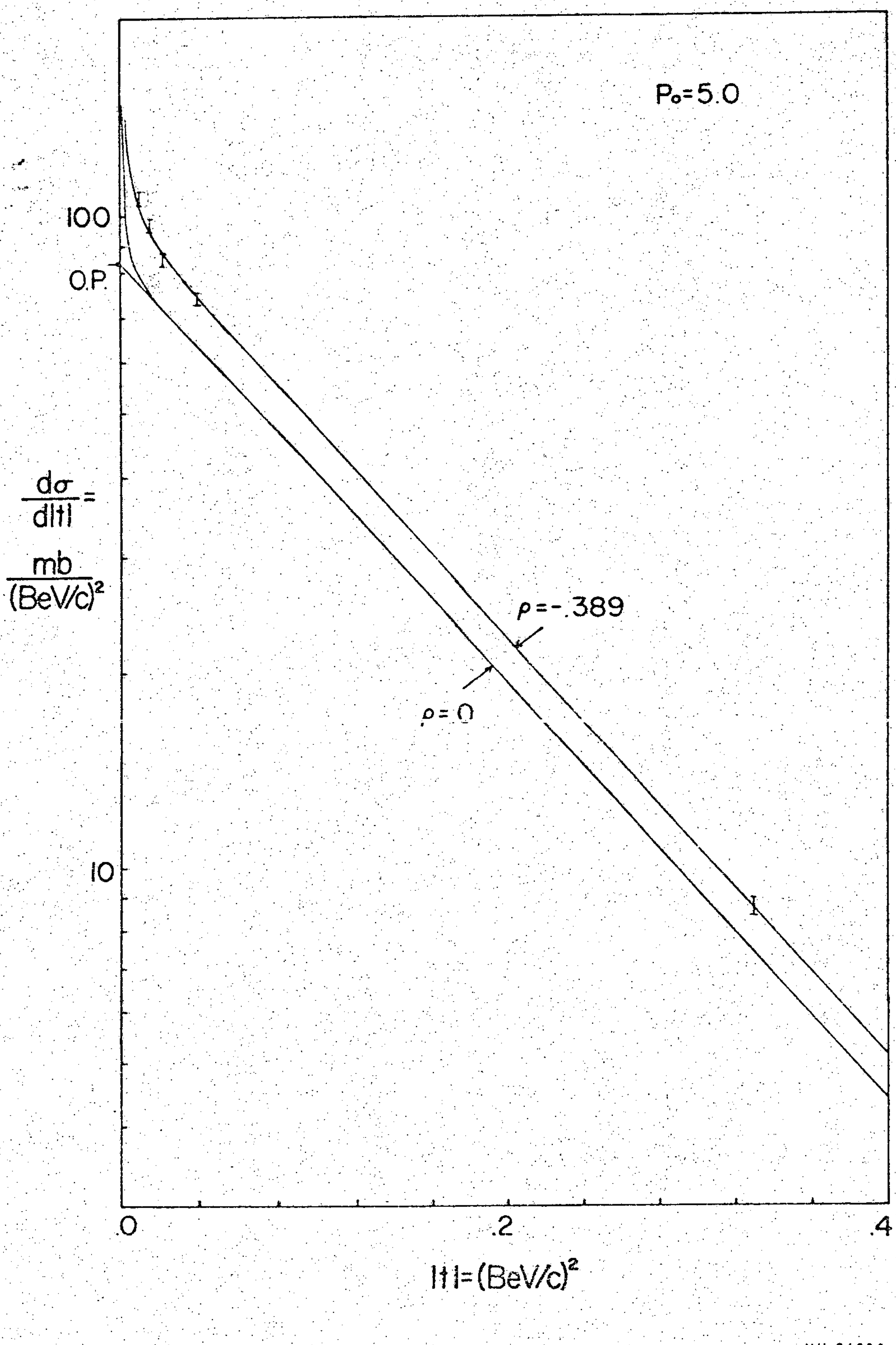

Fig. 18b. The forward scattering data taken with the hydrogen gas target at incident momentum P_o = 5.0 BeV/c. The upper curve is the theoretical fit to the data points for ρ = −.389. The lower curve is shown for comparison with ρ = 0.

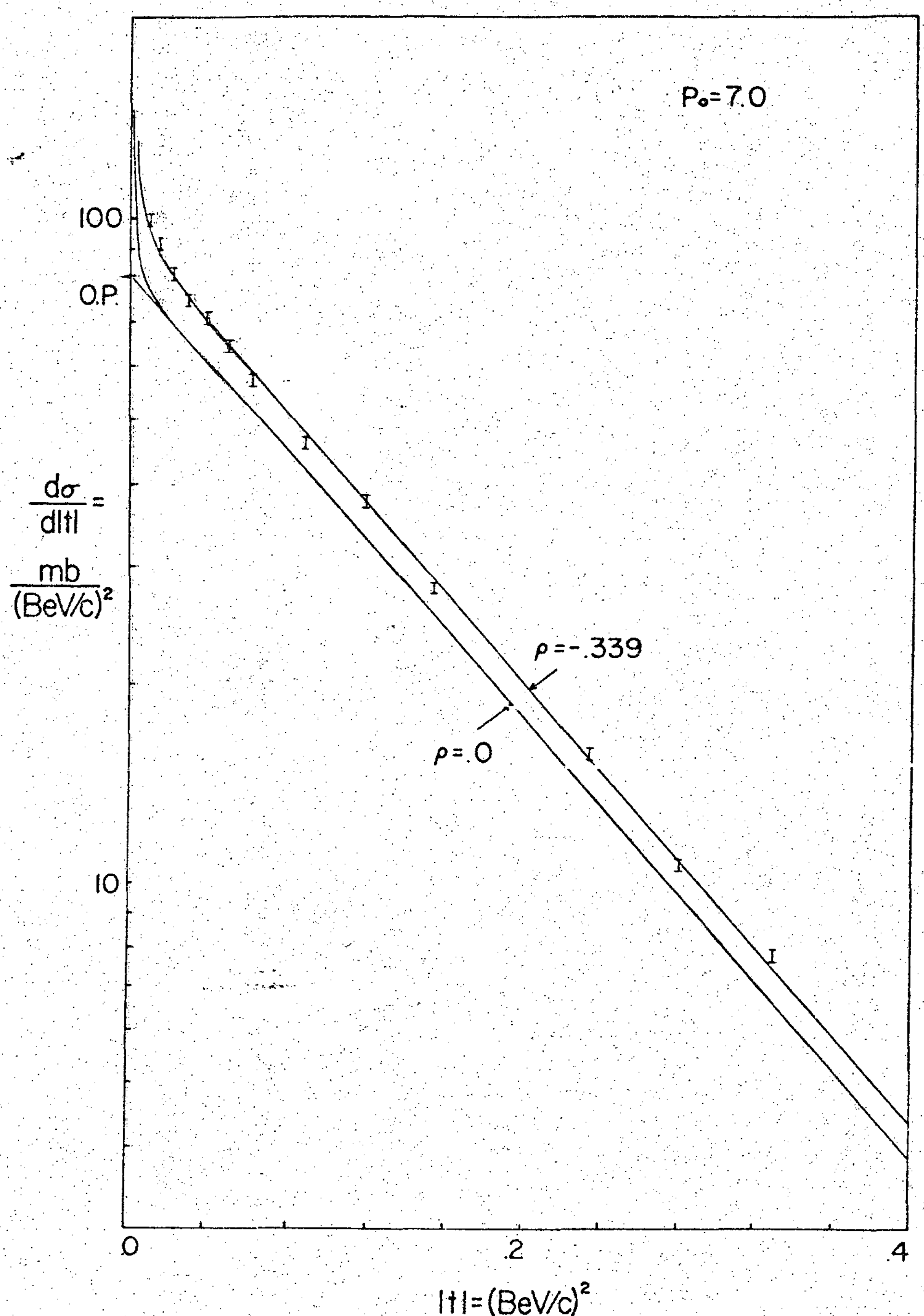

Fig. 18c. The forward scattering data taken with the hydrogen gas target at incident momentum P_o = 7.0 BeV/c. The upper curve is the theoretical fit to the data points for ρ = −.339. The lower curve is shown for comparison with ρ = 0.

Differentiating Eq. 47, one obtains

$$\Delta(d\sigma/d|t|) = 2\ |f_n + f_c| \cdot \Delta\ |f_n| \tag{51}$$

or

$$\frac{\Delta(d\sigma/d|t|)}{(d\sigma/d|t|)}\quad 2 \cdot\ \Delta|f_n|\ /\ |f_n + f_c| \cong 2\,\frac{\Delta|f_n|}{|f_n|}\ . \tag{52}$$

Using Eq. 49 this may now be written

$$(\Delta\ \sigma_T/\sigma_T)\Big|_N \cong \frac{1}{2}\ \cdot \Delta\ (d\sigma/d|t|)\ /\ (d\sigma/d|t|), \tag{53}$$

which to a good approximation is the effective error in σ_T from the uncertainty in normalization of $d\sigma/d|t|$. This normalization uncertainty is obtained from the calibration error given in Table I and a 1.7% overall systematic uncertainty. The significant contributions to this systematic error result from the combined uncertainties of the measured focal length and physical characteristics of the H_1 vertical bending magnet, and the measured geometry of the system. This affects, among other less significant parameters, the determination of ΔP_2 and $\Delta\phi$.

The values of σ_T are taken from the recent experiment of R. F. George, K. F. Riley, R. J. Tapper, D. V. Bugg, D. C. Satter, and G. H. Stafford with an error $(\Delta\sigma_T/\sigma_T)\big|_S$ of .31%.[22] Therefore, the effective, combined uncertainty is

$$\frac{\Delta\ \sigma_T}{\sigma_T} = \left[\left(\frac{\Delta\ \sigma_T}{\sigma_T}\Bigg|_S\right)^2 + \left(\frac{\Delta\ \sigma_T}{\sigma_T}\Bigg|_N\right)^2\right]^{1/2} \tag{54}$$

(numbers from the evaluation of this expression are quoted with σ_T in Table 5).

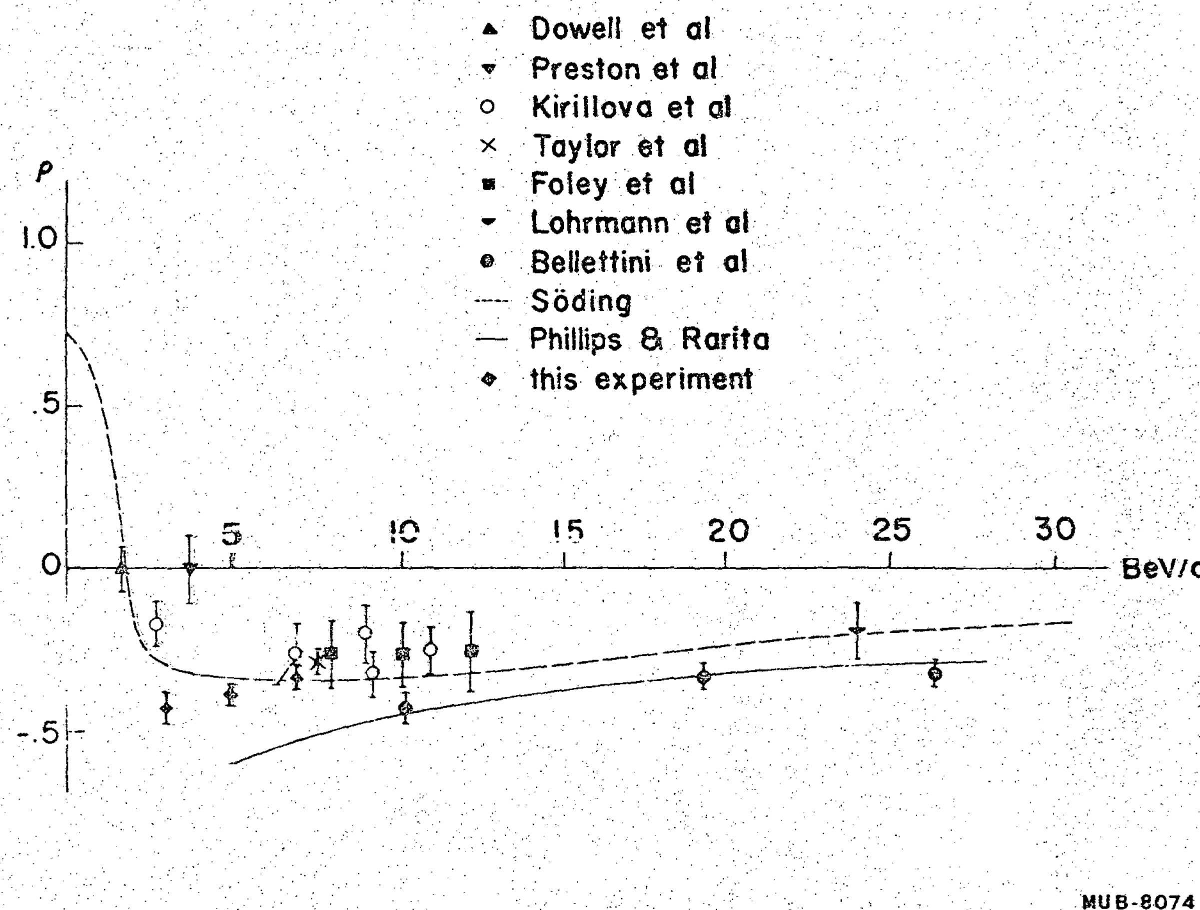

Fig. 19. Values of ρ taken from recent experiments (see References 5–9, 25, 26). The 3 values of this experiment are also shown. The two theoretical curves are from the work of P. Söding;[10] and R. J. N. Phillips and W. Rarita.[11]

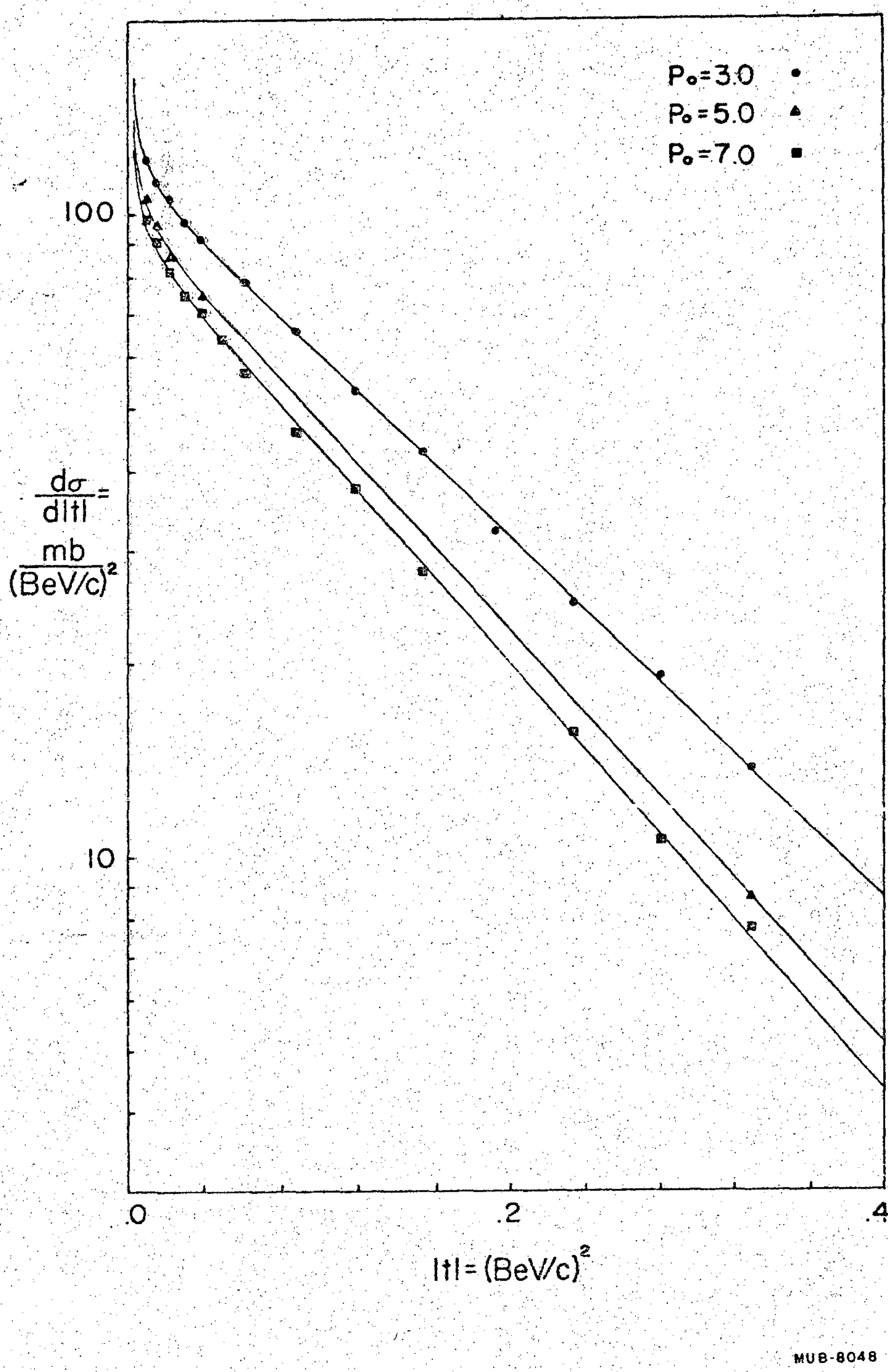

Fig. 20. The forward scattering data for the incident momenta P_0 = 3.0, 5.0, and 7.0 BeV/c. The curves shown are the theoretical fits to the data.

The error in ρ is calculated by

$$\frac{\Delta\rho}{\rho} = \left[\left(\frac{\Delta\rho}{\rho}\bigg|_S\right)^2 + \left(\frac{\Delta\rho}{\rho}\bigg|_\sigma\right)^2\right]^{1/2} , \tag{55}$$

where $\Delta\rho|_S$ is given by the error matrix from the least squares fitting procedure and $\Delta\rho|_\sigma$ is obtained by fitting with a variation of one standard deviation in σ_T.

Similarly,

$$\frac{\Delta A}{A} = \left[\left(\frac{\Delta A}{A}\bigg|_S\right)^2 + \left(\frac{\Delta A}{A}\bigg|_\sigma\right)^2\right]^{1/2} . \tag{56}$$

The results of the calculations are given in Table 5. The values of the χ^2 indicate the good agreement of the model with the behavior of the forward scattering for the presence of a real spin-independent amplitude, 34 to 43% of the imaginary part over the range $3.0 \leq 7.0$. On the basis of the good χ^2 it is also apparent that the assumption of similar behavior of the real and imaginary amplitudes must be reasonable.

These data are shown in Figs. 18a, 18b, and 18c for the incident moment 3, 5, and 7 respectively with $d\sigma/d|t|$ in $mb/(BeV/c)^2$ as a function of four momentum transfer $|t|$ in $(BeV/c)^2$. These figures also show the the calculated fits to the data. In addition, a curve for $\rho = c_o = 0$ is shown on each graph for comparison.

From this experiment and from recent work done by a number of investigators (see References 5 to 11, 25, 26) the absolute value of the real part appears to decrease with increasing energy. These data are shown in Fig. 19, along with two recent theorical curves. The upper curve is obtained from a dispersion relation calculation by P. Söding.[10] The lower curve is from the work of R. J. N. Phillips and W. Rarita using a four-pole Regge model.[11]

The forward scattering data from the gas target are shown plotted together in Fig. 20. These data show clearly the shrinkage of the diffraction peak with increasing energy. This was predicted by a number of Regge models.[2,3,4,11] However, there is no reason to expect the description to be as simple as the original one vacuum pole model.[2,3,4]

The total elastic cross sections were calculated by integrating the differential elastic scattering cross sections,

$$\sigma_e = \int_{o}^{2q^2} [d\sigma/d|t|]\, d|t| \tag{57a}$$

where q is the center-of-mass momentum. This integral was computed in two separate parts with

$$\sigma_e = \sigma_\epsilon^{(1)} + \sigma_e^{(2)} \tag{57b}$$

for

$$\sigma_e^{(1)} = \int_o^{.5} |f_n|^2\, d|t| \tag{57c}$$

and

$$\sigma_e^{(2)} = \int_{.5}^{2q^2} |f_n|\, d|t| \tag{57d}$$

The integral of Eq. 57c was calculated from the small angle scattering parameterization of the data (see Eq. 49) for the fitted values of A and ρ giving

TABLE 6

P_o BeV/c	$\Delta\sigma_e\|_s$	$\Delta\sigma_e\|_\sigma$	$\sigma_e^{(1)}$ mb	$\sigma_e^{(2)}$ mb	σ_e Tot. elastic cross section mb
3	±.4%	±3.9%	16.83±3.9%	1.61±7.0%	18.44±3.9%
5	±.3%	±2.7%	12.96±2.7%	.74±5.7%	13.71±2.7%
7	±.3%	±2.8%	11.70±2.8%	.38±5.8%	12.08±2.8%

$$\int_{o}^{.5} |f_n| d|t| = (\rho^2 + 1)(f_o^2/A)(1 - e^{-A/2}) \Big|_{o}^{.5} \tag{58}$$

The integral of Eq. 57d for $.5 \leq |t| \leq 2q^2$ was calculated numerically from the data. The values of the total elastic cross sections are given in Table 6. The error was determined from

$$\Delta\sigma_e = \sqrt{(\Delta\sigma_e^{(1)})^2 + (\Delta\sigma_e^{(2)})^2} \tag{59}$$

where $\Delta\sigma_e^{(2)}$ is an upper limit uncertainty on the numerical integration and

$$\Delta\sigma_e^{(1)} = \sqrt{(\Delta\sigma_e|_s)^2 + (\Delta\sigma_e|_\sigma)^2} \tag{60}$$

with $\Delta\sigma_e|_\sigma$ the error resulting from $\Delta\sigma_t$ of Eq. 54, or equivalently, f_o in Eq. 58, and

$$\Delta\sigma_e|_s = \left\{\left[(\delta\sigma_e^{(1)}/\delta A)\,\Delta A\,|_s\right]^2 + \left[(\delta\sigma_e^{(1)}/\delta\rho)\,\Delta\rho\,|_s\right]^2\right\}^{1/2} \tag{61}$$

for

$$\delta\sigma_e^{(1)}/\delta A = (\rho^2 + 1)\,(f_o^{\,2}/2A^2)\,[Ae^{-A/2} - 2\,(1 - e^{-A/2})] \tag{62}$$

and

$$\delta\sigma^{(1)}/\delta\rho = 2\,\rho\,f_o^{\,2}\,(1 - e^{-A/2})/A\,. \tag{63}$$

The data taken at large momentum transfer are given in Table 7 where the Lorentz invarient differential cross section $d\sigma/d|t|$ is given as a function of the four momentum transfer $|t|$. The error given is the combined counting statistics and the experimental uncertainty on each point. The counting statistics range from about ±.2 to ±4.0%, increasing roughly with $|t|$, where few points have statistical errors greater than ±1.0%.

For the Crossover Mode, the error arising from the systematics of the experiment is the combined result of a ±1.5% uncertainty in the data from magnet tuning and stability, in addition to a ±40% uncertainty in the inelastic background correction (0. to ±3.2% uncertainty in the data.). These corrections are discussed in detail in the analysis section "Crossover Mode".

The experimental error in the Parallel Mode results from the combination of a ±1.5% uncertainty in the data from magnet tuning and stability; a ±1.3 to ±3.5% uncertainty in the data from the correction for inelastic background; a ±1.5% uncertainty in the data from the anti-coincidence aperture correction; and a ±.5% uncertainty in the the data from the correction for aperture stopping in the system. These corrections are discussed in detail in the analysis section "Parallel Mode".

The data obtained at 90° in the center-of-mass system had an experimental error of ±.5% from the uncertainty in the inelastic background correction, in addition to an uncertainty of ±5.% resulting from the anti-coincidence aperture. These data are given in Table 8.

In addition to the calibration uncertainty quoted in Table 1, a systematic error of ±1.5% must be included to obtain the normalization error of the HMC. This error results from uncertainties in the measured geometry of the system and the emperically determined properties of the

Table 7

P_o BeV/c	$\|t\|$ $(BeV/c)^2$	$d\sigma/d\|t\|$ $mb/(BeV/c)^2$	Error %
3.0	1.039	.786	2.6
	1.172	.703	2.6
	1.363	.587	2.6
	1.487	.552	1.5
	1.559	.544	1.9
	1.760	.478	2.6
	1.965	.471	1.9
	2.068	.449	2.6
5.0	.2344	18.9	1.6
	.2433	17.0	1.7
	.3292	8.00	1.6
	.3497	6.91	1.7
	.3920	5.34	1.7
	.4360	4.09	1.7
	.4817	3.25	1.7
	.5289	2.47	1.8
	.5531	2.18	1.6
	.5776	1.89	1.8
	.6532	1.32	2.2
	.7316	.909	2.0
	.8125	.650	1.0
	.8957	.499	2.1
	1.010	.348	1.4
	1.098	.283	1.4
	1.248	.194	2.2
	1.402	.138	1.7
	1.559	.100	2.4
	1.883	.0617	2.4
	2.385	.0314	1.7
	3.250	.0195	6.0
	3.648	.0148	6.2
	3.893	.0160	5.5
7.0	.2344	15.7	1.6
	.2802	10.9	1.6
	.3292	6.97	1.6
	.3812	4.77	1.6
	.4360	3.12	1.6
	.5170	1.99	1.7
	.5531	1.61	1.2
	.6277	1.01	1.2
	.6790	.772	1.2
	.7052	.665	2.9
	.7853	.411	1.5
	.8125	.366	1.7
	.8677	.254	2.2
	.9524	.187	1.8
	1.039	.126	2.7
	1.402	.0467	2.2
	1.639	.0255	4.3
	1.720	.0203	2.0
	1.883	.0165	2.7
	2.048	.0128	3.0
	2.132	.0124	4.5
	2.385	.00798	2.9
7.06	2.385	.00671	2.8
	2.814	.00465	5.5
	3.250	.00267	2.8
	3.692	.00180	2.2
	4.138	.00136	2.5
	4.587	.00107	3.8
	5.039	.000781	5.4

quadrupole and Sagane magnets. The combined systematic and calibration for the HMC are

$$3.8\% \text{ for } P_o = 3 \text{ Bev/c},$$

$$2.5\% \text{ for } P_o = 5 \text{ BeV/c},$$

$$2.6\% \text{ for } P_o = 7 \text{ BeV/c}.$$

The data given in Tables 4 and 7 are plotted by incident momenta in the Figures 21a, b, and c for P_o=3, 5, and 7 BeV/c respectively.

The 90° center-of-mass data of Table 8 are plotted in Fig. 22. At large angles the cross sections are nearly independent of $|t|$. The presence of strong energy dependence makes hard core scattering unlikely. The statistical model of Fast, Hegedorn, and Jones gives the simple form[12,29,30]

$$d\sigma/d|t| = (\sigma/2qE)e^{-3.27(E - 1.88)} \tag{64}$$

where

q = center-of-mass momentum in BeV/c,

σ = total cross section less the diffraction scattering in mb,

E = center-of-mass energy in BeV,

for p-p elastic scattering in the region of 90° in the center-of-mass system. Fig. 22 shows Eq. 64 as a solid curve in a comparison with the data. In view of the low energies and the simple assumptions the fit to these data seems rather good.

At highenergies (10 to 31 BeV), in the region of large angle scattering, where one is sufficiently removed from the diffraction peak, considerable success in parameterizing p-p elastic scattering has been attained by Orear.[28] This relation for the angular dependence of the cross section is a simple exponential function of the Lorentz invarient

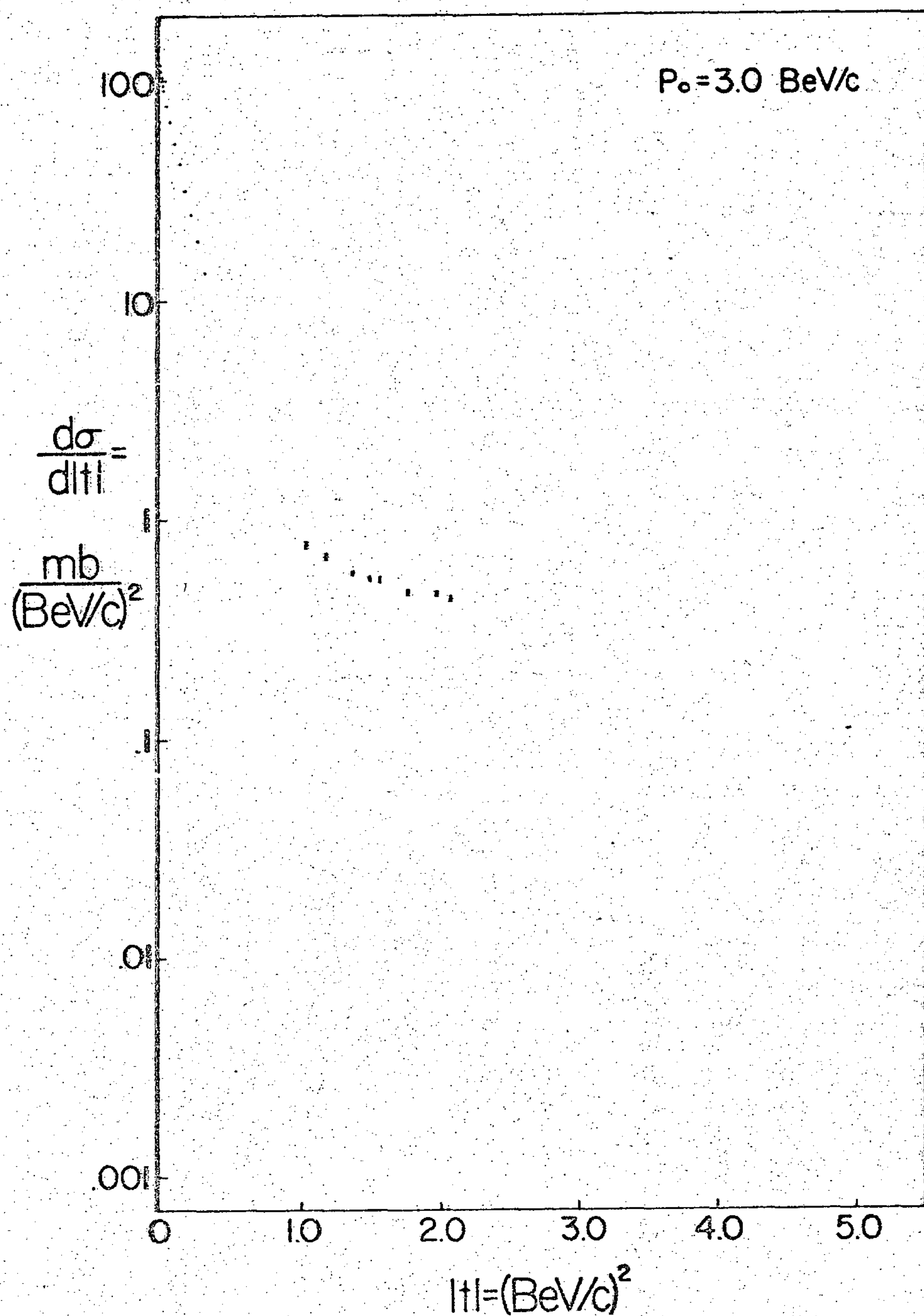

Fig. 21a. Data taken at P_o = 3 BeV/c plotted from Tables 4 and 7 giving $.01083 \leq |t| \leq 2.068$ $(BeV/c)^2$ where $|t| = 2.068$ corresponds to 90^o in the center-of-mass system.

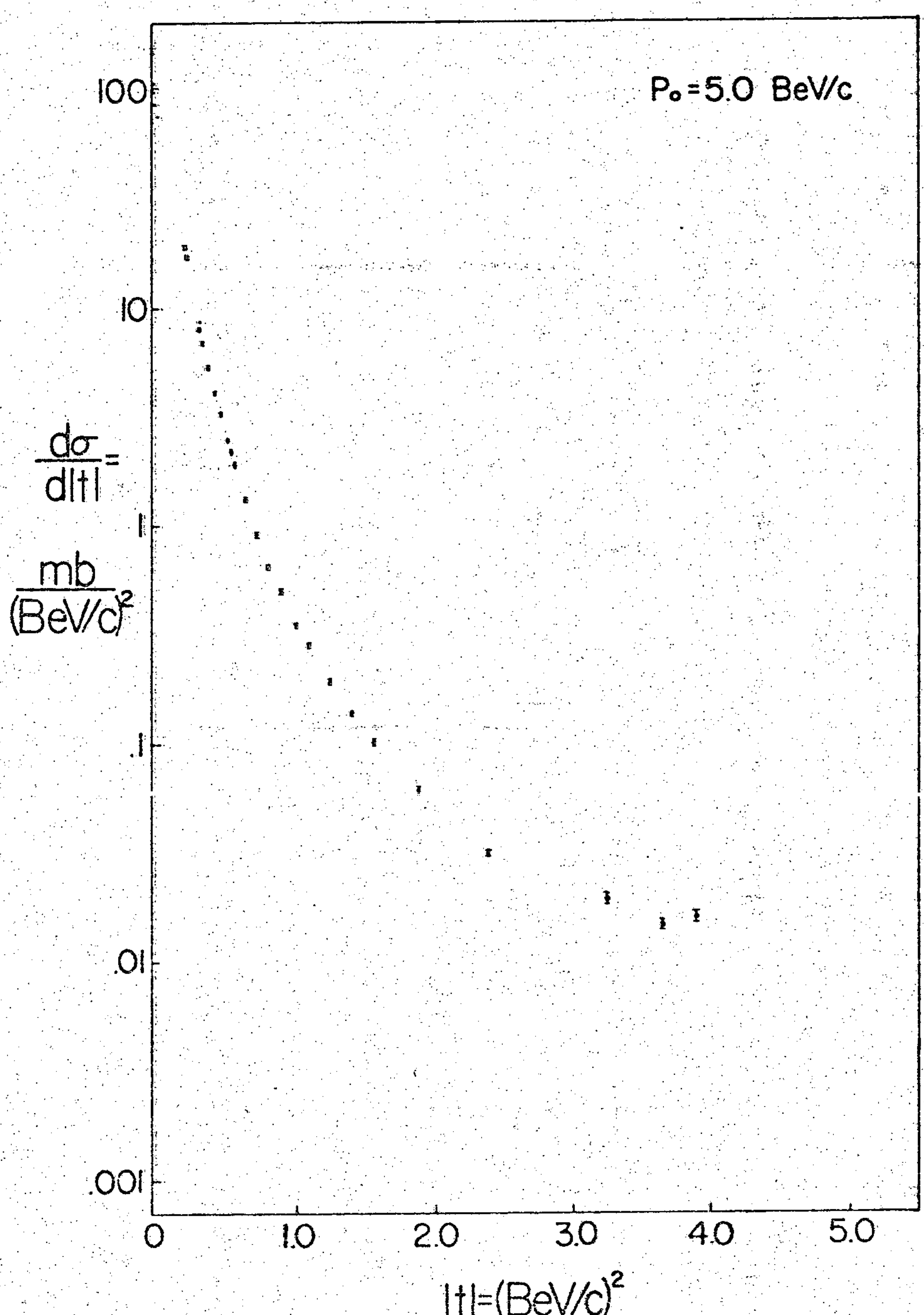

MUB-9936

Fig. 21b. Data taken at P_o = 5 BeV/c plotted from Tables 4 and 7 giving .01083 ≤ |t| ≤ 3.893 where |t| = 3.893 corresponds to 90° in the center-of-mass system.

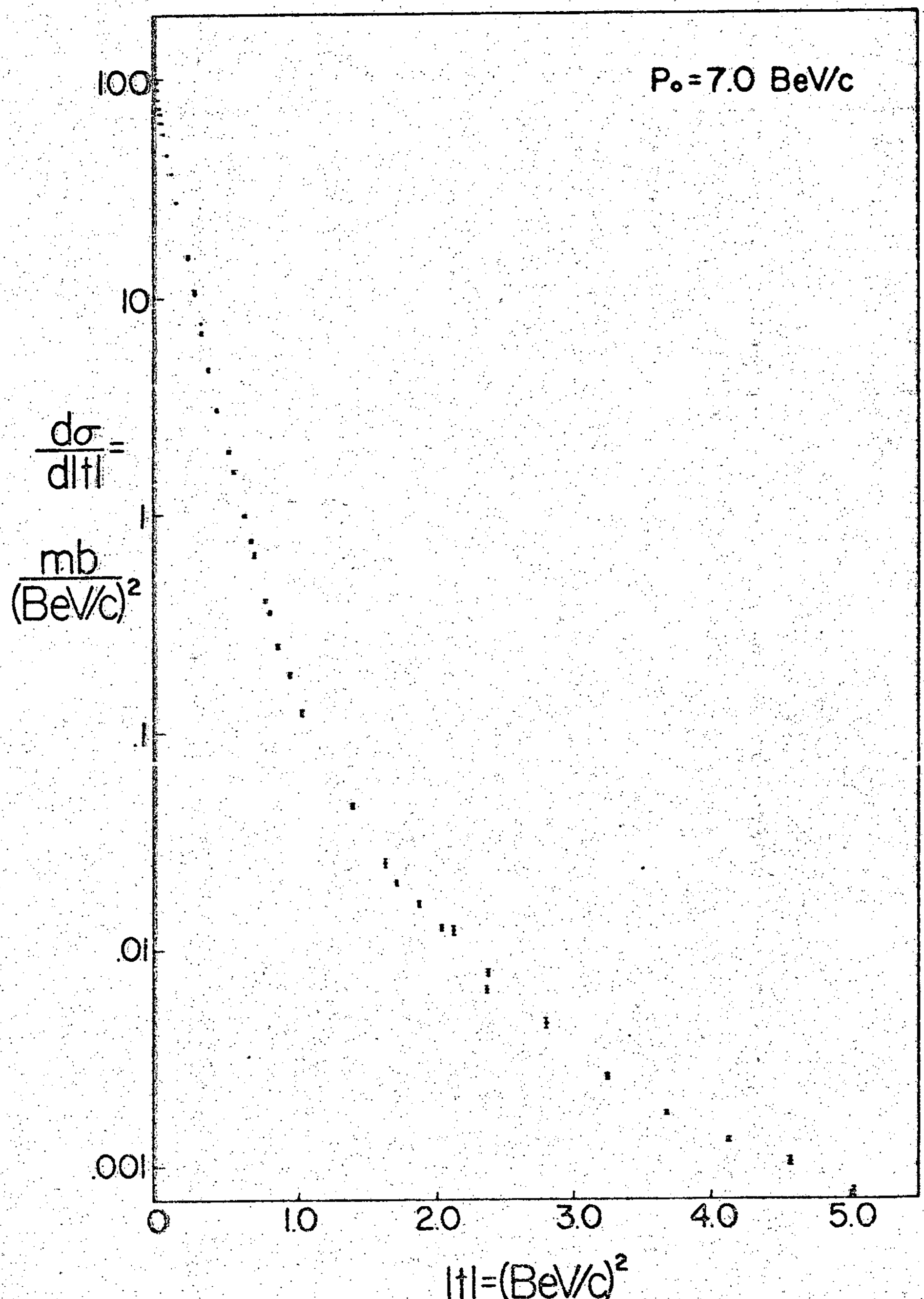

MUB-9935

Fig. 21c. Data taken at P_o = 7.056 BeV/c plotted from Tables 4 and 7 giving 2.385 ≤ |t| ≤ 5.039 $(Bev/c)^2$, in addition to data plotted from these Tables for P_o = 7.0 BeV/c giving .01083 ≤ |t| ≤ 2.385 $(BeV/c)^2$.

transverse momentum. An energy dependent gaussian term, which becomes significant in the region of the diffraction peak is also included by Orear to give

$$s\frac{d\sigma}{d\Omega_{cm}} = sBq^2 e^{-(cq\,\sin\theta_{cm})^2} + A\,e^{-aq\,\sin\theta_{cm}} , \qquad (65)$$

where

$A = 595 \pm 135$ BeV^2 mb/str,

$a = 6.33 \pm .12$ 1/(BeV/c),

s = the center-of-mass energy squared in (BeV)^2,

q = the center-of-mass momentum in BeV/c.

Comparison of Eq. 65 with the data taken in the experiment is graphically illustrated in Fig. 23, where these data have center-of-mass energies from 2.77 to 3.89 BeV. There is good qualitative agreement of these data with the model of Orear at all three energies (within 10 to 20%). For the data with the center-of-mass energy 3.89 BeV, in the range of $2.4 \leq |t| \leq 5.0$ (BeV/c)^2, the agreement is excellent giving the values

$A = 653.$ (BeV)^2,

$a = 6.4$ 1/(BeV/c),

for the normalization and slope of the exponential, respectively. The quantitative agreement for data at the center-of-mass energy 3.36 BeV is good over the range of $1.0 \leq |t| \leq 3.9$ (BeV/c)^2 where the slope of the exponential is 7./(BeV/c), and where these data, within the errors of this experiment, are significantly higher (10 to 17%) than Eq. 65. At 2.77 BeV in the center-of-mass, for $1.0 \leq |t| \leq 2.1$ (BeV/c)^2, these data are within 10% of Orear's model. However, the slope of the exponential is 4. /(BeV/c).

Table 8.

P_o BeV/c	$\|t\|$ $(\mathrm{Bev/c})^2$	$\frac{d\sigma}{dt}$ $\mathrm{mb/(BeV/c)^2}$	Error %
3.0	2.068	.449	2.6
3.2	2.248	.249	3.8
4.0	2.974	.0670	5.4
4.6	3.505	.0250	5.5
5.0	3.893	.0160	5.5
6.0	4.817	.00335	5.5

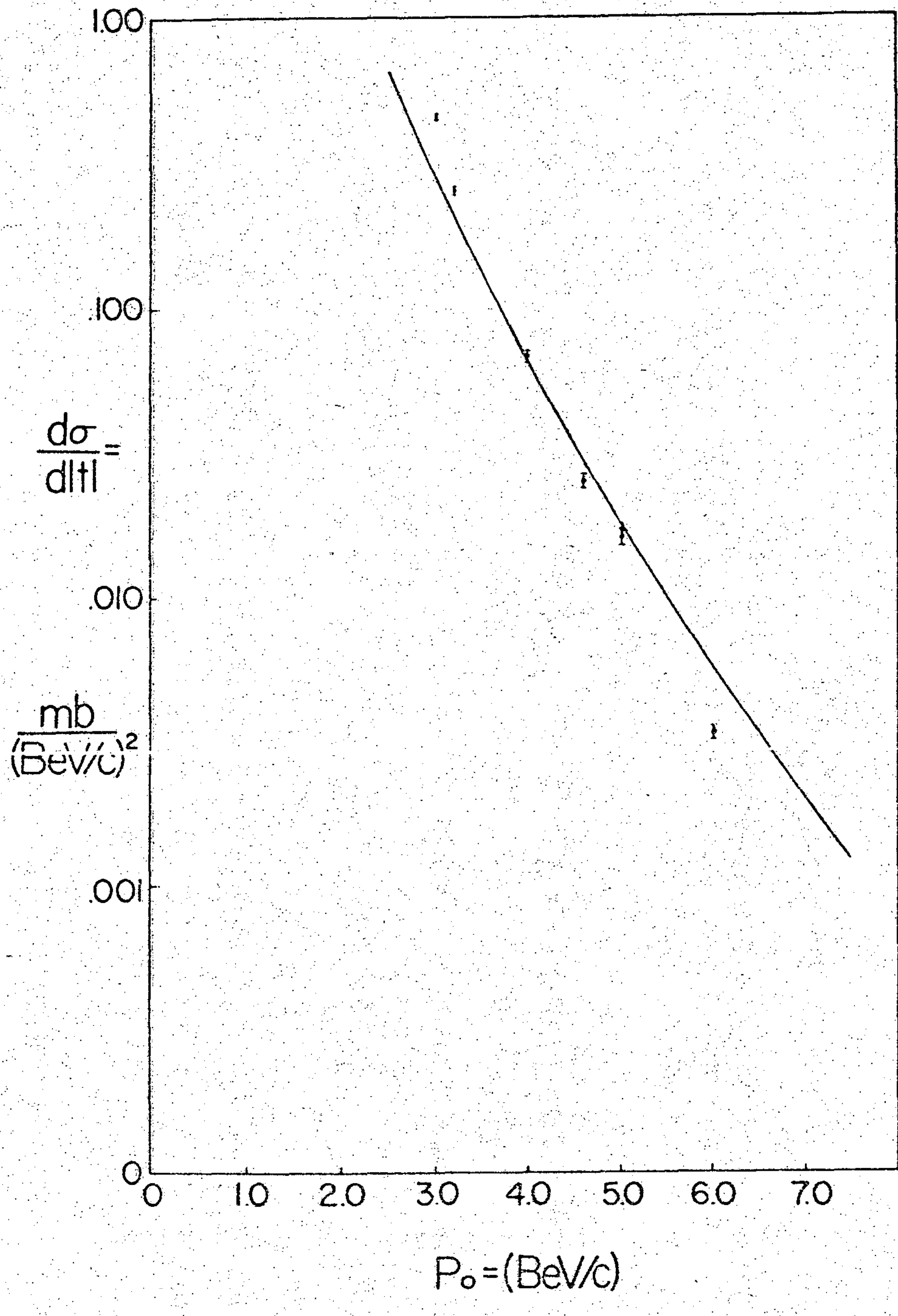

Fig. 22. Data taken at 90° in the center-of-mass system plotted from Table 8. The curve shown is the Fast, Hagedorn, Jones relation (see references 12,29,30).

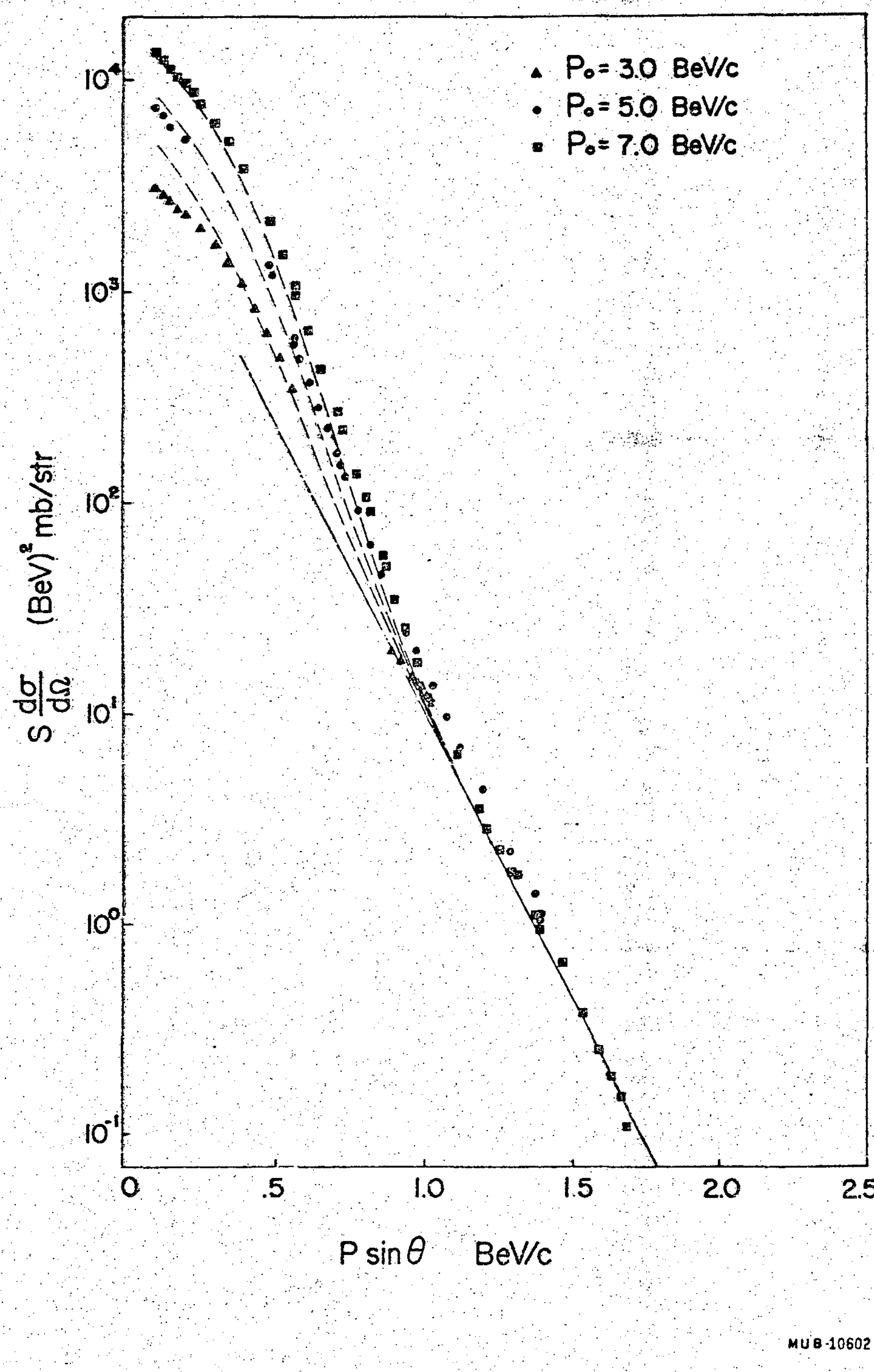

Fig. 23. Data at P_o = 3, 5, and 7 BeV/c plotted for comparison with the recent fit by Orear to p-p elastic scattering data at higher energies.(28) The solid line is the exponential term of the transverse momentum that dominates at large angles. The dotted lines include the gaussian term.

ACKNOWLEDGEMENT

I would like to acknowledge the assistance of my advisor, Leroy T. Kerth, and other members of the Lofgren Research Staff in the preparation of this thesis. Thanks are also due Roger W. Williams, a technician of the Lofgren Group, for dedicated work on the analysis of this experiment. In addition, I would like to express sincere appreciation to the secretarial staff for the typing of this paper.

APPENDIX A

DETERMINATION OF MASS RESOLUTION

Assuming $p + p \rightarrow p + x$, it can be shown from relativistic kinematics that

$$p_2^2 = \gamma_2^2 - 1 = \frac{m^2}{x^2}\left\{\left[(\gamma_o + 1) - \gamma_1\right]^2 - \frac{x^2}{m^2}\right\}, \qquad \text{(A-1)}$$

and

$$p_2^2 = \frac{m^2}{x^2}\left\{p_o^2 - 2\,p_o\,p_1\cos\theta_1 + p_1^2\right\}, \qquad \text{(A-2)}$$

where

$$p = P/m .$$

This leads to

$$p_o^2 - 2\,p_o\,p_1\cos\theta_1 + p_1^2 = (\gamma_o + 1)^2 - 2\,\gamma_1\,(\gamma_o + 1) + p_1^2 + 1 - \frac{x^2}{m^2},$$

and reduces to

$$\gamma_1 = p_1\,T + \delta$$

or

$$p_1^2\,(T^2 - 1) + p_1\,2T\delta + (\delta^2 - 1) = 0,$$

which gives

$$p_1 = \frac{T\,\delta + \sqrt{\delta^2 - (1 - T^2)}}{1 - T^2}, \qquad \text{(A-3)}$$

where

$$\beta_{cm} = \sqrt{\frac{\gamma_o - 1}{\gamma_o + 1}}$$

$$T = \beta_{cm}\cos\theta$$

$$\delta = 1 - \left[\left(\frac{x^2}{m^2} - 1\right)/(2\,\gamma_o + 2)\right],$$

and

$$\lim_{x \rightarrow m} p_1 = \frac{2T}{1 - T^2} \quad \text{or}$$

16

$$p_1 = 2\ \beta_{cm} \cos\theta./(1 - \beta_{cm}^2 \cos^2\theta_1)\ . \qquad \text{(A-4)}$$

Taking the derivative of Eq. (A-3)

$$\frac{dP_1}{dX} = \left(\frac{T^2+1}{T^2-1}\right)/\ T\ (\gamma_o + 1)\ . \qquad \text{(A-5)}$$

Therefore, if $\frac{\Delta P_1}{P_1}$ is the dispersion in the system, then

$$\frac{\Delta m}{m} = \frac{P_1}{m}\left[\frac{\Delta P_1}{P_1}\right]/\frac{dP_1}{dX}\ , \quad \text{or}$$

$$\Delta m/m = \left|(\gamma_o + 1)\ \beta_{cm} \cos\theta_1\ \frac{\Delta P_1}{m}\left[(1-\beta_{cm}^2 \cos^2\theta_1)/(1+\beta_{cm}^2 \cos^2\theta_1)\right]\right| \qquad \text{(A-7)}$$

is the mass resolution.

APENDIX B.

LOW MOMENTUM CHANNEL CALIBRATIONS AND ION CHAMBER DESCRIPTION

The remotely controlled brass collimator of the Low Momentum Channel was driven by stepping motors with separate controls and direct digital readout for both the throat gap and the azimuth. The azimuth readout was adjusted to give zero when the collimator was set at 69.5° to the EPB. This was the effective target position that allowed the scattered beam to travel directly down the LMC without need of horizontal deflection. The calibration for the azimuth is given by

$$\theta_B = A_1 - N_\theta A_2, \tag{B-1}$$

where N_θ is the readout number, and A_1 and A_2 are empirical constants. These have the values

$$A_1 = 69.5 \text{ (for } 50.0^\circ \leq \theta_B \leq 69.5^\circ\text{)},$$

$$A_1 = 327.8 \text{ (for } 69.5^\circ \leq \theta_B \leq 95.0^\circ\text{)},$$

and

$$A_2 = 1/385.55 \text{ (for } 50.0^\circ \leq \theta_B \leq 95.0^\circ\text{)}.$$

The calibration for the gap spacing is given by

$$G = (R_1 + R_2)(24.083\pi/180. + N_G/C) - 12.0, \tag{B-2}$$

where

$$R_1 = 14. + 22/32$$

$$R_2 = 14. + 23/32$$

$$C = (180/\pi)(320/360)(72/3.32)(2)(10) = 22{,}093.$$

$$N_G = \text{gap readout}$$

which gives the gap G in inches. The constants R_1 and R_2 are taken from the geometry of the brass collimator. The number C contains the dependence of the reading on the various gear ratios that coupled the remote system.

The temperature of the gas target was read by a thermistor located on the target container. Using a simple bridge circuit containing the thermistor, two 20 KΩ resistors, and a helipot, the temperature was read in ohms. The calibration of this device in centigrade degrees is given by a curve that was generated empirically. With this arrangement it was possible to determine the temperature of the target in Kelvin degrees to better than .5%.

The ionization chamber used in this experiment was designed by W. A. Wenzel. It consisted of 11 parallel aluminum foils .00025" in thickness. These were separated by 1/8" giving a beam path length of 1-1/4" in the sensitive region. The plates were enclosed in a container and operated at 1 atm pressure. The gas in the container consisted of 93% argon and 7% methane. Alternate plates were connected to a 200 volt D.C. source. The other plates were connected to an integrating electrometer, thus providing 10 sensitive gaps. With the electrometer attached to the inner 5 alternate plates it was possible to avoid collection of charges outside of the sensitive volume.

APPENDIX C

DETERMINATION OF ENERGY LOSS IN THE TARGETS

Let the path traversed in the target by the scattered beam be given by

$$\Delta R = R_1 - R_2 , \tag{C-1}$$

where R_1 is the range of the initial scattered momenta P_1 and R_2 is the range of the observed scattered momenta P_2. For a sufficiently small region of momenta the range-momentum curves of John H. Atkinson, Jr. and Beverly Hill Willis can be approximated by straight line segments on a log-log plot of the curve.[17] These have the form

$$\log P = \log b + n \log R, \tag{C-2}$$

where a sufficient number of these line segments are taken to approximate the range-momentum curve within the original reading errors. The constants b and n are then evaluated from the curve, being uniquely determined by requiring the line (C-2) to pass through ($\log P_{ai}$, $\log R_{ai}$) and ($\log P_{bi}$, $\log R_{bi}$), which are the end points of a typical line segment approximating the curve. This leads to a set of constants n_i and b_i that serve to define the range-momentum curve through equation (C-2) for momenta such that $P_{ai} \leq P_i \leq P_{bi}$.

Dropping the subscripts, one may re-write (C-2) in the form

$$P_1 = b\, R_1^{\,n} \tag{C-3a}$$

for the initial momenta, and

$$P_2 = b\, R_2^{\,n} \tag{C-3b}$$

for the observed momenta. These two relations may be inverted to give

$$\Delta R = R_1 - R_2 = \left(\frac{P_1}{b}\right)^{1/n} - \left(\frac{P_2}{b}\right)^{1/n} \quad . \tag{C-4}$$

Now this can be solved for P_1 or P_2 giving

$$P_1 = \mathrm{EXP}\left\{\log b + n \log \left[\Delta R + \mathrm{EXP}\left(\frac{1}{n} \log \frac{P_2}{b}\right)\right]\right\} \tag{C-5a}$$

and

$$P_2 = \mathrm{EXP}\left\{\log b + n \log \left[- \Delta R + \mathrm{EXP}\left(\frac{1}{n} \log \frac{P_1}{b}\right)\right]\right\} . \tag{C-5b}$$

From relativistic kinematics

$$\beta = P/E = P/(P^2 + M^2)^{1/2} \quad ,$$

or one may write

$$\frac{\beta_2}{\beta_1} = \frac{P_2}{P_1} \left[(P_1^2 + m^2)/(P_2^2 + m^2)\right]^{1/2} \tag{C-6}$$

for the ratios of the observed to the initial velocity of the scattered beam particles. By differentiating (C-3a) and (C-3b) with respect to R one obtains

$$\Delta R = \Delta P_1 \left(\frac{P_1}{b}\right)^{(1-n)/n} = \Delta P_2 \left(\frac{P_2}{b}\right)^{(1-n)/n} \tag{C-7}$$

or

$$\frac{\Delta P_2}{\Delta P_1} = \left(\frac{P_1}{P_2}\right)^{(1-n)/n} = \mathrm{EXP}\left[\frac{(1-n)}{n} \log \frac{P_1}{P_2}\right] . \tag{C-8}$$

The composite energy loss correction to the cross-section is then just the product of the equations (C-6) and (C-8) which gives

$$\frac{\beta_2\ \Delta P_2}{\beta_1\ \Delta P_1} = \mathrm{EXP}\left\{ \frac{1}{2} \log \left[(P_1^2 + m^2)/(P_2^2 + m^2) \right] + \frac{(1-2n)}{n} \log \frac{P_1}{P_2} \right\}. \tag{C-9}$$

APPENDIX D

MATRIX REPRESENTATION OF THE BEAM OPTICS

It is convenient to describe a magneto—optical system by a matrix representation of each element. In the absence of a mass spectrometer, a 5 x 5 matrix is sufficient for the description, where the vector space is given by

$$X = \begin{pmatrix} x \\ x' \\ y \\ y' \\ \Delta P/P \end{pmatrix} ,$$

where x is measured positive to the left when looking downstream and y is measured in the vertical direction in a plane perpendicular to the optic axis. Also

$$x' = dx/dz$$

$$y' = dy/dz$$

where z is the optic axis and is measured in the direction of the beam.

If X_d is a vector at the detector plane and X_s a vector taken at the source, then they are related by

$$X_d = Q_T X_s \tag{D-1}$$

where Q_T is the product matrix of the system, that is

$$Q_T = \prod_i^N Q_i \, . \tag{D-2}$$

The Q_i are some combination of the elements that make up the configuration desired. The various matrices for the beam elements are labeled:

$Q_f = \{f_{ij}\}$ for the field free regions;

$Q_q = \{q_{ij}\}$ for the quadrupole elements;

$Q_b = \{b_{ij}\}$ for the bending magnets;

$Q_s = \{s_{ij}\}$ for the horizontal bending elements with the circular pole forces.

The matrices for the field free region, the quadrupole, and the bending magnet are adapted from the work of Thomas J. Devlin.[18] Thus, for Q_f one may write

$$f_{11} = 1 \tag{D-3a}$$

$$f_{12} = \ell_f \tag{D-3b}$$

$$f_{22} = 1 \tag{D-3c}$$

$$f_{33} = 1 \tag{D-3d}$$

$$f_{34} = \ell_f \tag{D-3e}$$

$$f_{44} = 1 \tag{D-3f}$$

$$f_{55} = 1 \tag{D-3g}$$

(all other matrix elements = 0), where ℓ_f is the length of the field free region (to first order in x', y').[15]

The quadrupole matrix Q_q has the form

$$q_{11} = \cos\theta \tag{D-4a}$$

$$q_{12} = \ell_q \sin\theta/\theta \tag{D-4b}$$

$$q_{21} = -\theta \sin\theta/\ell_q \tag{D-4c}$$

$$q_{22} = \cos\theta \tag{D-4d}$$

— — — continued on next page

$$q_{33} = \cosh\theta \tag{D-4e}$$

$$q_{34} = \ell_q \sinh\theta/\theta \tag{D-4f}$$

$$q_{43} = \theta \sinh\theta/\ell_q \tag{D-4g}$$

$$q_{44} = \cosh\theta \text{ (all other q's = 0)} \tag{D-4h}$$

for a converging focusing condition in the horizontal plane. For a diverging lens in the horizontal, the two independent 2 x 2 matrices for the x and y planes simply replace each other. The parameter ℓ_q is defined as the effective length of the field and

$$\theta^2 = \ell_q^2 \frac{dB}{dr} / (1313.2\ P_1)$$

with

$$\frac{dB}{dr} = \text{the field gradient in the magnet}$$

and

$$P_1 = \text{the scattered beam momentum in MeV/c} .$$

The matrix Q_b for a magnetic spectrometer oriented to give a downward deflection is adapted to first order in ΔX from the equations given by W. G. Cross,[16] where

$$b_{11} = 1 - \Phi_v \tan\epsilon \tag{D-5a}$$

$$b_{12} = \rho\, \Phi_v \tag{D-5b}$$

$$b_{21} = (\Phi_v \tan^2\epsilon - 2\tan\epsilon)/\rho \tag{D-5c}$$

$$b_{22} = 1 - \Phi_v \tan\epsilon \tag{D-5d}$$

$$b_{33} = \cos(\Phi_v - \epsilon)\cos\epsilon \tag{D-5e}$$

$$b_{34} = \rho \sin\Phi_v \tag{D-5f}$$

$$b_{35} = \rho\,(1 - \cos\Phi_v) \tag{D-5g}$$

$$b_{43} = -\sin(\Phi_v - 2\epsilon)/(\rho\cos^2\epsilon) \tag{D-5h}$$

$$b_{44} = \cos(\Phi_v - \epsilon)/\cos\epsilon \tag{D-5i}$$

— — — continued on next page

$$b_{45} = 2 \sin (\Phi_v/2) \cos (\epsilon - \Phi_v/2)/\cos \epsilon \quad \text{(D-5j)}$$

$$b_{55} = 1 \quad \text{(all other matrix elements = 0)}, \quad \text{(D-5k)}$$

where

$$\rho = \ell_{eff}/(2 \sin \Phi_v)$$

and

$$\ell_{eff} = \text{the effective length of the pole face.}$$

In these matrix elements ϵ is the wedge angle. This is the angle between the optic axis and the normal to the entrance or exit pole face of the magnet. In general the entrance and exit wedge angles are different. However, in the case where the bending magnet is oriented symmetrically about the turning point, they are the same. For pole faces that have an effective rectangular shape, the wedge angle is just 1/2 the angle of deflection, or

$$\epsilon = \Phi_v/2$$

The bending magnet matrix in this case reduces to

$$b_{11} = 1-\Phi_v \tan (\Phi_v/2) \quad \text{(D-6a)}$$

$$b_{12} = \rho \cdot \Phi_v \quad \text{(D-6b)}$$

$$b_{21} = [\Phi_v \tan^2 (\Phi_v/2) - 2 \tan (\Phi_v/2)]/\rho \quad \text{(D-6c)}$$

$$b_{22} = 1 - \Phi_v \tan (\Phi_v/2) \quad \text{(D-6d)}$$

$$b_{33} = 1 \quad \text{(D-6e)}$$

$$b_{34} = \rho \sin \Phi_v \quad \text{(D-6f)}$$

$$b_{35} = \rho (1 - \cos \Phi_v) \quad \text{(D-6g)}$$

$$b_{43} = 0 \quad \text{(D-6h)}$$

$$b_{44} = 1 \quad \text{(D-6i)}$$

$$b_{45} = 2 \tan (\Phi_v/2) \quad \text{(D-6j)}$$

$$b_{55} = 1 \quad \text{(all other matrix elements = 0)}. \quad \text{(D-6h)}$$

For the derivation of a matrix representation of a deflection magnet with cylindrical pole faces it is useful to define the following parameters indicated in Fig. D-1.

R_e = the effective radius of the pole tip,

ℓ_a = the distance from the center of the pole tip to the aperture,

ℓ_t = the distance from the center of the pole tip to the target,

Φ_h = the horizontal deflection angle of the scattered beam,

$x'_o = dx_c/dz$,

$x' = dx/dz$,

$\rho' = \rho + \Delta\rho$.

If one considers initial vectors such that

$$X_o = (x_o,\ x'_o,\ y_o,\ y'_o,\ \Delta p_1/p_1) \ll 1 ,$$

then the entire field including the fringe region can be considered uniform with no vertical focusing to a very good approximation in first order. In a uniform field the proportionality of ρ and p_1 may be expressed by

$$\Delta\rho = \rho\ \Delta p_1/p_1 . \tag{D-7}$$

It is also useful to relate ρ, R, and Φ. From Fig. D-1

$$\rho = R \cot \Phi/2 . \tag{D-8}$$

The slope x' of the orbit after leaving the field is determined by three independent effects. This may be written

$$\Delta X' = \Delta X'_o + \Delta\Phi|_{\Delta p} + \Delta\Phi|_{\Delta s} , \tag{D-9}$$

where $\Delta\Phi|_{\Delta p}$ relates to the change in ρ and hence of Φ as a function of variations Δp in p. The term $\Delta\Phi|_{\Delta s}$ relates to the change in Φ determined by x'_o and x_o. This is more conveniently treated as just one factor

$$s = x'_o(\ell_t + x_o/x'_o) = (x'_o\ \ell_t + x_o) . \tag{D-10}$$

The dependence of x' on $\Delta\Phi|_{\Delta p}$ may be obtained directly from Eq. (D-8) by

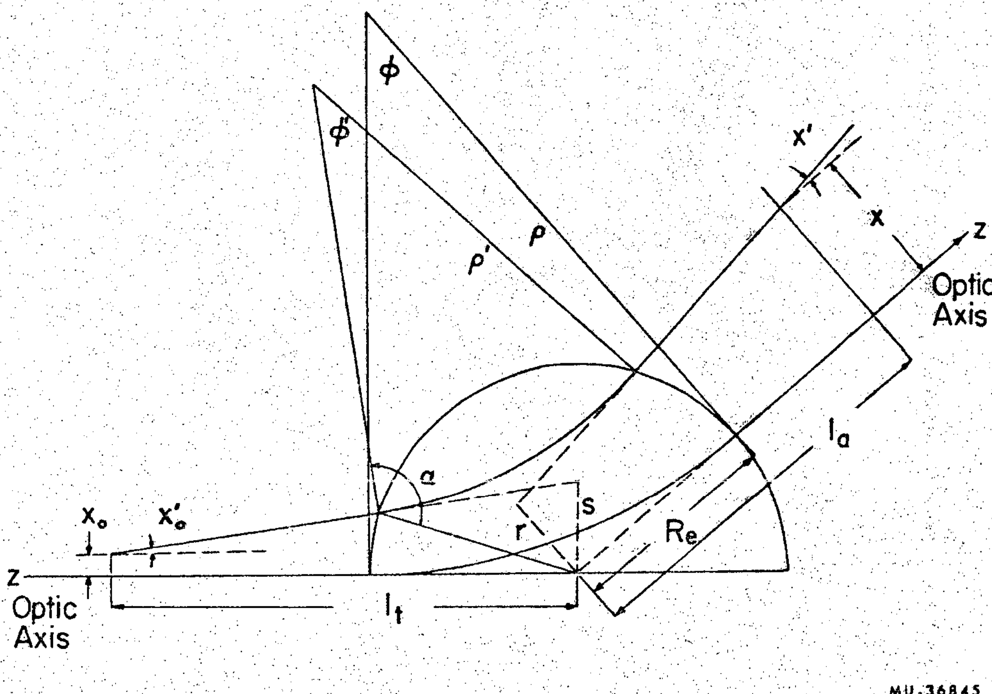

Fig. D-1. The definition of the various parameters used in the derivation of the matrix representation of a cylindrical magnet are illustrated for a typical orbit. R_e is the effective radius of the field; ℓ_t and ℓ_a are the distances from the center of the pole faces to the target and aperture respectively. The angle of deflection is given by ϕ.

differentiating with respect to Φ which gives

$$\Delta\rho = -R \csc^2 (\Phi/2)(\Delta\Phi/2) , \tag{D-11}$$

or by substituting Eqs. (D-7) and (D-8)

$$R(\Delta p/p) \cot (\Phi/2) = -R(\Delta\Phi/2)/\sin^2 (\Phi/2) . \tag{D-12}$$

This reduces to

$$\Delta\Phi\big|_{\Delta p} = -(\Delta p/p) \sin \Phi . \tag{D-13}$$

For the dependence of x' on $\Delta\Phi\big|_{\Delta s}$ one may write from geometry

$$R_e/x_o' = -T/\cos \alpha$$

for

$$T = (\ell_t + x_o/x_o') .$$

This reduces to

$$\cos \alpha = -s/R_e . \tag{D-14}$$

Also, from the geometry

$$\cos (\Phi'/2) = \left\{\rho^2 + R_e^2 - 2\rho R_e \cos \alpha + \rho^2 - R_e^2\right\} / \left\{2\rho(\rho^2 + R_e^2 - 2\rho R_e \cos \alpha)\right\}^{1/2} \tag{D-15}$$

Substituting Eq. (D-14), this reduces to

$$\cos (\Phi'/2 = (\rho + s) / (R^2 + \rho^2 + 2\rho s)^{1/2} . \tag{D-16}$$

By differentiating Φ' with respect to s with ρ held constant one attains

$$-\left[2 \sin (\Phi'/2) \cos (\Phi'/2)\right]\left[\Delta\Phi'/2\right]\left[R_e^2 + \rho^2 + 2\rho s\right]$$
$$+ 2 \rho\Delta s \cos^2 (\Phi'/2) = 2 \rho\Delta s + 2 s\Delta s \tag{D-17}$$

Now by evaluating this expression at $x_o' = x_o = 0$ and substituting Eq. (D-8)

$$-\Delta\Phi R_e^2 \sin (\Phi/2) \cos (\Phi/2) \left[1 + \cot^2 (\Phi/2)\right]$$
$$= 2 R_e \Delta s \cot (\Phi/2) \left[1 - \cos^2 (\Phi/2)\right],$$

or

$$\Delta\Phi\big|_{\Delta s} = -2\Delta s \sin^2 (\Phi/2) / R_e \tag{D-18}$$

where

$$\Delta s = \ell_t \Delta x_o' + \Delta x_o .$$

Therefore, by substituting eqs. (D-13) and (D-18) into eq. (D-9) one obtains

$$\Delta X' = \Delta x_o[-2 \sin^2(\Phi/2)/R_e] + \Delta x_o^1[1 - 2\ell_t \sin^2(\Phi/2)/R_e]$$
$$+ (\Delta p/p)[- \sin\Phi] \qquad \text{(D-19)}$$

The displacement of an orbit from the optic axis in the x,z plane at the aperture is given by

$$\Delta X = \Delta x_o'T + \Delta x' \ell_a. \qquad \text{(D-20)}$$

Using eq. (D-19) this may be written

$$\Delta X = \Delta x_o[1 - 2\ell_a \sin^2(\Phi/2)/ R_e]$$
$$+ \Delta x_o'[\ell_t + \ell_a - 2\ell_a\ell_t \sin^2(\Phi/2)/R_e]$$
$$+ (\Delta p/p)[-\ell_a \sin\Phi] \qquad \text{(D-21)}$$

The length of the optic axis from the target to the aperture is obtained directly from the geometry giving

$$L = \ell_t + \ell_a - 2R_e + R_e\Phi \cot (\Phi/2). \qquad \text{(D-22)}$$

Therefore

$$\Delta y = \Delta y_o + \Delta y_o' [\ell_t + \ell_a - 2R_e + R_e\Phi \cot (\Phi/2)], \qquad \text{(D-23)}$$

also

$$\Delta y' = \Delta y_o' \qquad \text{(D-24)}$$

It is now possible from the eqs. (D-19), (D-21), (D-23), (D-24) to write down the 5 x 5 matrix representation of this magnet:

$$S_{11} = 1 - 2 \ell_a \sin^2 (\Phi_h/2)/R_e \qquad \text{(D-25a)}$$
$$S_{12} = \ell_t + \ell_a - 2 \ell_a \ell_t \sin^2 (\Phi_h/2)/R_e \qquad \text{(D-25b)}$$
$$S_{15} = -\ell_a \sin \Phi_h \qquad \text{(D-25c)}$$
$$S_{21} = -2 \sin^2 (\Phi_h/2)/R_e \qquad \text{(D-25d)}$$
$$S_{22} = 1 - 2 \ell_t \sin^2 (\Phi_h/2)/R_e \qquad \text{(D-25e)}$$
$$S_{25} = -\sin \Phi_h \qquad \text{(D-25f)}$$
$$S_{33} = S_{44} = S_{55} = 1 \qquad \text{(D-25g)}$$

$$S_{34} = \ell_t + \ell_a - 2\,R_e + R_e\,\Phi_h\,\cot\,(\Phi_h/2) \tag{D-25h}$$

(all other matrix elements = 0)

Equations of this type have been previously derived by W. A. Wenzel, but with a somewhat different approach.[21]

APPENDIX E

DETERMINATION OF THE WEDGE ANGLE FOR H_1 BENDING MAGNET

Assume an initial vector

$$X_i = \begin{pmatrix} x_i \\ x_i' \\ y_i \\ y_i' \\ \dfrac{\Delta P_2}{P_2} \end{pmatrix} \tag{E-1}$$

at the entrance face of the H_1 vertical bending magnet, where the coordinates are measured in a plane perpendicular to the optic axis. Looking downstream, the x-axis is positive to the left in the horizontal, and the y-axis is positive in the vertical direction. This system of coordinates is used throughout in both the LMC and the HMC for the matrix calculation of the magneto-optics.

Using the matrix Q_B for a vertical bending magnet, one may write (see Appendix D)

$$X_e = Q_B X_1 \tag{E-2}$$

at the exit face of the magnet. If

$$y_i = 0 \text{ and } y_i' = 0,$$

this gives

$$y_e = b_{35} \frac{\Delta P_2}{P_2} \tag{E-3}$$

and

$$y_e' = b_{45} \frac{\Delta P_2}{P_2} \quad . \tag{E-4}$$

From the matrix for a field free region (see Appendix D)

$$X_d = Q_f\ X_e$$

at the detector. For d equal to the length ℓ_f of the field free region, one obtains

$$y_d = f_{11}\ y_e + f_{12}\ y_e' \qquad \text{(E-5)}$$

where

$$f_{11} = 1 \qquad \text{(D-3a)}$$

$$f_{12} = d\ . \qquad \text{(D-3b)}$$

This gives

$$y_d = (b_{35} + b_{45} d)\ \frac{\Delta P_2}{P_2} \qquad \text{(E-6)}$$

Therefore, if y_d is just the scintillator width w, then

$$\Delta P_2 = w \cdot P_2/L, \qquad \text{(E-7)}$$

where

$$L = b_{35} + b_{45}\ d \qquad \text{(E-8)}$$

and

$$b_{35} = \ell_{eff} \sin \frac{\Phi_v}{2}\ ; \qquad \text{(D-5g)}$$

$$b_{45} = 2 \sin \frac{\Phi_v}{2} \cos\left(\epsilon - \frac{\Phi_v}{2}\right) \cos \epsilon. \qquad \text{(D-5j)}$$

Referring again to the bending matrix Q_B of Appendix D, the focal length f due to focusing in the vertical plane is defined as

$$f = {}^{-1}/{}_{b_{43}}\ , \qquad \text{(E-9)}$$

where

$$b_{43} = -\sin(\Phi_v - 2\epsilon)/(\rho \cos^2 \epsilon) \qquad \text{(D-5h)}$$

This leads to

$$\frac{\rho}{f} = [\sin \Phi_v \cos 2\epsilon - \cos \Phi_v \sin 2\epsilon]/\cos^2 \epsilon\ . \qquad \text{(E-10)}$$

Solving for ϵ one obtains

$$\tan \epsilon = [1+\cot^2 \Phi_v - \rho/(f \sin \Phi_v)]^{1/2} - \cot \Phi_v . \tag{E-11}$$

Therefore, this gives the wedge angle ϵ as a function of the geometric parameters

$$\Phi_v = \text{angle of deflection}$$

and

$$\rho = \ell_{eff}/(2 \sin \frac{\Phi_v}{2})$$

for

$$\ell_{eff} = \text{the effective length of the field}$$

where the focal length f can be measured empirically.

APPENDIX F

IMPORTANT PROTON-PROTON ELASTIC SCATTERING RELATIONSHIPS

For the derivation of a number of important relations for $p + p \rightarrow p + p$ it is convenient to define the four vectors

$$\underset{\sim}{P}_o = (\underline{P}_o, E_o)_{Lab} \quad ; \quad (\underline{q}_o, E/2)_{c.m.}$$

$$\underset{\sim}{P}_t = (0, m_o)_{Lab} \quad ; \quad (-\underline{q}_o, E/2)_{c.m.}$$

$$\underset{\sim}{P}_1 = (\underline{P}_1, E_1)_{Lab} \quad ; \quad (\underline{q}_1, E/2)_{c.m.}$$

$$\underset{\sim}{P}_2 = (\underline{P}_2, E_2)_{Lab} \quad ; \quad (\underline{q}_2, E/2)_{c.m.}$$

where the subscripts o, t, 1, 2 refer to the incident, target, and scattered protons respectively. In the center of mass

$$q = |\underline{q}_o| = |\underline{q}_1| = |\underline{q}_2|$$

is the magnitude of the momentum and E is the energy of the system. Therefore the four momentum transfer for P_2 is defined by

$$t_2 = (\underset{\sim}{P}_o - \underset{\sim}{P}_2)^2 \qquad \text{(F-1)}$$

which is Lorentz invariant. In the center of mass coordinates this gives

$$t_2 = -(q_o^{\,2} - 2\, q_o\, q_2 \cos\theta_{2_{cm}} + q_2^{\,2})$$

or

$$t_2 = -2\, q^2\, (1 - \cos\theta_{2_{cm}}) \,. \qquad \text{(F-2)}$$

From the Lorentz invariant direct product of $\underset{\sim}{P}_t$ and $\underset{\sim}{P}_1$ one obtains

$$\underset{\sim}{P}_t \cdot \underset{\sim}{P}_1 = (q_o\ q_1 \cos \theta_{1_{cm}}) + E^2/4$$

or

$$\underset{\sim}{P}_t \cdot \underset{\sim}{P}_1 = q^2 \cos \theta_{1_{cm}} + E^2/4 , \tag{F-3}$$

and

$$\underset{\sim}{P}_t \cdot \underset{\sim}{P}_1 = m_o\ E_1 . \tag{F-4}$$

Using the relations

$$E_1 = T_1 + m_o \tag{F-5}$$

$$E^2/4 = q^2 + m_o^2 , \tag{F-6}$$

where T_1 is the laboratory kinetic energy of the scattered proton. Then from Eqs. (F-3) and (F-4) one obtains

$$2\ q^2\ (1 + \cos \theta_{1_{cm}}) = 2\ T_1\ m_o . \tag{F-7}$$

However,

$$\cos \theta_{1_{cm}} = - \cos \theta_{2_{cm}} . \tag{F-8}$$

Therefore, from Eqs. (F-2), (F-7), and (F-8) one may write

$$|t_2| = 2\ q^2\ (1 - \cos \theta_{2_{cm}}) = 2\ T_1\ m_o . \tag{F-9}$$

Thus, for looking at large angles in the laboratory system ($\theta_{1_{Lab}}$ large) the form

$$|t| = 2\ T_1\ m_o$$

used to plot the data of this experiment is the four momentum transferred to the forward scattered particle.

The cross section in the center of mass system may be defined by

$$d\sigma/d\Omega_{c.m.} = (N_S/N_I\ n_t)/\Delta\Omega_{c.m.} \tag{F-10}$$

where

N_S = number scatter particles

N_I = number of incident protons

n_t = target thickness in protons/mb

$\Delta\Omega_{c.m.} = \Delta\phi \; \Delta \cos \theta_{c.m.}$.

Using Eq. (F-10), the Lorentz invariant differential cross section is given by

$$d\sigma/d|t| = (N_S/N_I \; n_t)(1/\Delta\phi \; \Delta \cos \theta_{cm})(2\pi \; \Delta \cos \theta_{cm}/ \; \Delta|t| \;) . \qquad \text{(F-11)}$$

From Eq. (F-9) one obtains

$$\Delta|t| = 2 \; m_o \; c^2 \; P_1 \; \Delta P_1/E_1 \; , \qquad \text{(F-12)}$$

where

$$P_1 = \gamma_1 \; \beta_1 \; m_o \; c \qquad \text{(F-13)}$$

and

$$E_1 = \gamma_1 \; m_o \; c^2 \; . \qquad \text{(F-14)}$$

Then one re-writes Eq. (F-11) in the form

$$d\sigma/d \; |t| = (N_S/N_I \; n_t)\pi/(m_o c \cdot \beta_1 \cdot \Delta\phi \cdot \Delta P_1) \; . \qquad \text{(F-15)}$$

From the momentum relation

$$\underline{P}_2 = \underline{P}_o - \underline{P}_1 \; , \qquad \text{(F-16)}$$

one may write the relation

$$P_2^{\;2} = P_o^{\;2} + P_1^{\;2} - 2 \; P_1 \; P_o \cos \theta_{1_{Lab}} \; . \qquad \text{(F-17)}$$

The total incident and final laboratory energies are conveniently related by the form

$$E_o + m_o c^2 = E_1 + E_2 \,. \tag{F-18}$$

also, γ_o and β_o are defined by

$$P_o = \gamma_o \beta_o m_o c \;, \tag{F-19}$$

$$E_o = \gamma_o m_o c^2 \,. \tag{F-20}$$

Now by substituting Eq. (F-17) and the definitions (F-13), (F-14), (F-19), and (F-20) into Eq. (F-18), one obtains

$$\gamma_o + 1 = \gamma_1 + (\gamma_1^{\,2} \beta_1^{\,2} + \gamma_o^{\,2} \beta_o^{\,2} - 2\,\gamma_o \beta_o \gamma_1 \beta_1 \cos \theta_{1_{Lab}} + 1)^{1/2} \,. \tag{F-21}$$

By using the indentities

$$\gamma_1^{\,2} \beta_1^{\,2} = \gamma_1^{\,2} - 1 \tag{F-22}$$

$$\gamma_o^{\,2} \beta_o^{\,2} = \gamma_o^{\,2} - 1 \,, \tag{F-23}$$

one may reduce Eq. (F-21) to

$$\gamma_1 = \left[1 + \left\{ (\gamma_o - 1)/(\gamma_o + 1) \right\} \cos^2 \theta_{1_{Lab}} \right] / \left[1 - \left\{ (\gamma_o - 1)/(\gamma_o + 1) \right\} \cos^2 \theta_{1_{Lab}} \right] . \tag{F-24}$$

From Eq. (F-9), where $\theta_{2_{cm}} = \pi$, one obtains

$$2\, q^2\, (2) = 2T_o\, m_o \;,$$

or

$$q^2 = (\gamma_o - 1)\, m_o^{\,2}\, c^2/2 \,. \tag{F-25}$$

However, by substituting the definitions

$$q = \beta_{cm}\, \gamma_{cm}\, m_o c \tag{F-26}$$

and

$$\gamma_{cm}^{\,2} = 1/(1 - \beta_{cm}^{\,2}) \tag{F-27}$$

into Eq. (F-25) one may obtain

$$\beta_{cm}^{\;2} = (\gamma_o - 1)/(\gamma_o + 1) \tag{F-28}$$

Therefore Eq. (F-24) may be written

$$\gamma_1 = \left[1 + \beta_{cm}^{\;2} \cos^2 \theta_{1_{Lab}}\right] \Big/ \left[1 - \beta_{cm}^{\;2} \cos^2 \theta_{1_{Lab}}\right] . \tag{F-29}$$

From Eqs. (F-22) and (F-29) the laboratory momentum of the scattered beam is

$$P_1 = \sqrt{\gamma_1^{\;2} - 1}\; m_o c$$

or

$$P_1 = 2\, m_o c\, \beta_{cm} \cos \theta_{1_{Lab}} \Big/ \left[1 - \beta_{cm}^{\;2} \cos^2 \theta_{1_{Lab}}\right] . \tag{F-30}$$

REFERENCES

1. G. F. Chew and S. C. Frautschi, Phys. Rev. Letters, 7, 394 (1961).
2. Luke C. Yuan, Proceedings of the Topical Conference on Recently Discovered Resonant Particles, 51, (1963).
3. S. J. Lindenbaum, International Conference of N-Structure, Stanford (1963).
4. S. D. Drell, 11th International High Energy Physics Conference at CERN.
5. H. Lohrman, H. Meyer, H. Winzeler, Phys. Rev. Letters, 13, 78 (1964).
6. L. Kirilova, L. Khristov, V. Nikitin, M. Shafranova, L. Strunov, V. Sviridov, Z. Korbel, L. Rob, P. Markov, Kh. Tchernev, T. Todorov, A. Zlateva, Phys. Lett. 13, 93 (1964).
7. A. E. Taylor, A. Ashmore, W. S. Chapman, D. F. Falla, W. H. Range, D. B. Scott, A. Astbury, F. Capocci, and T. G. Walker, Phys. Lett., 14, 54 (1965).
8. K. J. Foley, R. S. Gilmore, R. S. Jones, S. J. Lindenbaum, W. A. Love, S. Ozaki, E. H. Willen, R. Yamada, and L. C. L. Yaun, Phys. Rev. Letters, 14, 74 (1965).
9. G. Bellettini, G. Cocconi, A. N. Diddens, E. Lillethun, J. Pahl, J. P. Scanlon, J. Walters, A. M. Wetherell, and P. Zanella, Phys. Letters, 14, 164 (1965).
10. P. Söding, Phys. Rev. Letters, 8, 285 (1964).
11. R. J. N. Phillips and W. Rarita, Phys. Rev. Letters 14, 502 (1965).
12. L. W. Jones, Phys. Rev. Letters, 8, 287 (1964).
13. Jay Orear, Phys. Rev. Letters, 12, 112 (1964).

14. G. Cocconi, V. T. Cocconi, A. D. Krisch, J. Orear, R. Rubinstein, D. B. Scarl, W. F. Baker, E. W. Jenkins, and A. L. Read, Phys. Rev. Letters, <u>11</u>, 499 (1963).

15. Owen Chamberlain, Ann. Rev. Nucl. Sci. <u>10</u>, 16 (1960).

16. W. G. Cross, Rev. Sci. Inst., <u>22</u>, 717 (1951).

17. Beverly Hill Willis, Charles V. Stableford, UCRL-2426, Vol. II, January, 1965.

18. Thomas J. Devlin, UCRL-9727, September, 1961.

19. Francis F. Chen, Christopher P. Leavitt, and Anatole M. Shapiro, Phys. Rev. <u>99</u>, 857 (1955).

20. Francis F. Chen, Christopher P. Leavitt, and Anatole M. Shapiro, Phys. Rev. <u>103</u>, 211 (1956).

21. W. A. Wenzel, Dev 826, May 21, 1963 (<u>unpublished</u> - LRL internal report).

22. R. F. George, K. F. Riley, R. J. Tapper, D. V. Bugg, D. C. Salter, and G. H. Stafford, Phys. Rev. Letters <u>15</u>, 214 (1965).

23. Private communication with C. M. Ankenbrandt.

24. H. A. Bethe, Annals of Phys. <u>3</u>, 190 (1958).

25. J. D. Dowell, R. J. Homer, Q. H. Khan, W. K. McFarlane, J. S. C. McKee and A. W. O'Dell, Phys. Letters <u>12</u>, 252 (1964).

26. W. M. Preston, R. Wilson, and J. C. Street, Phys. Rev. <u>118</u>, 579 (1959).

27. B. Cork, W. A. Wenzel, C. W. Causey, Phys. Rev. <u>107</u>, 859 (1957).

28. Jay Orear, Phys. Lett., <u>13</u>, 190(1964).

29. G. Fast and R. Hagedorn, Nuovo Cimento <u>27</u>, 208(1963).

30. G. Fast, R. Hagedorn, and L. W. Jones, Nuovo Cimento <u>27</u>, 856(1963).